Evolving morphology and rheological properties of an emulsion undergoing clathrate hydrate formation

by

Prasad Uday Karanjkar

A Dissertation

Submitted to the Graduate Faculty in Engineering

in Partial Fulfillment of the Requirements

for the Degree of

Doctor of Philosophy

The City University of New York

2012

This manuscript has been read and accepted for the Graduate Faculty in Engineering in satisfaction of the dissertation requirement for the degree of Doctor of Philosophy.

Date	Prof. Jeffrey F. Morris Chair of Examining Committee
Date	Prof. Jae W. Lee co-Chair of Examining Committee
Date	Mumtaz K. Kassir Executive Officer
	Prof. Charles Maldarelli
	Prof. Morton Denn
	Prof. Alexander Couzis
	Dr. Hariprasad Subramani

Supervisory Committee

THE CITY UNIVERSITY OF NEW YORK

Abstract

Evolving morphology and rheological properties of an emulsion undergoing clathrate hydrate formation

by

Prasad Uday Karanjkar

Advisors: Jae W. Lee and Jeffrey F. Morris

Blockage of natural gas and crude oil subsea transport pipelines due to hydrate plug formation is a major concern in the petroleum industry as it directly affects the goal of flow assurance. A proper analysis of hydrates requires knowledge of the dynamic processes of formation and dissociation as well as understanding of their rheological and morphological properties. This work addresses the issue of clathrate hydrate formation in oil-dominated systems relevant to subsea crude oil transport. Cyclopentane, which forms hydrate at atmospheric pressure, is used as a component of the oil phase in our model emulsions.

Differential scanning calorimetry (DSC) is applied to investigate the formation of cyclopentane hydrates in a water-in-oil emulsion. A novel method based on comparing the heat flow measured by DSC for samples of identically prepared hydrate-forming and non-hydrate (ice-forming) emulsions is developed to obtain the rate of cyclopentane hydrate growth. Experimental results lead to the conclusion that the hydrate formation is an interfacial phenomenon and occurs primarily at the interface between water drops and the continuous oil phase. A three-step mechanism – nucleation, lateral surface growth and radial growth – is described to capture the main features of the hydrate formation process. Mechanical stresses developed in the hydrate shell due

to volume expansion upon hydrate formation (a liquid-solid transition) are analyzed.

The proposed three-step mechanism for the hydrate formation is supplemented by direct visualization of hydrate growth at a single water drop suspended in the oil phase. The crystal morphology study probes the effect of an oil-soluble surfactant sorbitan monooleate (Span 80) on the crystal behavior at the water-oil interface. In the absence of surfactant, a faceted polycrystalline hydrate shell develops around the water drop. This limits transport of hydrate former to the free (liquid) water which remains trapped inside the hydrate layer. The presence of Span 80 at concentrations greater than 0.01% by volume in the oil phase leads to a hairy or mushy hydrate morphology. A unique hollow-conical crystal is observed during the lateral surface growth at these Span 80 concentrations. A detailed analysis is presented to explain the role of Span 80 on driving force and transport for the morphological development. The effect of a commercially available anti-agglomerant on the hydrate morphology is investigated. Preliminary results for the high-pressure propane hydrate morphology are reported.

The rheological properties of hydrate-forming emulsions are investigated over a wide range of water volume fractions, both for oil- and water-continuous emulsions. The hydrate formation leads to an irreversible increase in the mechanical properties; high dispersed phase fraction emulsions, especially 30% to 60% water volume fraction, show a rapid viscosification resulting in a rheometer jamming. A mechanism in which the hairy and porous hydrate growth combined with enhanced agglomeration due to liquid bridges formed by wetted water films leads to development of a porosity, resulting in greater effective dispersed phase fraction is proposed. This is supported by experiments performed at variable shear rates, temperatures and surfactant concentrations. In order to probe the hydrate morphological properties under flow, we describe the development of a *flow rheometer* providing the capability of measurement

of mechanical properties together with morphological characteristics through visualization. The results are reported for a 40% water-in-oil emulsion and it is observed that mushy, cotton-like hydrate balls form a complex and porous network developing into a hydrate plug.

Acknowledgements

First and foremost I want to convey my deepest gratitude to my advisors Prof. Jae Lee and Prof. Jeffrey Morris. I truly appreciate all their contributions of time, invaluable ideas and funding to make my Ph.D. experience productive and enlightening. They have always encouraged me to think independently, provided freedom and resources to pursue new ideas and have been very supportive throughout the ups and downs of my work. Their passion and professional attitude towards scientific research was motivational and has been a learning experience for me; it was truly an honor to work with them. I remember Prof. Morris once said, *'the beauty of this project exists in how complicated it is'* – thanks for such an excellent opportunity, I enjoyed working on this challenging project and I am very happy to move on in my career with this valuable experience in my pocket.

I very much appreciate the useful comments on this work provided by my thesis committee, Prof. Charles Maldarelli, Prof. Morton Denn, Prof. Alexander Couzis and Dr. Hariprasad Subramani. I am grateful to Prof. Charles Maldarelli for his guidance and constructive discussions on interfacial effects. I am very thankful to Chevron Flow Assurance Core Team for their valuable inputs, brain-storming sessions and financial support for the project. I also want to thank Chevron Corporation for providing me with a valuable summer internship opportunity.

I would also like to thank my lab mates, Allan, Jorge, Junshe, Pablo, Hitesh, Parisa, Prasad, Pandurang, Sandeep, Xiajuan, Chi, Ehssan, Genti, Hamed and Amit for their guidance, support, useful discussions and providing a wonderful work environment. I am also grateful to Xu, Andy, Junjun and Mary for their support during all these years. Having a great company of friends, room-mates, batch-mates, seniors

and juniors, made my stay at City College an enjoyable experience.

Special thanks to Pranav and Jaspal for all their love and encouragement. A patient and faithful support from Jaspal during the final stages of this Ph.D. is so appreciated. Finally, I want to dedicate this Ph.D. thesis to my parents, *Mummy & Baba*, Mrs. Arti Karanjkar and Mr. Uday Karanjkar. It would have been impossible for me to succeed in my career without their love, teaching and support.

Prasad Uday Karanjkar

Contents

List of Figures

List of Tables

Chapter 1

Introduction

1.1 Background and Motivation

Rising demand for fossil fuels and lack of easily discoverable oil and gas reserves are driving new exploration and production (E&P) projects worldwide. With E&P increasingly shifting to offshore, the use of subsea pipelines for transportation of hydrocarbons is rising proportionately. In these offshore projects, large water depths, low temperatures and remote locations present many new challenges to subsea operations. Ensuring a successful, continuous, economical and environmentally safe flow of hydrocarbons through subsea pipelines, from reservoir to storage or processing facility, is the main challenge and is usually referred to as *'flow assurance'* in the oil and gas industry. The term was coined by Petrobras in the early 1990's in Portuguese as *'Garantia de Fluxo'*, meaning *'Guarantee the Flow'*. In 1999, Welling and Associates conducted a survey of 110 oil companies throughout the world [1] and revealed that flow assurance was the most important technical issue facing the petroleum industry. Since then, with the exploration of ultra deep-water fields to satisfy the growing energy demand, flow assurance challenges have increased significantly.

Flow assurance is an extremely diverse issue, involving many specialized topics

and engineering disciplines. It may include formation of solid deposits like gas hydrates, wax, asphaltenes and scale which reduce the flow capacity, erosion due to solid particle or liquid impingement, corrosion due to chemistry of materials present, slugging caused by instabilities at gas-liquid interfaces and formation of emulsions that cause excessive pressure losses. The consequences of these issues can be serious and include significant intervention costs, substantial losses in production or even catastrophic pipeline blockages leading to unscheduled shutdown scenarios.

From the beginning of the 20^{th} century, every oil and gas company encountered difficulties in production due to plugging of transport pipelines by deposition of some icy crystals from the fluid flowing through the pipelines. Initially it was believed that the small fraction of water that enters the main stream during drilling operation crystallizes into ice particles at cold subsea environments. However, in the early 1930's Hammerschmidt [2] found that plugging of natural gas pipelines is due to formation of *'clathrate hydrates'* of natural gas, which are ice-like solids but not ice. This discovery led to more detailed studies on these crystalline compounds called gas hydrates, found to be stable at conditions of high pressure and low temperature. Hydrate formation is usually detected by increase in pipeline pressure drop or changes in fluid rates and composition, *e.g.* significant decrease in water amount at the separator suggests hydrates may be forming inline. However, hydrates usually form rapidly without sufficient advance warning resulting in minimal response time for implementing engineering solutions like pigging or thermal treatment, and thus are considered as the most critical and challenging flow assurance problem compared to other solid deposits [3]. Figure 1.1 shows a gas hydrate plug recovered from a Petrobras subsea pipeline off the coast of Brazil and depicts the severity of the problem. Where it is known that hydrate formation is much faster compared to other solid buidups like wax, scale or asphaltenes (several hours as compared to months),

Figure 1.1: A gas hydrate plug taken from an offshore production line of Petrobras, Brazil.

it can take weeks or even months to get rid of hydrate plugs in a safe manner. Also as recently learned, gas hydrate formation can be a major issue in other hydrocarbon production aspects as well. Gas hydrates were believed to be the key problem that led to a failure of a 100 ton containment cap for the deepwater Macondo well blowout in the Gulf of Mexico in 2010. The pressure and temperature conditions at the water depths of oil leak were favorable for gas hydrate formation and thus further oil leak containment efforts required proper hydrate-handling policies.

There are mainly two types of pipeline flows in petroleum industry, 'gas-dominated' and 'liquid-dominated'. This defines the major type of fluid transported through the pipeline. The motivation of our study is on the hydrate formation in liquid/oil-dominated systems, *i.e.* modeling crude oil transport rather than natural gas transport. Water or brine flowing with the oil usually gets stabilized in the form of water-in-oil (w/o) emulsion due to the presence of naturally occurring surface-active substances, *e.g.* asphaltenes and resins [4]. Under suitable pressure and temperature conditions, water drops undergo hydrate formation as the hydrate-forming natural

gas components like methane and ethane are usually soluble in the oil phase at high pipeline pressures. The agglomeration of these now-solid particles cause the problem of hydrate plug formation.

Various hydrate mitigation strategies for hydrocarbon subsea pipeline transport can be organized as –

- Maintaining pressure and/or temperature conditions outside the hydrate formation region.
- Changing the composition of production stream to minimize hydrate formation.
- Injecting additives like thermodynamic or kinetic inhibitors, or anti-agglomerant chemicals into the production stream.

Temperature conditions can be changed by insulating the pipeline to avoid heat losses, heating them by circulating hot oil or by direct electrical heating methods. Hydrate plugs can be removed by reducing pressure levels below the equilibrium value and can be achieved either by one-sided depressurization or two-sided depressurization. Both of these options significantly increase capital or operating costs. Also, additional precautions are necessary in depressurization techniques as the hydrate plug can suddenly break from the wall and develop into a "missile" damaging downstream facilities or injuring personnel. Similarly, modifying the composition of production stream by separating gases and liquids to avoid water-gas contact, reducing water content or reducing concentration of hydrate-forming components is possible but very costly as it requires an effective subsea separator.

The most commonly used chemical additives are thermodynamic inhibitors such as methanol and glycols. The addition of such chemicals shifts the hydrate phase boundary to lower temperatures at a fixed pressure, providing more operating window

as shown in Figure 1.2. The hydrate phase boundary is a pressure-temperature (P-T) envelope separating the hydrate-forming zone from the hydrate-free zone. Though the thermodynamic inhibitors are widely used, the effective concentrations go as high as 30 to 50% with respect to water amount. This results in high costs associated with quantity and storage. Also, the large quantities of methanol in the production stream not only cause serious problems in desalting, water management and final quality of the product but can also lead to corrosion issues due to dissolved oxygen. Thus a new class of hydrate inhibitors called low dosage hydrate inhibitors (LDHI) are being used [5]. The required concentration of such chemicals is expected to be less than 1% with respect to water amount. There are two types of LDHI, kinetic inhibitors (KI) and anti-agglomerants (AA). KI, mostly water soluble polymers, prevent or delay hydrate nucleation and slow down the crystal growth. Therefore, KI have no effect on the hydrate phase boundary but limit the hydrate growth rate for a period of time. The effectiveness of KI additives is known to be limited by the degree of sub-cooling and the residence time, with commonly accepted maximum allowable sub-cooling of 10°C for a residence time of 2 days. Sub-cooling corresponds to the driving force for hydrate formation and is defined as the difference between the hydrate equilibrium temperature and the operating temperature at a given pressure. Unlike thermodynamic or kinetic inhibitors, AA additives do not affect the hydrate formation process but instead affect the hydrate surface properties reducing the binding between hydrate particles. In short, they inhibit the agglomeration process and fluid can be transported as a slurry ensuring the continuity of an operation, and thus these are usually referred to as dispersant additives as well. The main limitation associated with AA is the maximum allowed water cut: usually accepted values are 40 to 50%. Due to these limitations, a combined use of thermodynamic inhibitors and LDHI additives is found to be an efficient strategy in most cases.

In addition, a technique called 'cold flow technology' (CFT) is being developed as an alternative technology. In this method, produced water is directly converted into inert hydrate particles and transported as a slurry without a risk of pipeline blockage. The main goal of CFT is to eliminate the need for chemical additives and heating methods. Special precautions are necessary in case of shut down and restart operations, as the hydrate particles may accumulate during shut down and further develop into a plug during restart. Other techniques like use of chemicals or heating may need to be implemented under such circumstances. More information about CFT can be found in the references [6, 7, 8].

The need for affordable, reliable and long term methods for the prevention of hydrate plug formation calls for a detailed understanding on the behavior of *w/o* emulsions (oil-field emulsions) under hydrate-forming conditions. A proper analysis requires knowledge of the dynamic processes of hydrate formation and dissociation, as well as an understanding of their rheological and morphological properties in multi-phase systems where they are encountered. Although the thermodynamics of hydrate formation is relatively well established, other important aspects of their behavior, including rheology and morphology, are not well studied. Our approach is to probe the properties of these hydrate-forming emulsions and the resulting hydrate slurries using techniques of rheology, crystal morphology, calorimetry and lab flow experiments. A detailed outline of the thesis is presented at the end of this chapter.

1.2 Hydrates

Hydrates are ice-like solid crystalline compounds with cage-like structures of water molecules [9, 10]. The cavities in these structures are occupied by external guest molecules. The cages are stabilized by van der Waals forces between the water

molecules and the entrapped guest molecule. These guest molecules can be low molecular weight hydrocarbon gases (CH_4,C_2H_6, *etc.*) or others gases like H_2, CO_2 or H_2S and liquids like tetrahydrofuran (THF) or cyclopentane. Hydrates are classified as structure I, II and H hydrates, depending on the size of cavities. Cavity size is determined from the number of pentagonal and hexagonal faces formed by H_2O molecules, refer to Figure 1 from [9] for details. Structure I and II have two kinds of cavities: small cavity (5^{12}, *i.e.* pentagonal dodecahedron) found in both structures and large cavity: ($5^{12}6^2$, *i.e.* tetrakaidecahedron) and ($5^{12}6^4$, *i.e.* hexakaidecahedron) for structure I and II, respectively. Structure I can be stabilized by gas molecules like pure methane or ethane, but the presence of a small amount of larger molecule like propane (0.5 mol %) with methane would result in structure II. Structure H contains three cavities: small cage (5^{12}) and two large cavities. Mainly structure II is expected to form with natural gas in production lines, because this gas contains a mixture of methane with larger molecular weight gases.

Unlike ice, hydrates can be stable at temperatures higher than 0°C. Conditions suitable for hydrate formation are high pressure (typically $\geq$ 30 bar) and low temperature (typically $\leq$ 20°C). A thermodynamic phase diagram for natural gas hydrates is shown in Figure 1.2. Hydrates may not form exactly at the conditions specified by the phase curve. At a given pressure, due to kinetic effects, temperature of formation may be lower than specified by the phase diagram. This kinetic effect produces a metastable zone in the phase diagram. This implies that hydrate formation needs some time if pressure and temperature are in the metastable region, known as an induction time. This temperature offset is usually referred to as sub-cooling. The larger the sub-cooling, the lower will be the induction time and the greater will be the hydrate formation rate.

Though the hydrate formation is a problem for the petroleum industry, hydrates

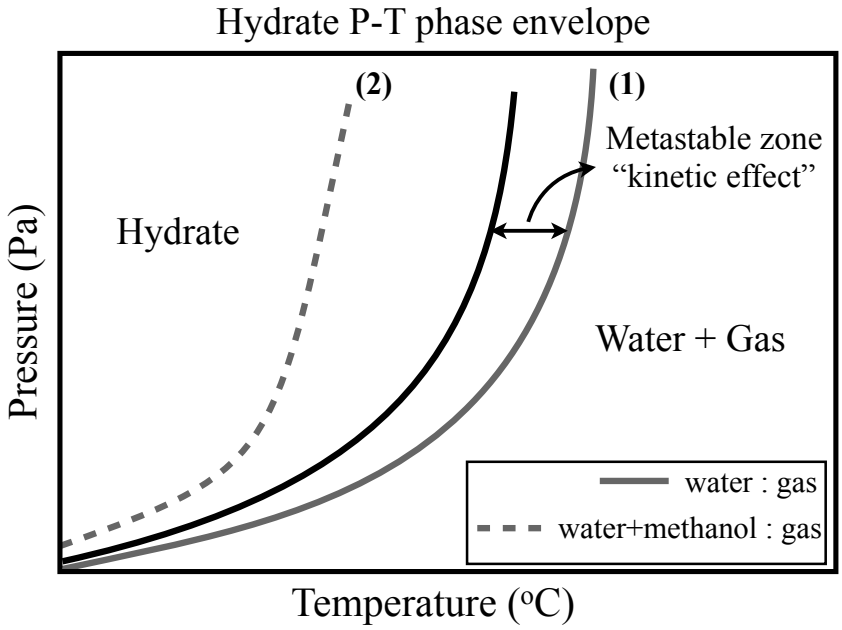

Figure 1.2: Hydrate Pressure - Temperature phase envelope (1) water - natural gas (2) water and methanol mixture - natural gas

of natural gas are considered to be an enormous potential future energy source. It is generally believed that large quantities of natural gas (predominantly methane) are entrapped as gas hydrates in sediments at the bottom of the ocean [11]. The worldwide volume of natural gas present in the form of hydrates is immense and estimates range from 100,000 to more than 1,000,000 trillion cubic feet (Tcf) of natural gas. According to a recent assessment by the US Minerals Management Service, there is approximately 11,000 - 34,000 Tcf of methane present in hydrate form only in the Gulf of Mexico and this amount is enormously large compared to total US natural gas resource (excluding hydrate), which equals to 2,074 Tcf (http://www.netl.doe.gov). Thus if recovered in a safe manner, hydrate sediments can be a great energy source, but concern also exists that the methane could be released from these sediments if conditions go outside the hydrate stability envelop considering that methane itself is

a potent greenhouse gas. Other potential applications of gas hydrates include efficient and safe transport of natural gas and hydrogen as one m^3 of hydrates contain almost 180 m^3 of natural gas at standard temperature and pressure [12], candidate phase change materials for use in refrigeration operations as a potential thermal energy storage media [13, 14], separation of flue gases and desalination of sea water.

In the present work, *w/o* emulsions are studied using cyclopentane, a liquid phase hydrate former, present in the continuous oil phase. Cyclopentane hydrate forms at atmospheric pressure, with a dissociation temperature of 7°C [14, 15]. While THF also forms a hydrate at atmospheric pressure, liquid THF is miscible with water and thus eliminates the key mass transfer considerations which are present in gas hydrate-forming emulsions; recall the gas in such a system is soluble in the oil phase. Also, as cyclopentane forms structure II hydrates [16] usually encountered in petroleum fields, it serves as a good atmospheric pressure model for high-pressure gas hydrates in emulsions allowing simpler operation under ambient conditions.

1.3 Outline

The thesis is arranged in four chapters followed by supplementary information provided in appendices. Chapter 2 describes a calorimetric analysis of cyclopentane hydrate formation in a 40% water-in-oil emulsion using a micro-differential scanning calorimeter (μDSC). A comparison between segregated and emulsified samples of water and cyclopentane suggests that the hydrate formation is an interfacial phenomenon. A novel method based on comparing the heat flow from DSC for identically prepared hydrate-forming and ice-forming emulsions to obtain the rate of cyclopentane hydrate growth is reported. The analysis is performed at three different heating rates and based on the experimental results, a three-step mechanism

– nucleation, lateral surface growth and radial growth – is described to capture the main features of the hydrate formation process. Development of mechanical stresses in a hydrate shell, due to volume expansion at the liquid-solid transition, is analyzed followed by description of a simple shell (or shrinking core) model for the radial hydrate growth.

Chapter 3 investigates the crystal morphology through direct visualization of hydrate formation at a single water drop suspended in the oil phase. Experimental results supplement the three-step mechanism proposed in the calorimetric studies. This study probes the effect of an oil-soluble surfactant sorbitan monooleate (Span 80) on the crystal behavior during the lateral surface and radial hydrate growth. A faceted polycrystalline hydrate shell formed by joining of numerous flat hydrate facets is obtained in the absence of surfactant, which slows down further radial hydrate growth due to additional diffusion limitations introduced by the solid shell. On the other end, a hairy and porous hydrate morphology is observed in the presence of Span 80 at concentrations greater than 0.01% by volume in the oil phase. A unique three-dimensional hollow-conical hydrate crystal is observed during the lateral surface growth at these Span 80 concentrations. A hypothesis that a mechanical barrier generated by crowding of Span 80 molecules at the interface is responsible for the observed conical crystal shape is supported by experiments at variable Span 80 concentrations and temperatures. This is followed by discussion on the effect of a commercially available anti-agglomerant on the hydrate growth behavior, which is shown to completely inhibit the hairy hydrate growth and leads to a faceted shell formation around the water drop. Preliminary results for a high-pressure propane hydrate morphology are reported.

The rheological properties of density-matched hydrate-forming emulsions are

reported in Chapter 4. The data is obtained using standard rheometers, either stress-controlled AR 2000 or strain-controlled ARES rheometer, equipped with a concentric cylinder geometry. The results are presented over a wide range of water volume fractions, including both water-in-oil and oil-in-water emulsions. The water-in-oil emulsions are stable up to 45% of internal water fraction, with 45% - 57.5% found to be the transition range where emulsions are unstable; above this water fraction, the emulsion inverts to form water-continuous emulsions. An irreversible increase is observed in the emulsion mechanical properties upon hydrate formation and for emulsions with 30% to 60% water volume fraction, the rapid increase in viscosity is shown to stop the rheometer motion with a yield stress of O(3000) Pa. A detailed characterization of 25% water-in-oil and 30% oil-in-water emulsions is performed at variable shear rates. The shear rate during hydrate growth controls the properties of the resulting hydrate slurry which exhibits a shear thinning behavior. The rheology experiments performed at different temperatures and Span 80 concentrations combined with the morphological characteristics support the proposed hypothesis that the hairy and porous hydrates with enhanced agglomeration due to wetted liquid water films serving as liquid bridges develop the porosity and lead to a greater effective volume fraction. A probability analysis of hydrate formation with the change in viscosity as a criterion to detect the phase transition and the effect of sub-cooling and shear rate on the critical time for hydrate formation is reported for a 40% water-in-oil emulsion. This is followed by a description of emulsion viscoelastic properties during hydrate formation.

Chapter 5 describes the development of a *flow rheometer* providing the capability of measurement of mechanical properties combined with the morphological characteristics through direct visualization. The results are reported for the 40% water-in-oil emulsion; the hydrate plug is shown to be a complex and porous network of mushy or

cotton-like hydrate balls, supporting the observations from single-drop morphology experiments.

Appendix A provides supplementary information on the crystal morphology experiments while appendix B describes the effect of repetitive hydrate formation/dissociation on emulsion properties through calorimetric analysis.

Chapter 2

Calorimetric investigation of cyclopentane hydrate formation

2.1 Introduction

One especially useful technique in phase change systems like hydrate formation is calorimetry. Ease of operation and the ability to extract useful thermal information makes the differential scanning calorimeter (DSC) a valuable tool in this area; when the sample size is very small, the method is termed μDSC. Examples of application of DSC to hydrate systems include studies by Parlouër et al. [17] who used high-pressure μDSC, and Zhang et al. [18] who applied the technique to study cyclopentane and THF hydrate formation in emulsions. Fouconnier et al. [19] used DSC along with X-ray diffraction to study trichlorofluoromethane (CCl_3F) hydrate formation in emulsion systems. Dalmazzone et al. [20, 21] have studied methane hydrate formation kinetics in emulsions using high-pressure DSC, and these provide significant overviews of the methodology and its relation to theories of the mechanistic behavior; Lachance et al. [22] used the technique to study the effects of hydrate formation and dissociation on emulsion stability. In support of the possible implementation of hydrates in refrigeration systems, Nakajima et al. [14] employed DSC to determine

the heat of dissociation for cyclopentane hydrates in oil-in-water emulsions. Davies et al. [23] reported nucleation probability based on DSC detection of the onset of hydrate formation while Zhang et al. [24] studied the effect of surfactant on freezing temperature or supercooling point of ice and hydrates. Davies et al. [25] utilized high-pressure DSC to study the mass transfer characteristics of methane hydrate films at the water-hydrocarbon interface. Review articles by Clausse et al. [26, 27] describe previous results obtained by application of DSC techniques to understand various aspects – nucleation, freezing, melting, hydrate formation, mass transfer – in emulsion systems.

In addition to DSC, nuclear magnetic resonance [28, 29] has been applied to probe the hydrate/water drop morphology. Scanning electron microscopy has been used to describe the porous nature of gas hydrates [30, 31], while Raman spectroscopy was applied to study methane-ethane hydrate metastability [32]. An important issue in the hydrate formation at an interface is the transport rate through a hydrate film, and Davies et al. [33] showed using a confocal Raman spectroscopy technique that water is the more mobile species in passage through the film. This is related to the shell, or shrinking core, model of hydrate formation on drops (which is also considered in analyzing our data), a model which has also been probed by studies using dielectric spectroscopy [34]. A review by Sum et al. [35] discusses experimental approaches to hydrate study, while a review by Ribeiro and Lage [36] summarizes different models proposed for hydrate formation kinetics.

In the present calorimetric study, water-in-oil (w/o) emulsions are studied using cyclopentane, a liquid phase hydrate former, present in the continuous oil phase. The ability of cyclopentane to form hydrates at atmospheric pressure has been used previously. Nakajima et al. [14] studied cyclopentane-in-water emulsions for possible use in air-conditioning systems, considering the influence of surfactants on

hydrate formation. The morphological characteristics of the cyclopentane hydrates reported there are qualitatively similar to the observations made in [37, 38]. Sakemoto et al. [39] also investigated morphological characteristics of hydrates at the cyclopentane-water interface, including the effect of dissolved salt in their study. Trichlorofluoromethane (CCl_3F) is another atmospheric pressure hydrate former which is immiscible with water. As noted, Jakobsen et al. [34] studied CCl_3F hydrate formation in *w/o* emulsions using dielectric spectroscopy. This work addressed the validity of the shell model for hydrate formation, and concluded that the diffusion of CCl_3F from the oil phase to the dispersed water droplets is the rate limiting step. Fouconnier et al. [19] also studied CCl_3F hydrate formation in emulsion systems using DSC. Along with DSC, Fouconnier et al. have used a time resolved X-ray diffraction technique to identify the conditions of hydrate formation; this is useful because of the overlap of ice melting (endothermic), hydrate formation (exothermic) and hydrate dissociation (endothermic) signals from DSC during the heating cycle. In their experiments, *w/o* emulsions with 60% water fraction were submitted to a cooling-heating cycle between -50°C and 20°C. From the combined DSC and X-ray diffraction results, Fouconnier et al. showed that only ice formation occurs during cooling and hydrate formation occurs during ice melting once the liquid water becomes available. A simple shell model was proposed in their study along with estimates of the amount of hydrate formed.

We have used the DSC technique in a novel fashion which compares hydrate-forming emulsions with comparable ice-forming emulsions, and combined these studies with mechanical analysis to study the hydrate formation process in *w/o* emulsions. The method developed for μDSC experiments allows us to obtain information on the kinetics of hydrate formation. With the method, we determine the probable sequence of events taking place during hydrate formation in the emulsion and provide

parameters describing hydrate growth rate; note that this information does not represent intrinsic reaction kinetics as nucleation, heat transfer and mass transfer play roles.

We begin in the next section with a description of the experiments, followed by a description of our method for extracting hydrate growth rate information. This is followed by the hypothesized mechanism of hydrate formation in the emulsion as a sequence of nucleation, surface growth and radial growth. Development of mechanical stresses in a hydrate shell, due to volume expansion at the liquid-solid transition, is analyzed for the first time; these appear to play a major role in defining the surface morphology, based on supporting direct visualization in single-drop experiments [37]. A simple shell (or shrinking core) model is shown to capture certain essential features, but shown to be insufficient because the hydrate growth is not simply a diffusion-controlled phenomenon in the presence of oil-soluble surfactants, as the observed morphology of the hydrate formed is more complex than the shell model assumes.

2.2 Experimental section

2.2.1 Materials

Emulsions of different compositions are formed using the organic components light mineral oil (NF/FCC Fisher Chemical), cyclopentane (99%) (also Fisher), *iso*-octane and the surfactant Span 80 (both from Sigma-Aldrich). Span 80 is sorbitan monooleate, a non-ionic surfactant, and is oil soluble with hydrophilic-lipophilic balance (HLB, see [40] for a discussion of this property) of 4±1 (as reported by vendor). All these materials are used as received without further purification. Deionized water is obtained from a Millipore Direct-Q3 system.

Table 2.1 lists the physical properties under ambient conditions for materials used in this study. Span 80 concentration is fixed at 0.1% (v/v) based on the oil phase volume. The oil phase is a 50:50 (by volume) mixture of light mineral oil and cyclopentane when a hydrate-forming system is studied. Cyclopentane is replaced by the same volume of *iso*-octane to obtain a non-hydrate (ice-forming) system which is comparable in viscosity to the hydrate-forming system. Water constitutes 40% of the emulsion volume. Cyclopentane is in excess of the stoichiometric requirement for cyclopentane hydrates which is one mole of cyclopentane to 17 moles of water.

–	Density (gm/cm^3)	Viscosity (cP)	Molecular weight
Light mineral oil	0.86	46	-
Cyclopentane	0.75	0.419	70.1
iso-octane	0.69	0.473	114.23
Span 80	0.986	1200-2000	428.6

Table 2.1: Physical properties of emulsion components at 25°C. Wax appearance temperature of light mineral oil is $\sim$ -15°C, molecular weight data is unavailable.

Each emulsion is prepared in a glass vial by vigorous shaking for five minutes. Though shaking is a crude method for emulsification, it is found to be satisfactory to generate small emulsion volumes (10 ml oil phase); a single run of μDSC requires only 30-40 mg of sample. Reproducibility of emulsion droplet size has been confirmed from optical photomicrographs using a Nikon AZ100 microscope. A freshly prepared emulsion sample (without dilution) is transferred into a rectangular capillary (0.1 $\times$ 1 mm) placed over a glass slide for microscopy. Figure 2.1 shows photomicrographs of the emulsion up to 24 hours after preparation. The glass vial is gently tilted upside down a few times before sampling for these images. Emulsions are found to be stable against coalescence for several hours as the droplet size distribution remains roughly constant (see Table 2.2). The average drop diameter remains around 40 μm up to 24 hours, much longer than the total duration of an experiment. The variations seen

are a result of sampling rather than an evolution in size. The emulsion was similarly stable against coalescence when maintained at -3°C.

Time (hours)	Mean drop size (μm)	Standard deviation (μm)
0	40.5	20.5
2	41.0	16.2
4.5	40.0	17.8
24	39.3	17.6

Table 2.2: Droplet size distribution of 40% hydrate-forming *w/o* emulsion as a function of time.

2.2.2 Micro-differential scanning calorimeter, μDSC

A micro-differential scanning calorimeter (μDSC VIIa, Setaram Inc.) is used for calorimetric studies. The working principle is based on measurement of the temperature of a sample and reference; the necessary heat to achieve a zero difference between the two is recorded as an output. The principle of this technique is described in detail by Parlouër et al. [17].

2.3 Results and discussion

2.3.1 Kinetics

Figure 2.2 compares the heat flow curves in a DSC of hydrate- and ice-forming emulsions for the same temperature protocol. Temperature is decreased from 20°C to -45°C and then brought back to 20°C at a fixed ramp rate of 1°C/min in each direction. An exothermic peak is observed during the cooling ramp in both emulsions, due to formation of ice. Upon heating there is an endotherm observed in either system, near 0°C. In the hydrate system, during heating there is an additional endothermic peak

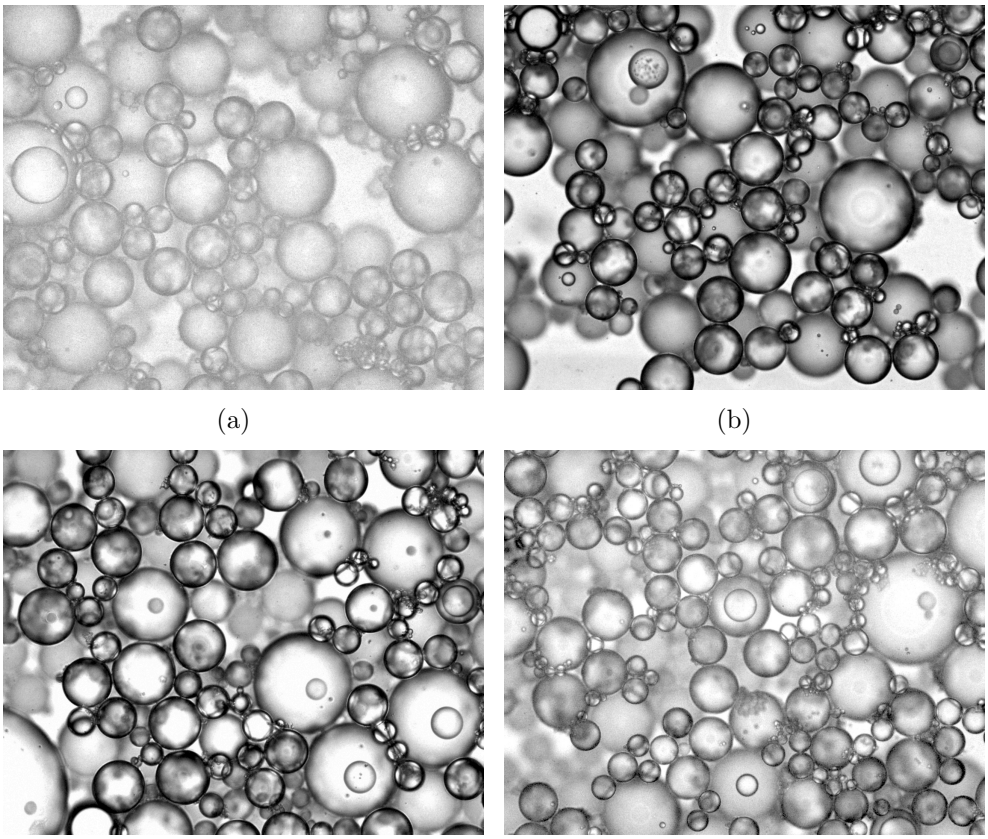

(a) (b)

(c) (d)

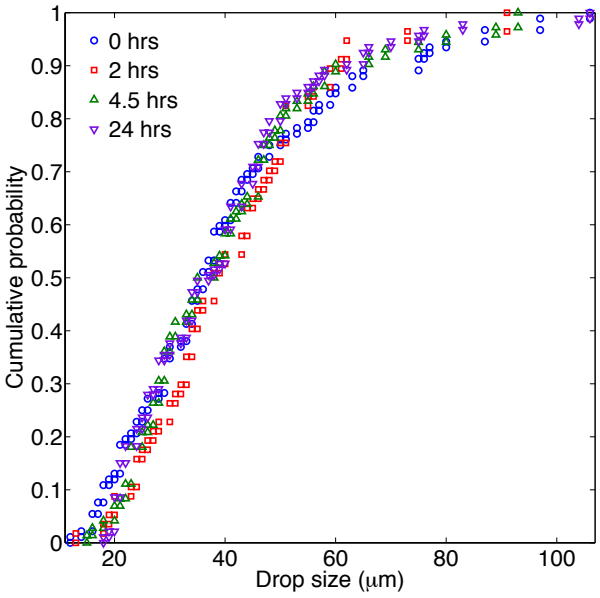

(e)

Figure 2.1: Emulsion photomicrographs (450 × 360 μm) at different times after preparation (a) 0 hours, (b) 2 hours, (c) 4.5 hours, (d) 24 hours, (e) cumulative drop size distributions; 40% *w/o* hydrate-forming emulsion, 50% of oil phase is cyclopentane.

corresponding to hydrate dissociation, observed just after the endotherm of an ice melting. An energy balance shows that predominantly ice formation occurs during the cooling ramp, producing a single exothermic peak; calculations are provided under 'hydrate conversion analysis method' at the end of this section. Fouconnier et al. [19] studied CCl_3F hydrate formation in *w/o* emulsion, and also found a single exothermic peak during cooling. They have coupled X-ray diffraction with DSC to separate ice formation, ice melting, hydrate formation and hydrate dissociation curves. X-ray diffraction shows that only ice formation takes place (in a single exotherm) during cooling. Therefore, we assume that our exothermic peak during cooling corresponds to ice formation.

The temperature of the exotherm corresponding to ice formation, both for hydrate- and ice-forming emulsions, is around -20°C. This is above the homogeneous ice nucleation point of -38°C [18]. Clausse [27] reported that the shape of an exothermic peak corresponding to freezing allows one to distinguish between bulk and emulsified water. For emulsified water, Clausse has argued that the exothermic peak should be symmetric and bell-shaped while bulk water shows an asymmetric peak. The asymmetry can be explained by rapid release of energy once ice nucleation occurs in a bulk volume. In our experiments, the exothermic peaks, both for hydrate- and ice-forming emulsions, are asymmetric. Significant attention was thus placed on the stability of our emulsions, as this exotherm asymmetry suggests destabilization and coalescence of water drops. However, as observed from photomicrographs in Figure 2.1, the emulsions in the present study are completely stable against coalescence up to 24 hours. A possible reason for the disagreement with the argument of Clausse is that some crowding of droplets (due to settling of water drops) is observed, with associated flocculation. Once ice nucleation occurs, we speculate that the flocculated water droplets may undergo a rapid conversion with energy release similar to that

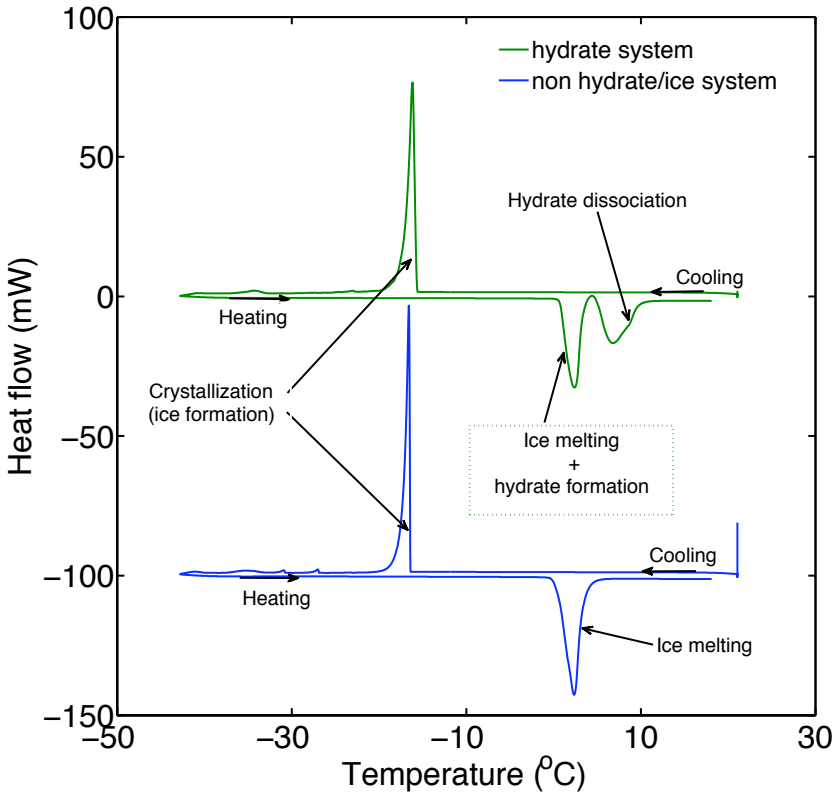

Figure 2.2: μDSC thermographs for hydrate (green) and non-hydrate/ice (blue) forming emulsions (40% w/o), heating and cooling rate = 1°C/min. Data for the ice case is shifted downward for clarity.

observed for bulk water. We note similar observations by Drelich et al. [41], who studied a water-in-paraffin oil emulsion using the same surfactant (Span 80) as used in our study. These authors reported a shift in the freezing exotherm, from -38°C at mixing ($t = 0$), to -18°C after one day. There is some asymmetry exhibited by the exothermic peak at the higher temperature of Drelich et al., with only slight change in the drop size distribution one day after emulsification. Drelich et al. show their emulsions to be flocculated, and suggest the possibility of interfacial molecular arrangements, *e.g.* reverse micelle or ordered mutilayer formation, of Span 80 at the water-oil interface acting as agents for heterogeneous ice nucleation as an explanation for the shift to a higher conversion temperature. For the purposes of the present work, the key issue is that the emulsion is stable until the conversion to ice takes place, so that a dispersed high-interface system is present when the hydrate formation takes place in the warming part of the cycle.

In Figure 2.2, we also see a very small exothermic peak close to -35°C. Drelich et al. also reported the appearance of a similar small exothermic peak and reported that it progressively disappears with time. Noting that it has long been known, at least since the work of Carte [42], that the freezing temperature for water drops decreases as the drop size goes down, this suggests the presence of very fine liquid drops which remain unconverted after the vast majority of the water converts. In fact, emulsions containing a large number of drops in a single sample may allow better control over the statistical analysis of freezing experiments as compared to isolated single drops. Using this concept, Clausse et al. [43] reported that for the emulsions in their study, the most probable temperature of solidification decreases exponentially as the radius of a water drop becomes smaller.

A similar DSC temperature protocol is applied to a mixture of pure cyclopentane and water without surfactant. This forms a segregated (layered) system. Figure

2.3 shows a DSC thermograph for an equimolar mixture of cyclopentane and water. Cyclopentane is much in excess of the stoichiometric requirement for conversion of water to hydrate. Similar to the emulsion studies, an exothermic peak is observed during a cooling ramp corresponding to ice formation. However, during the heating ramp, there is only one endotherm, corresponding to ice melting. There is no signature of cyclopentane hydrate dissociation. Hydrates are absent or present in too small a quantity to be detected by μDSC. We see that hydrate formation is an interfacial phenomenon depending on the availability of interfacial area between the water and the hydrate former phase. Interfacial area is estimated to be two orders of magnitude higher for the emulsions prepared here (assuming drop diameter of 50 μm) than in the segregated system.

In Figure 2.2 the ice melting endotherm in the hydrate-forming emulsion appears to be weaker than that of the ice-forming emulsion; for details, see Figure 2.4. For the same internal phase fraction emulsions, in case of pure ice melting, heat flow per unit mass of crystallized water (as determined from an exothermic peak) should be the same unless there is another phase transition taking place simultaneously. The upward shifting of the endotherm is thus the result of the exothermic hydrate formation. Hydrate formation occurs simultaneously with ice melting as soon as there is free (*i.e.* liquid) water at the oil interface.

Hydrate conversion analysis method:

The area under the single exothermic peak during cooling provides the heat associated with ice formation. Recall the assumption that exclusively ice formation takes place during cooling. This heat is divided by the ice fusion enthalpy, ΔH_{ice}, of 333.55 J/g water, to provide the total mass of water, which we will call A. We assume this as the total water content of the emulsion sample and calculate the heat flow per

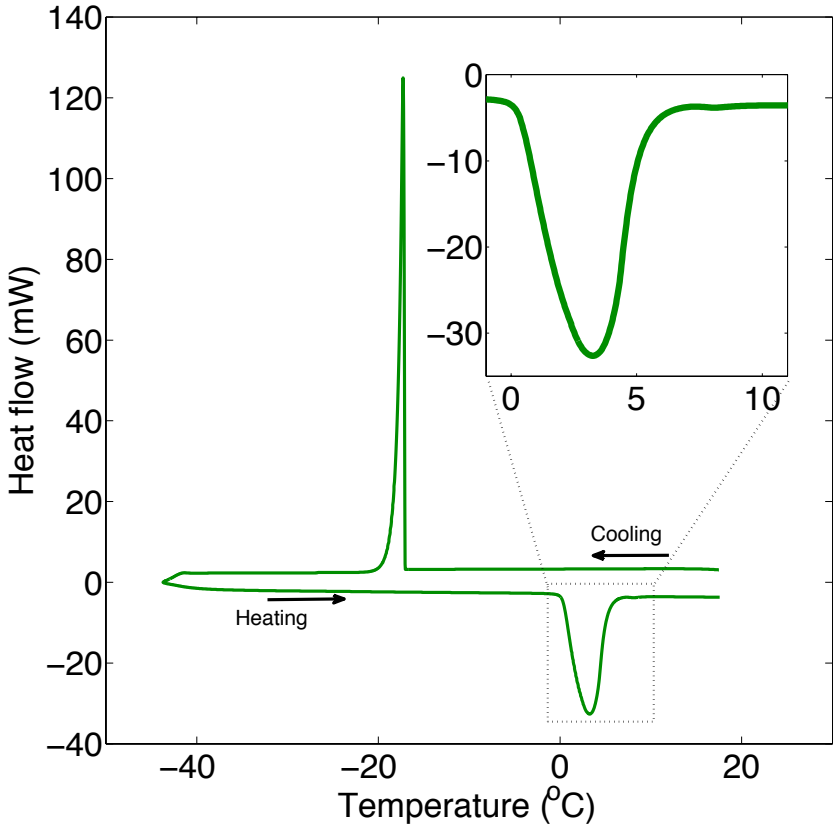

Figure 2.3: μDSC thermographs for equimolar cyclopentane-water mixture with no surfactant (segregated system), heating and cooling rate = 1°C/min, (inset shows the absence of second endothermic peak corresponding to hydrate dissociation).

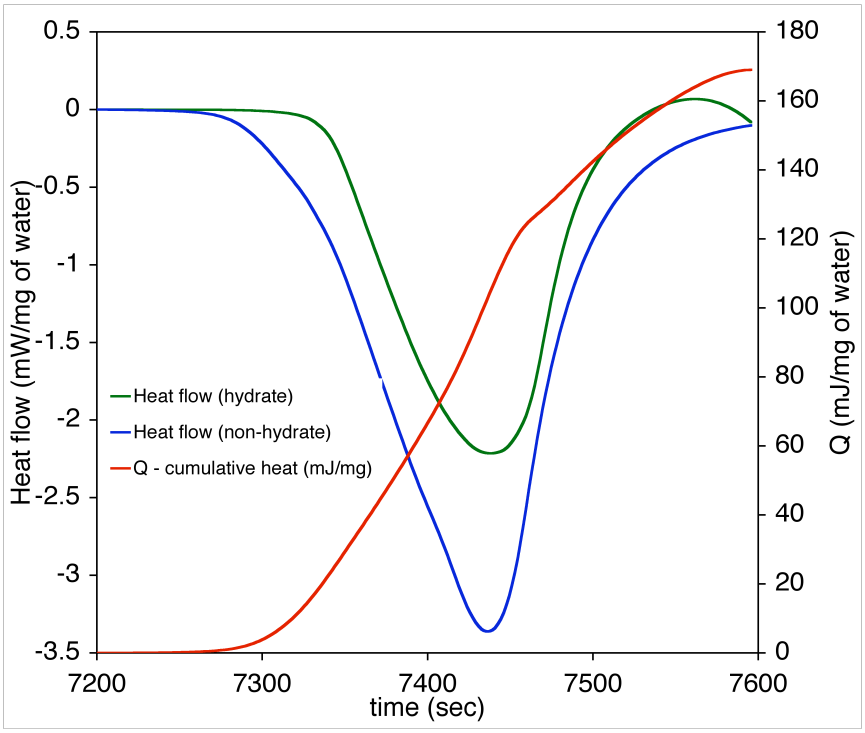

Figure 2.4: Endotherms for 40% *w/o* emulsion from Figure 2.2, hydrate (green) and non-hydrate/ice (blue). $T_{(t=7200seconds)}$=-2.82°C, heating rate = 1°C/min. Red line: cumulative area between the heat flow curves.

unit mass of water based on this amount. At a particular instant during the heating cycle a fraction of ice melts; assume a mass B of liquid water is obtained through ice melting. Only free liquid water can undergo clathrate hydrate formation and if a mass C of the liquid water converts into hydrates, we see that $C \leqslant B \leqslant A$. The fractional conversion of total ice into liquid water (X_w) and into hydrates (X_h) can be defined by the ratios $\frac{B}{A}$ and $\frac{C}{A}$, respectively. Since we do not have direct measures of the masses A, B, or C, we use heat flows from μDSC to calculate these conversions.

Our analysis of the level of conversion of water to hydrates is thus based on computation of the cumulative area between the ice melting endotherms from experiments with otherwise identically prepared hydrate- and ice-forming emulsions. This area translates to the amount of heat associated with the exothermic hydrate formation (see Figure 2.4). The hydrate formation heat agrees with the heat deduced from the area under the hydrate dissociation peak, with an average difference of 7±3%. Thus the predominant hydrate formation occurs during ice melting when liquid water becomes available. This agrees with the argument that predominantly ice formation, with little or no hydrate formation, occurs during cooling.

The amount of heat from exothermic hydrate formation can be easily used to compute the fraction of water converted into hydrates using cyclopentane hydrate enthalpy of formation, with the best estimate being $\Delta H_{CPhyd} = 269$ J/g water [18] for the enthalpy of cyclopentane hydrate dissociation to liquid water and liquid cyclopentane. Zhang et al. [18] also reported, by adding the enthalpy of vaporization of cyclopentane (28 kJ/mol), the heat of dissociation to liquid water and cyclopentane vapor as 346.4 J/g water; this is in reasonable agreement with the dissociation enthalpy value of 321.2 J/g water, obtained from application of the Clausius-Clapeyron equation to the hydrate-liquid water-vapor three phase equilibrium data for cyclopentane hydrates reported by Fan et al. [44].

Using $\Delta H_{CPhyd} = 269$ J/g water, the cumulative area between the ice melting endotherms of hydrate- and ice-forming emulsions (as shown in Figure 2.4), which we denote as Q (J/g water), can provide the amount of water in the form of cyclopentane hydrates. The ratio ($Q/\Delta H_{CPhyd} = C/A$ in the terms of the discussion of the prior paragraph) provides the fraction of the total water in the hydrate-forming emulsion that converts to cyclopentane hydrate, and is denoted by X_h. Similarly, using ΔH_{ice} (J/g water), the cumulative area (total heat flow) under the ice melting endotherm for an ice-forming emulsion, $Q_{ice-melting}$ (J/g water), provides the total mass of water melted. This is converted into the fractional conversion of ice (which we assume is the total water content of the emulsion) into liquid water, and denote this fraction as $X_w = Q_{ice-melting}/\Delta H_{ice}$.

We consider the rate of conversion of liquid water into hydrates using the quantities X_h and X_w just defined. The fraction of liquid (or 'free' as it is available for the transition to a clathrate hydrate) water converted into hydrates is described by $Z = \frac{X_h}{X_w}$. The disadvantage of the method is that Z is obtained from the analysis of two separate experiments, and we must assume that hydrate- and ice-forming emulsions follow the same temperature path for ice melting. Nonetheless, the approach provides significant insight. Due to the presence of ice during hydrate formation, it is assumed that there is zero induction time and nucleation occurs immediately [45], when liquid water becomes available from ice melting. The effective elimination of induction time due to presence of ice is clearly observed in single-drop experiments discussed in [37].

For all heating rates (0.25, 0.5 and 1°C/min), the previously described temperature protocol is employed, except that the heating rate may be changed from 1°C/min to 0.25 or 0.5°C/min at -10°C during a heating ramp. A temperature interval from -1°C to 1°C is selected for characterizing the conversion data, as this is when ice begins to melt. A small fraction of the ice melts before the pure water ice melting

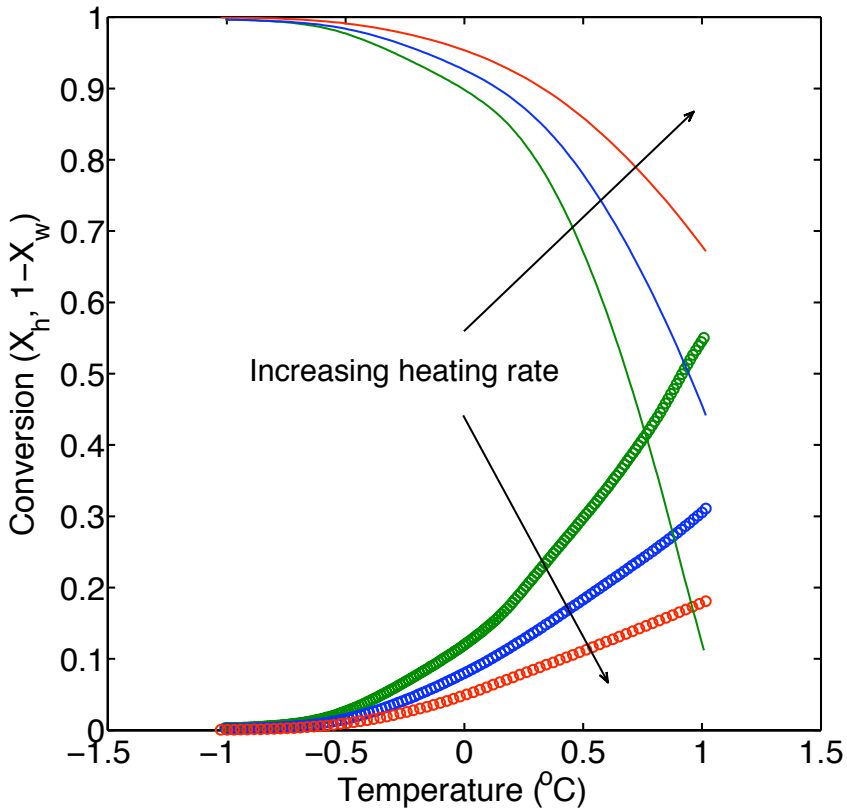

Figure 2.5: Conversion of total water into cyclopentane hydrates (X_h) and free water (X_w) , 40% *w/o* emulsion. green: 0.25°C/min, blue: 0.5°C/min and red: 1°C/min; open circles: X_h, solid lines: (1-X_w).

point of 0°C; this may be due to premelting [46] or due to a melting point depression due to some solubility of surfactant and oil in water. Figure 2.5 shows the evolution of X_h and X_w for the three heating rates in the specified temperature range. Total conversion when the system reaches 1°C is found to increase as the heating rate decreases, apparently due to the greater time for conversion.

Analysis of X_h, X_w and Z for the heating rate of 0.5°C/min is shown in Figure 2.6. The comparison between X_h and X_w shows that in the initial stages the two track very closely, which suggests that all free liquid water is converted into hydrate, *i.e.* $Z \approx 1$. The temperature interval is divided into three sub-intervals as shown in

Figure 2.6. In the first two intervals, -1°C $< T <$ −0.5°C and -0.5°C $< T <$ 0°C, X_h and X_w vary in a similar fashion. In the final interval, 0°C $< T <$ 1°C, X_w increases much more rapidly than X_h, and thus Z decreases.

2.3.2 Mechanism

Figure 2.7 shows the variation of Z, which is found to be independent of the heating rate. In the initial stages Z values greater than unity (*i.e.* $X_h > X_w$) suggest that more water is converted into hydrates than the amount of free liquid water generated through ice melting. This seems unrealistic but recall that the Z values are obtained from two different experiments involving different samples. Based on the regularity of the computed values of $Z > 1$, emulsions that form hydrates may have slightly different X_w compared to a non-hydrate system. One possibility is that energy released through exothermic hydrate formation may lead to added ice melting. For the sake of simplicity, we set the upper limit as $Z = 1$, as shown in Figure 2.6(a), and reconsider the issue below.

The variation of Z suggests that in the initial stage all free water is converted to hydrate. Heat transfer limits the process, as it governs the rate of ice melting. Once the hydrates completely cover the ice ball forming a thin shell of hydrates, diffusion through a solid is necessary for cyclopentane and water to come into contact, so that hydrate growth is severely limited by mass transfer. Further melting of bulk ice produces more free water; owing to diffusional limitations, only a small fraction of the water reacts as indicated by decrease of Z. A pictorial view based on the above explanation is shown in Figure 2.8. The event of cyclopentane hydrate formation can thus be described in three steps:

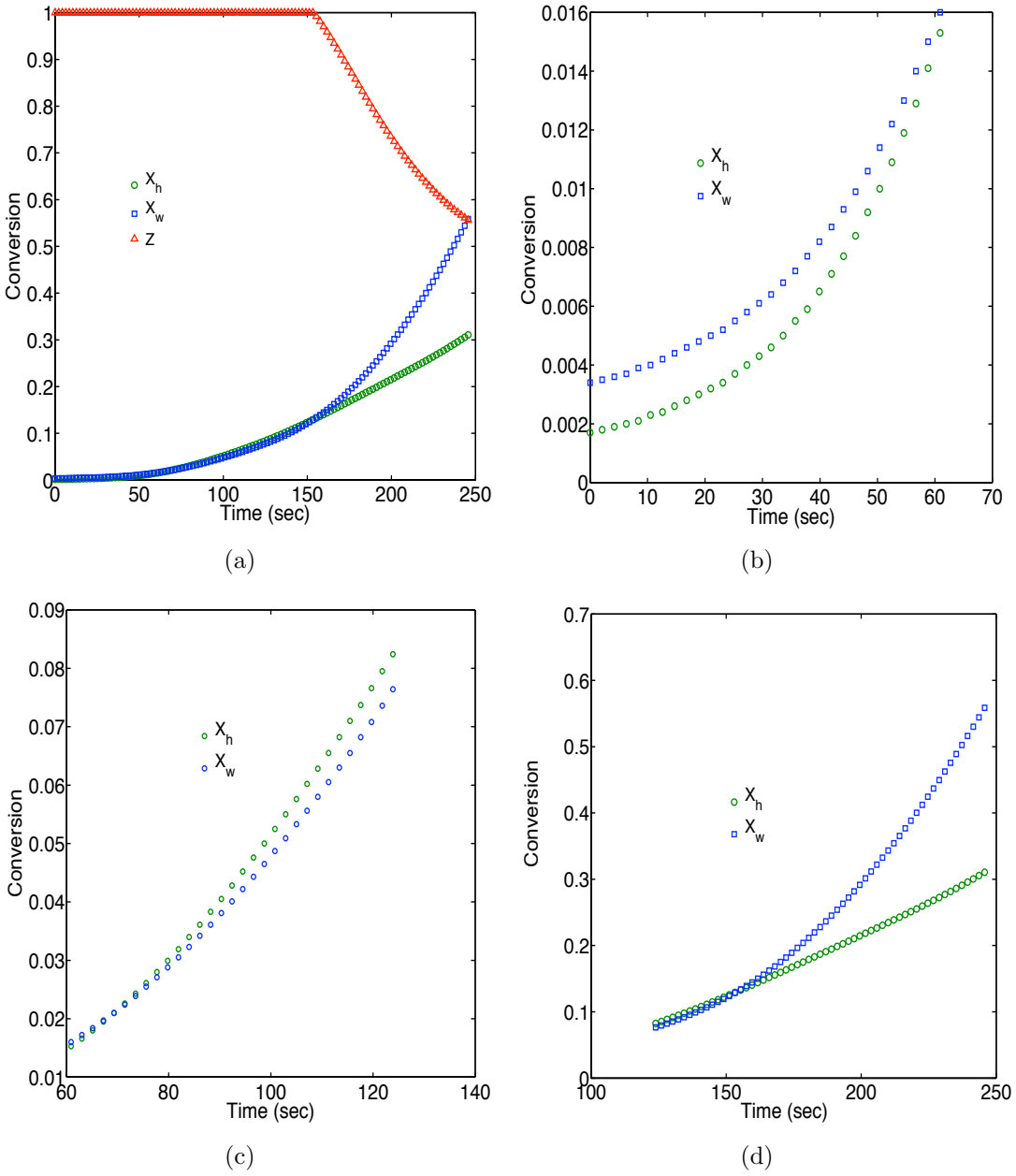

Figure 2.6: (a) -1 to 1°C, (b) -1 to -0.5°C, (c) -0.5 to 0°C, (d) 0 to 1°C; 40% *w/o* emulsion, heating rate = 0.50°C/min. Variation of X_h, X_w and Z in the temperature interval -1°C to 1°C (X_h: circles, X_w: squares and Z:triangles).

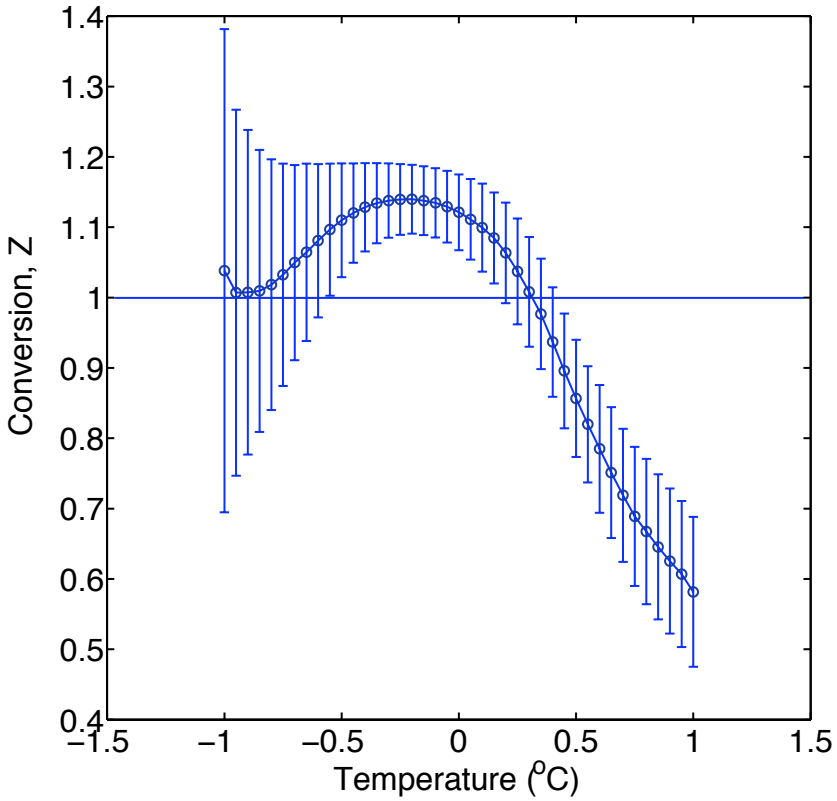

Figure 2.7: Variation of Z for 40% *w/o* emulsion (error bars are standard deviation on six experiments, two for each heating rate).

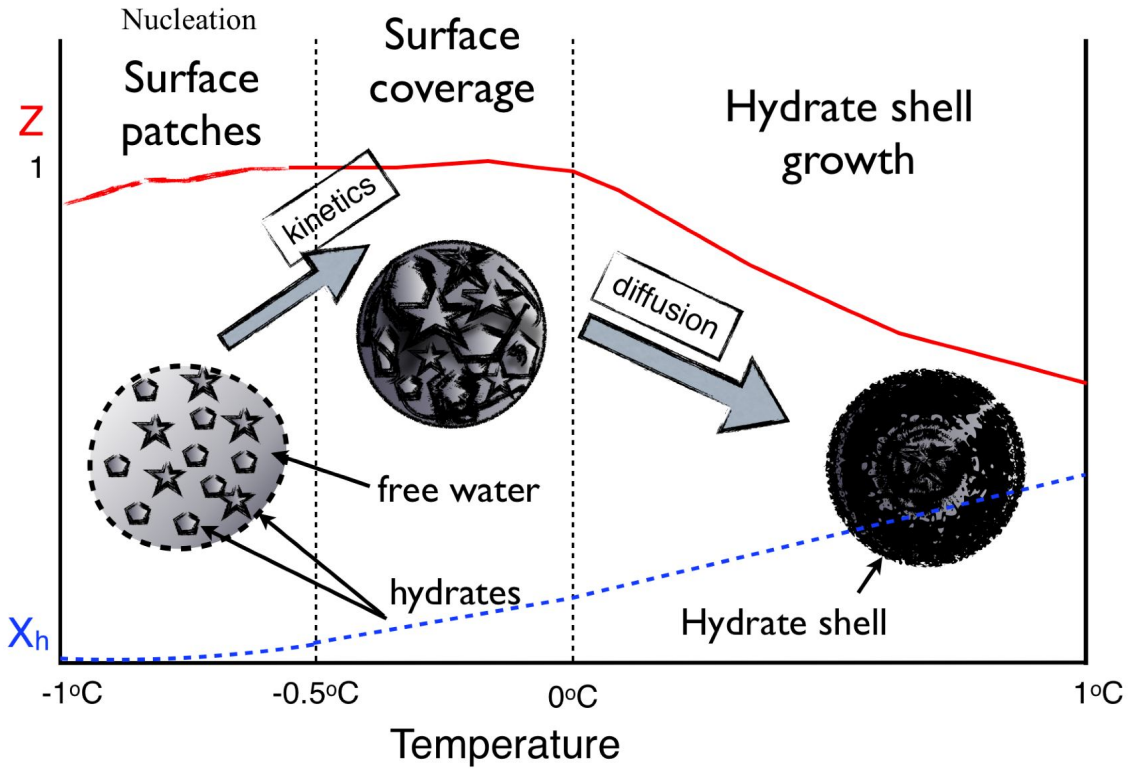

Figure 2.8: Hypothesis of hydrate formation, water drop suspended in an oil phase containing hydrate former (cyclopentane).

Hydrate nucleation:

The initial stage of ice melting leads to availability of free water which reacts completely to cyclopentane hydrate. Nucleation occurs in the free water layer and the presence of ice leads to rapid heterogeneous nucleation. In our system, nucleation is not the rate limiting step, but instead the availability of free water (which is heat transfer limited) controls the rate of hydrate formation from -1 to -0.5°C.

Lateral growth:

Nuclei formed in the free water layer or at the ice surface grow along the surface. As cyclopentane-rich liquid is in direct contact with water, there are no mass transfer limitations. In the absence of surfactants, lateral hydrate growth leads to a thin shell formation around the water drop. Single-drop experiments described afterwards support the view that nucleation occurs randomly at the water-oil interface and crystals grow along the interface leading to a complete surface coverage in the absence of surfactant. This observation is corroborated by recent experiments by Sakemoto et al. [39], who studied cyclopentane hydrate crystal growth at a water-cyclopentane interface. Sakemoto et al. reported a polycrystalline nature of the hydrate shell, similar to the one observed in single drop experiments in our recent work [37].

It is difficult to distinguish the nucleation event from the lateral growth, and thus for simplicity we assume that primary hydrate growth occurs above -0.5°C. Either kinetics or heat transfer controls the growth rate until diffusion dominates when a complete surface coverage is obtained.

The following rate equation represents the cyclopentane hydrate formation,

$$C_5H_{10} + 17H_2O \rightarrow C_5H_{10} \cdot 17H_2O. \tag{2.1}$$

Regardless of whether control is by heat transfer or by chemical kinetics, cyclopentane is present in excess and the rate of water consumption can be written as,

$$\frac{dm_{H_2O}}{dt} = -m^o_{H_2O}\left(\frac{dX_h}{dt}\right) = -m^o_{H_2O} \cdot K, \tag{2.2}$$

where m_{H_2O} is the mass of water and $m^o_{H_2O}$ represents the total water mass. X_h is the fractional conversion of water into hydrates, *i.e.* $m_{H_2O} = m^o_{H_2O}$·(1-X_h).

In the temperature interval from -0.5 to 0°C, X_h follows a linear profile and thus the rate of water consumption is constant at $m^o_{H_2O} \cdot K$ (gm/s). Table 2.3 shows the constant K (s^{-1}) for the hydrate growth, corresponding to the fractional conversion of water into hydrates per unit time (dX_h/dt).

Radial growth:

Once a complete layer of hydrates covers the drop, the rate is governed by mass transfer through the hydrate shell. For a simple shell model described below, diffusion of cyclopentane through the hydrate shell towards the bulk water determines the rate of radial growth (temperature: $\gtrsim$ 0°C). In the presence of oil-soluble surfactants, the radial growth is not simply a diffusion process and it is observed that radial hydrate growth follows lateral growth without a complete hydrate shell formation [37], see Chapter 3 for more details.

2.3.3 Modeling

We present here a brief analysis of the shell model, assuming uniformity of the properties of the shell. This is expected to be inadequate based on the noted polycrystalline nature of the surface observed in the formation of the shell in experiments with larger drops [37].

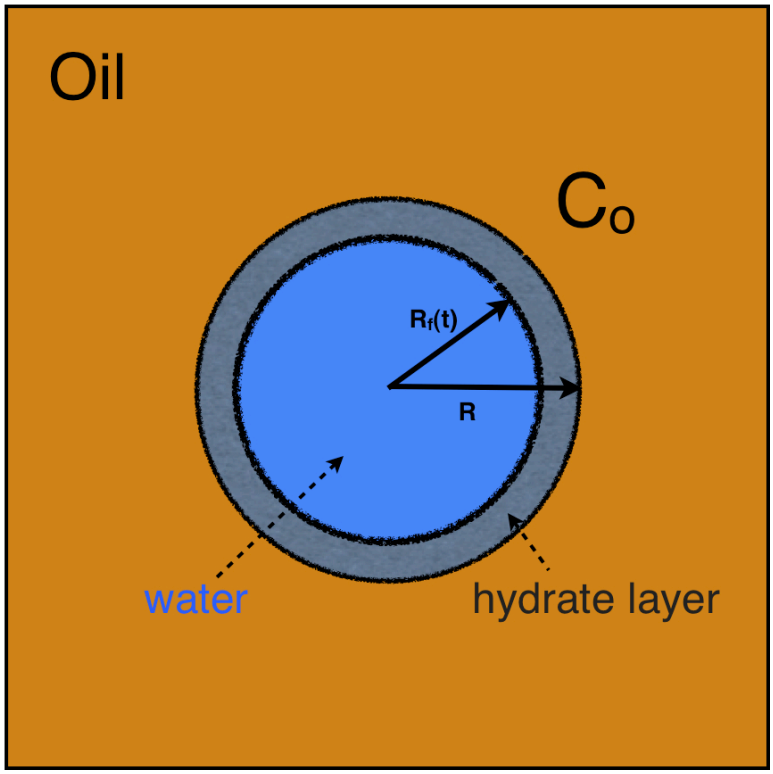

Figure 2.9: Schematic of the water drop in a pool of oil, with inward radial hydrate growth.

Figure 2.9 shows a schematic of the system under consideration. A water drop of radius R is suspended in an oil phase containing 50% by volume cyclopentane, C_o, similar to DSC studies. The entire drop is initially liquid and a hydrate front then propagates inward, with R_f the position of the hydrate front.

In the freezing of food and other biomaterials, tissue damage may arise due to mechanical stresses associated with expansion at the phase change from liquid water to ice. Analyses of these systems [47, 48] are followed for calculation of the stresses in the hydrate shell. We assume spherical symmetry, which we expect leads to upper bounds on stresses in the shell-drop configuration of Figure 2.9.

With spherical symmetry, the equation of mechanical equilibrium is

$$\frac{d\sigma_r}{dr} + \frac{2}{r}(\sigma_r - \sigma_\theta) = 0, \tag{2.3}$$

and strains are related to displacements as

$$\epsilon_r = \frac{du}{dr}; \quad \epsilon_\theta = \frac{u}{r}, \tag{2.4}$$

where σ is the stress, ϵ is the strain (subscripts r and θ for the radial and tangential components respectively), and u is the radial displacement. Boundary conditions are zero radial stress on the outer surface,

$$\sigma_r(R) = 0, \tag{2.5}$$

and continuity of radial stress and displacement at the hydrate front,

$$\sigma_r(R_f)|_1 = \sigma_r(R_f)|_2, \tag{2.6}$$

and

$$\epsilon_\theta(R_f)|_1 = \epsilon_\theta(R_f)|_2, \tag{2.7}$$

where the indices 1 and 2 represent the water core and the hydrate shell, respectively.

These equations can be solved for the core liquid pressure p_1 and shell deviatoric stress $\sigma_r - \sigma_\theta$, as shown in detail elsewhere [47]:

$$p_1 = \frac{2}{9}\frac{E\Delta e}{(1-\nu)}\left[1 - 3\ln\left(\frac{R}{R_f}\right) - \left(\frac{R_f}{R}\right)^3\right], \tag{2.8}$$

for $0 < r < R_f$, and

$$\sigma_r - \sigma_\theta = \frac{E\Delta e}{3(1-\nu)}\left[\left(\frac{R_f}{r}\right)^3 - 1\right], \tag{2.9}$$

for $R_f < r < R$. Here, E is the elastic modulus, and ν is the Poisson ratio (assumed to be 0.33, as for ice), both for the solid shell material, and Δe is the volumetric strain owing to the liquid-to-solid phase change.

For lack of a better value, the cyclopentane hydrate density is calculated using the estimation formula provided by Sloan [45] assuming complete occupancy of large cavities:

$$\rho = \frac{N_w MW_{H_2O} + y_1 \upsilon_1 MW_{CP} + y_2 \upsilon_2 MW_{CP}}{N_{Avo} V_{cell}}, \tag{2.10}$$

where ρ is density, $N_w = 136$ is the number of water molecules per unit cell, MW is molecular weight, y is the fractional occupancy of a type of cavity, and υ is the number of cavities per water molecule. The subscripts 1 and 2 represent the small and large cavity, respectively so that y_1=0, y_2=1 here, with υ_1=16 and υ_2=8. The volume of unit cell is $V_{cell} = (17.3 \times 10^{-10})^3$ m^3, and N_{Avo} Avogadro's number. The parameter values for cyclopentane hydrates are taken from [45]. The density obtained for cyclopentane hydrates is 0.965 gm/cm^3 and the corresponding Δe is 0.036, while this value is 0.091 for ice.

Figure 2.10 shows the predicted variation of stress across the hydrate shell for different shell thickness and a comparison with the reported values for ice formation by the same diffusion-limited shell growth mechanism[1]. The lowest R_f/R attainable is 0.58 which corresponds to the conversion of 0.8, the maximum conversion observed in DSC experiments. This shows that stresses reach large values in the shell for the

[1]Note that once subcooled, a water drop may nucleate and freeze rapidly throughout its volume, so this mechanism must be assumed. For the cyclopentane hydrate formation (and for other hydrate formers with negligible solubility in water), mass transfer limitations require growth at the interface between the two fluids and thus the mechanism is a natural first step, even if incomplete.

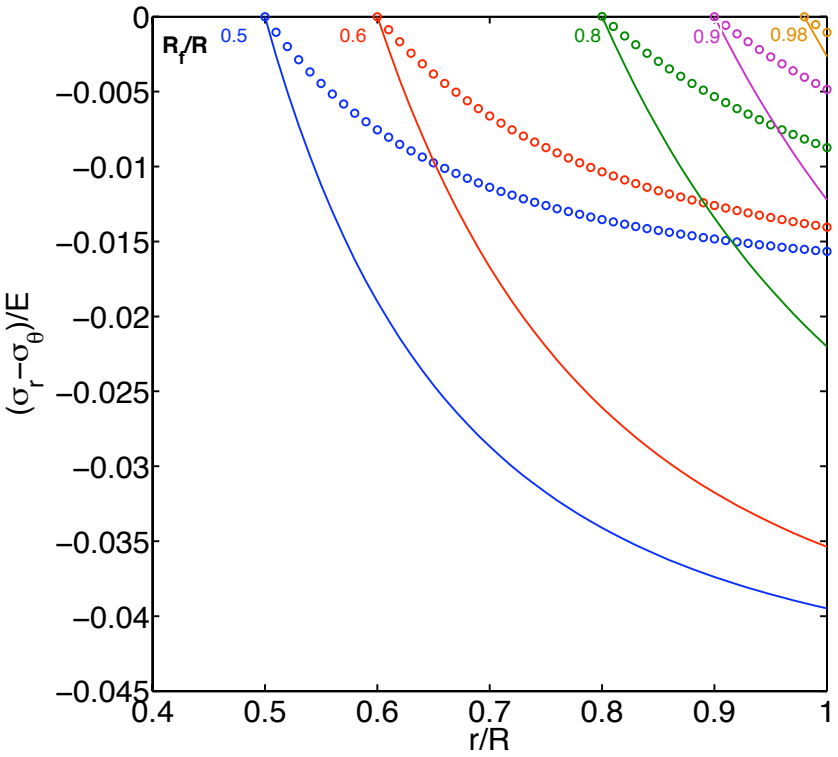

Figure 2.10: Deviatoric stress distribution, solid line: ice ($\Delta e = 0.0907$) and open circles: hydrate ($\Delta e = 0.036$).

assumed hydrate density. The response of the shell material to such stresses depends on the yield strength of the shell material, and this is an issue clouded by lack of information: even the bulk yield stress is not very well known for most hydrates (and cyclopentane hydrates in particular), and the actual response may be a rather complex system-dependent issue as opposed to a well-defined property owing to the polycrystalline nature of the shell.

To relate our results to a known analytical model for the shell growth, we use the shrinking core model as described by Fogler [49]. Recall that all μDSC results used for comparison in this section are obtained for systems with Span 80 surfactant present at 0.1% (v/v). In studies related to morphological characterization of cyclopentane hydrates in the presence of Span 80, we will see that not a simple diffusion but a

complicated sequence of crystal detachment from the interface into the bulk water followed by the exposure of free water to the oil phase is the mechanism for the radial hydrate growth. Though the shrinking core model is an over-simplified description of hydrate shell growth, we find it useful to develop the predictions of this model to allow comparison with our results.

Using the solution methodology as described by Fogler [49], we can write the molar flux of cyclopentane as:

$$J_{CP} = -D_e \frac{dC_{CP}}{dr} = \frac{-D_e C_o}{(1/R_f - 1/R)r^2}. \tag{2.11}$$

An overall balance on water gives

$$r''_w \times 4\pi R_f^2 = \frac{d(\frac{4}{3}\pi R_f^3 \rho_w)}{dt}, \tag{2.12}$$

where r''_w is the water consumed per unit area, and ρ_w is the molar density of water.

The rate of disappearance of water balances the molar flux of cyclopentane at the interface,

$$-r''_w = -17 \times J_{CP}|_{r=R_f} = \frac{17 D_e C_o}{(R_f - R_f^2/R)}, \tag{2.13}$$

using the stoichiometry given by (2.1). Assuming that initial hydrate layer thickness, at $t = 0$, is small compared to R we write $R_f = R$ at $t = 0$, which gives

$$t = \frac{\rho_w R^2}{102 D_e C_o} \left[1 - 3\left(\frac{R_f}{R}\right)^2 + 2\left(\frac{R_f}{R}\right)^3\right], \tag{2.14}$$

where t is the time at which the hydrate-water interface (or hydrate front) is at R_f. The ratio (R_f/R) can be easily obtained from X_h: $(R_f/R) = (1\text{-}X_h)^{1/3}$ and the unknown D_e/R^2 can be calculated.

Fitting our experimental data for X_h from μDSC to the equation (2.14) and taking the measured $R = 20$ μm, we determine the effective diffusivity of cyclopentane through the hydrate layer based on the shrinking-core model; note, however, that Davies et al. [33] have shown that water is the more mobile species, and our model simplifies the transport without accounting for this factor. The amount of free water generated from ice melting up to 1°C increases with decreasing heating rate, apparently owing to more time for ice melting (refer Figure 2.5). Diffusion through liquid water is more rapid than through solid ice, which may explain the decreasing trend of diffusivity with cooling rate. The mean diffusivity value obtained is (1.71 $\pm$ 0.5)$\times 10^{-14}$ m^2/s. This value is over 100 times larger than the diffusivity reported for methane diffusion through a film by Turner et al. [50], also based on analysis of the shrinking core model. This suggests that the morphology of the hydrate is not a robust shell under the conditions studied here, and the present data must be interpreted with a detailed understanding of morphological characteristics.

Heating rate (°C/min)	K (s^{-1})	D_e (m^2/s)
0.25	7.77×10^{-4}	2.35×10^{-14}
0.50	10.79×10^{-4}	1.64×10^{-14}
1.00	12.91×10^{-4}	1.15×10^{-14}

Table 2.3: Coefficients: hydrate formation model.

2.4 Conclusion

Cyclopentane hydrate formation is an interfacial process, as is expected for gas hydrates as well. The availability of large interfacial area between the hydrate former phase and water in an emulsion system leads to vastly more hydrate formation than

in a segregated water-oil system. We have analyzed the hydrate formation in water-in-oil emulsions relevant to oil-field emulsions, with contributions to the DSC analysis and the mechanical understanding of the material.

Through a kinetic analysis based on comparing the heat flow curves from μDSC for hydrate and non-hydrate (ice-forming) emulsions, we provide information about the hydrate formation mechanism in these mixtures. Hydrate formation apparently proceeds in three steps: (i) nucleation, (ii) lateral surface growth and (iii) radial growth and a proposed mechanism for the hydrate formation has been postulated. The mechanical stresses developed in the hydrate shell due to volume expansion associated with hydrate formation are large and expected to play a major role in determining the surface morphology of hydrates. A detailed discussion on the morphological characteristics of cyclopentane hydrate formation at a single water drop suspended in the oil phase, as in the case with *w/o* emulsion studied here, is presented in the following chapter.

Chapter 3

Surfactant effects on cyclopentane hydrate morphology

3.1 Introduction

Rheological properties of multiphase systems like emulsions, suspensions or polymer blends predominantly depend on the microscopic structure of the developing phases, thereby making the morphological characterization an integral part in understanding the complex fluid behavior. Along with other parameters like external flow field, oil and water properties and presence of chemical additives, morphology of hydrate particles is one of the key issues in the hydrate agglomeration process and thus factors into the mechanical strength of hydrate plug to a large extent. The focus of this chapter is on the crystal morphology during hydrate growth at water drops dispersed into the oil phase, *i.e.* in case of water-in-oil (w/o) emulsions. Instead of multiple water drops as in case of an emulsion, efforts have been made to understand the morphological development of hydrate growth at a single water drop suspended in the oil phase.

As concluded from the calorimetric analysis, hydrate formation is an interfacial process occuring at the water-oil interface, and thus interfacial properties are expected

to have a significant impact on the hydrate crystal growth and the resulting morphology. To this end, addition of surfactants like sodium dodecyl sulphate (SDS) into the water phase have been shown to increases the rate of gas hydrate formation. Zhong et al. [51] studied the effect of SDS on ethane hydrate formation in a two phase gas-water system. They suggested that surfactant micelles act as nucleation points by increasing the solubility of gas in water and hydrate crystals form around the micelles in the water below the gas-water interface. They also found a decreased induction time and almost 700 times faster hydrate formation rate as compared to a system without SDS.

In terms of morphological characteristics of hydrates through direct visualization, Ohmura et al. [52, 53] reported the morphology of hydrochlorofluorocarbon (CH_3CCl_2F) and CO_2 hydrates, Servio et al. [54] analyzed methane and CO_2 hydrate morphologies, Tanaka et al. [55] and Saito et al. [56] studied single component and mixed gas hydrate formation. Bruusgaard et al. [57] studied the effect of biological and polymeric kinetic inhibitors on methane hydrate morphology while Okutani et al. [58] and Yoslim et al. [59] studied the effect of different sodium alkyl sulphate aqueous solutions on the gas hydrate formation and reported a mushy hydrate morphology obtained due to extensive hydrate growth in the presence of surfactant. A review by Sun et al. [60] summarizes the studies on gas hydrate film growth rate, morphology and related modeling efforts.

As noted, hydrate formation is an interfacial process and thus depends on the interfacial characteristics of the system as well as the concentration or activity of the hydrate former. Crude oils contain many naturally occurring chemical species like paraffins, aromatics, asphaltenes, resins, acids or other externally added components like kinetic and thermodynamic hydrate inhibitors, anti-agglomerants, demulsifiers, anti-foaming agents, corrosion and scale inhibitors. Each crude oil has its own

properties depending on the unique mixture of these components. Høiland et al. [61] and Fotland et al. [62] studied the wettability of hydrates in a water-crude oil system. Høiland et al. compared the emulsion inversion point of 12 different crude oils with and without hydrate particles and showed that wettability of hydrates depends on the oil composition. Two of their crude oils which led to oil-wet hydrates, possibly due to adsorption of some natural surface active components of oil on the hydrate surface, showed low plugging tendency. Other oils which lead to intermediate or water-wet hydrates showed high risk of plugging. Fotland et al. discussed wettability diagrams illustrating all possible wettability states and their analysis showed that capillary forces dominate buoyancy and turbulence forces when the hydrate crystals are less than 10^{-3} m in diameter, but the effects of wetting can be observed at all levels. Sjöblom et al. [63] studied three different crude oils and compared the hydrate plug formation properties with asphaltenes and acids removed from the crude oil. Removal of asphaltenes led to decreased emulsion/hydrate dispersion stability and more plugging tendency while removal of acids caused asphaltene precipitation at the water/hydrate-oil interface increasing the emulsion/hydrate dispersion stability and thus less plugging tendency. Thus the crude oil properties appear to have a key role in controlling the hydrate behavior. A recent review by Zerpa et al. [64] discusses the importance of surface chemistry in hydrate flow assurance.

Though efforts have been made to study the effect of oil properties on the hydrate behavior, very few studies deal with the hydrate crystal morphology at the water-oil interface and the effect of oil-soluble surfactants, as the bulk of morphology studies in the past are focussed on the water-gas systems. To briefly review the studies dealing with water-oil systems, Sakaguchi et al. [65] studied hydrate formation at the CH_3CCl_2F-water interface with the effect of kinetic inhibitors (KI) including poly(N-vinylpyrrolidone) (PVP) and poly(N-vinylcaprolactum) (PVCap). Lee et al. [66] and

Kumar et al. [67] studied the effect of PVP on the methane and propane mixed gas hydrate formation at the heptane-water interface. Taylor et al. [68] and Sakemoto et al. [39] studied cyclopentane hydrate formation at the water-cyclopentane interface but without any surfactant present in the system. Nakajima et al. [14] observed a mass of granular hydrates in their study of hydrate-forming cyclopentane-in-water emulsions with the main focus on the potential application as a thermal energy storage media. Aman et al. [69] studied the effect of commercially available additives on the inter-particle adhesion force between cyclopentane hydrate particles in the oil phase and observed an increased surface roughness with hair-like hydrate morphology when Span 80 is present in the oil phase. A similar hair-like cyclopentane hydrate morphology is also reported in a recently published hydrate emulsion calorimetry study [38].

Better flow assurance mitigation strategies call for a detailed understanding of the effect of naturally occurring oil-soluble surface-active components on the hydrate morphology. From a flow assurance perspective in case of oil-dominated systems, *i.e.* *w/o* emulsion transport, we study cyclopentane hydrate formation at a millimeter-scale water drop suspended in cyclopentane. This chapter demonstrates the effect of commercially available oil-soluble surfactant, Span 80, used as an emulsifier in the previous emulsion studies [38, 70] and a water-soluble anti-agglomerant (AA) on the crystal morphology of cyclopentane hydrate at the water-cyclopetane interface. We begin in the next section with a description of experiments, followed by a description of cyclopentane hydrate morphology in the absence of surfactant, where a faceted polycrystalline hydrate shell is formed around the water drop. A unique three-dimensional (3D) hollow-conical crystal is observed at Span 80 concentrations greater than 0.01% by volume in cyclopentane. The conical crystals have a polygonal base, usually hexagonal, which is pinned at the water-cyclopentane interface; growth

occurs at this base and drives the previously-formed crystal into the water phase. A hypothesis that a mechanical barrier generated by crowding of surfactant molecules at the interface is responsible for the observed hollow-conical crystal shape is supported by experiments at variable surfactant concentrations and temperatures. The final morphology observed in the presence of Span 80 is hairy or mushy exhibiting significant porosity and the steps leading to such hairy and porous morphology are discussed. This is followed by discussion on the AA effect on cyclopentane hydrate growth, which is shown to completely eliminate the effect of Span 80 responsible for the observed hairy hydrate growth. Preliminary results for a high-pressure propane hydrate morphology at a single water drop suspended in mineral oil are presented and they show very promising similarities with the model cyclopentane hydrate properties.

3.2 Experiments

3.2.1 Single drop morphology setup

Figure 3.1 shows the experimental setup, which includes an aluminum microscope slide with a circular well of 12.5 mm diameter and 2 mm in depth. The well is filled with cyclopentane (density approximately 0.75 g/cm^3) and a 4 μL drop of the denser (approximately 1.0 g/cm^3) water is placed in the center, so that it sits on the bottom. A typical temperature protocol is to decrease the temperature to -25°C to convert the water drop to ice and then increase the temperature to $T_{\text{hold}} = 0.2$ °C, with a temperature ramp of 5°C/min in each direction. The temperature is then held fixed at 0.2°C (or other values of T_{hold} below the cyclopentane hydrate equilibrium dissociation temperature of $T_{\text{eqm}} \approx 7$ °C) to melt the ice. It is found that water from freshly melted ice leads to immediate hydrate formation, overcoming the extended and

stochastic induction time associated with cyclopentane hydrate nucleation. A Linkam Peltier stage (LTS 120) with a quartz visualization window is used for temperature control, as shown by Figure 3.1(b). A Sony digital camera XCD-SX 910 equipped with an imaging lens and Nikon AZ100 microscope are alternatively used for the image acquisition.

For high-pressure gas hydrate studies, a high-pressure Linkam Peltier stage THMS600-PS is used. The sample chamber can be pressurized up to 14 bar and liquid nitrogen cooling system LNP95 allows cooling to -120°C.

3.2.2 Pendant drop tensiometer

KSV Theta Optical Tensiometer is used for the interfacial tension measurements. A gas-tight glass syringe filled with an oil phase is fixed to an inverted needle (J type). A pendant drop of oil is produced inside the water phase contained in the quartz cell. The pendant drop shape is fitted with the Young-Laplace equation for the interfacial tension measurements. The surface tension of pure water obtained using this technique is 72.8 mN/m at 25°C; an air bubble replaces the oil drop for this measurement.

3.3 Results and discussion

3.3.1 Surfactant free case

Figure 3.2 shows the morphology of cyclopentane hydrate crystals formed with a water drop immersed in cyclopentane alone, with no surfactant. Hydrate nucleation occurs, apparently randomly, at the water-cyclopentane interface as soon as free liquid water becomes available through ice melting. Hydrate nuclei grow laterally along the

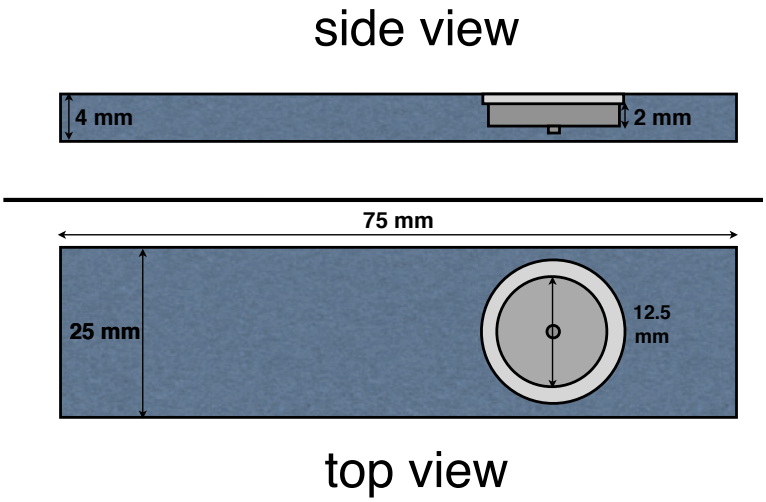

(a) Aluminum microscope slide

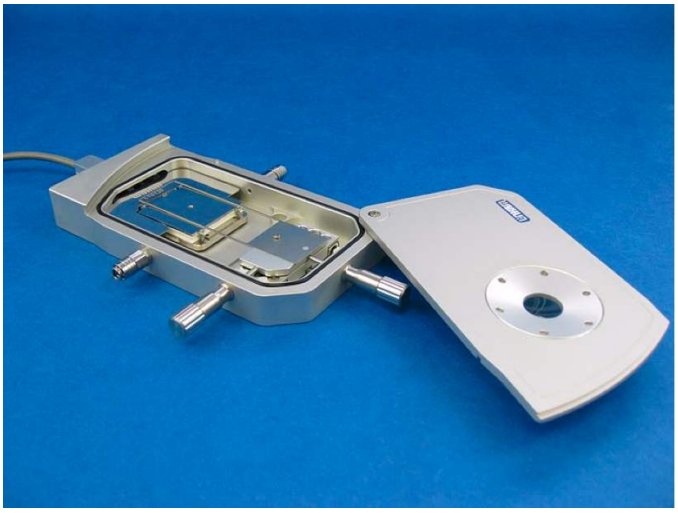

(b) Linkam Peltier stage, LTS 120

Figure 3.1: Crystal visualization chamber: aluminum slide with circular well inside a stage with Peltier temperature control (Linkam LTS 120) and a quartz viewing window.

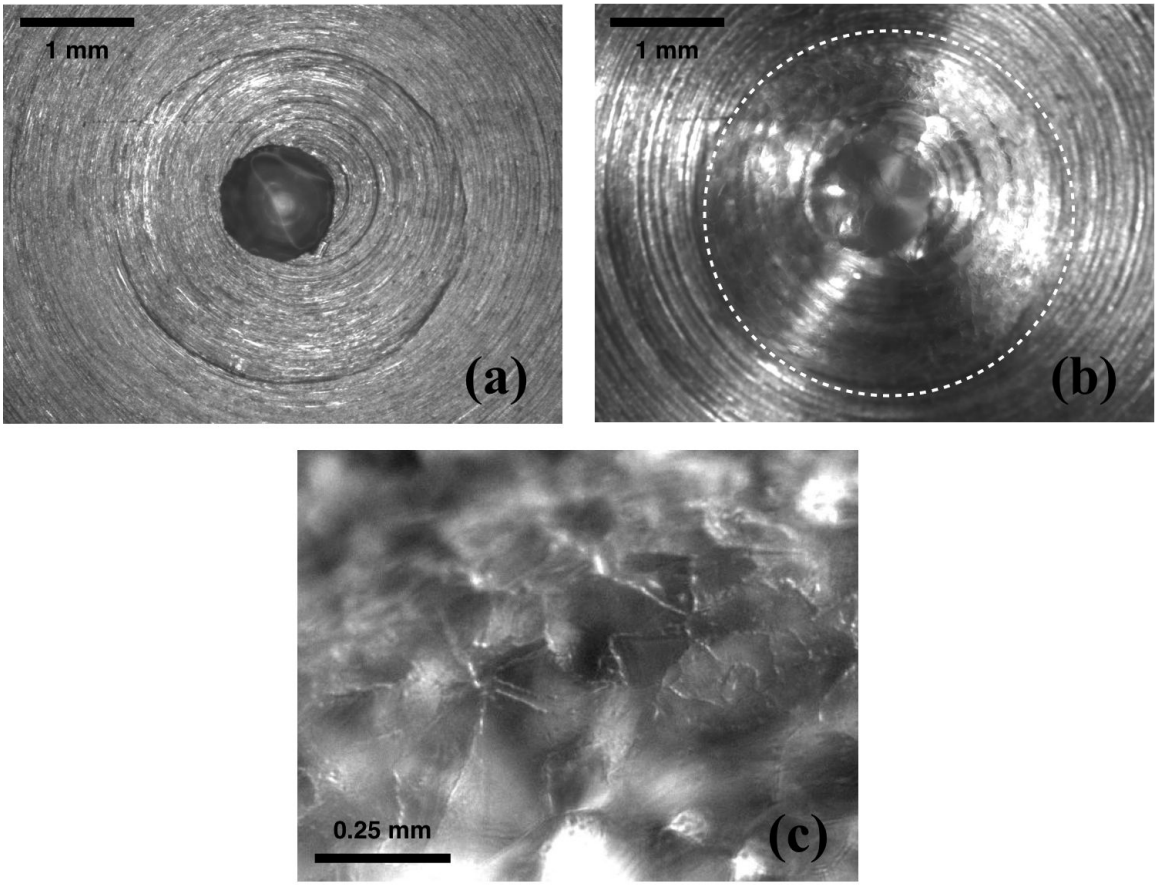

Figure 3.2: Faceted cyclopentane hydrate shell morphology: oil phase is pure cyclopentane with no surfactant, $T = 0.2^{o}$C (a) initial water drop, (b) white dotted line distinguishes between hydrate ball and aluminum surface, (c) enlarged view of the hydrate ball.

water drop surface leading to a faceted, polycrystalline hydrate shell as shown in Figure 3.2(c). Figure 3.3 shows images of the faceted hydrate shell morphology obtained from a different experimental set up. The shell formed by the joining of numerous hydrate facets slows further hydrate formation due to mass transfer limitations.

A similar faceted hydrate shell formation at the water-cyclopentane interface has been reported in [68, 39]. Taylor et al. [68] reported that a thin hydrate shell formation around the water drop slows down further hydrate growth and over time,

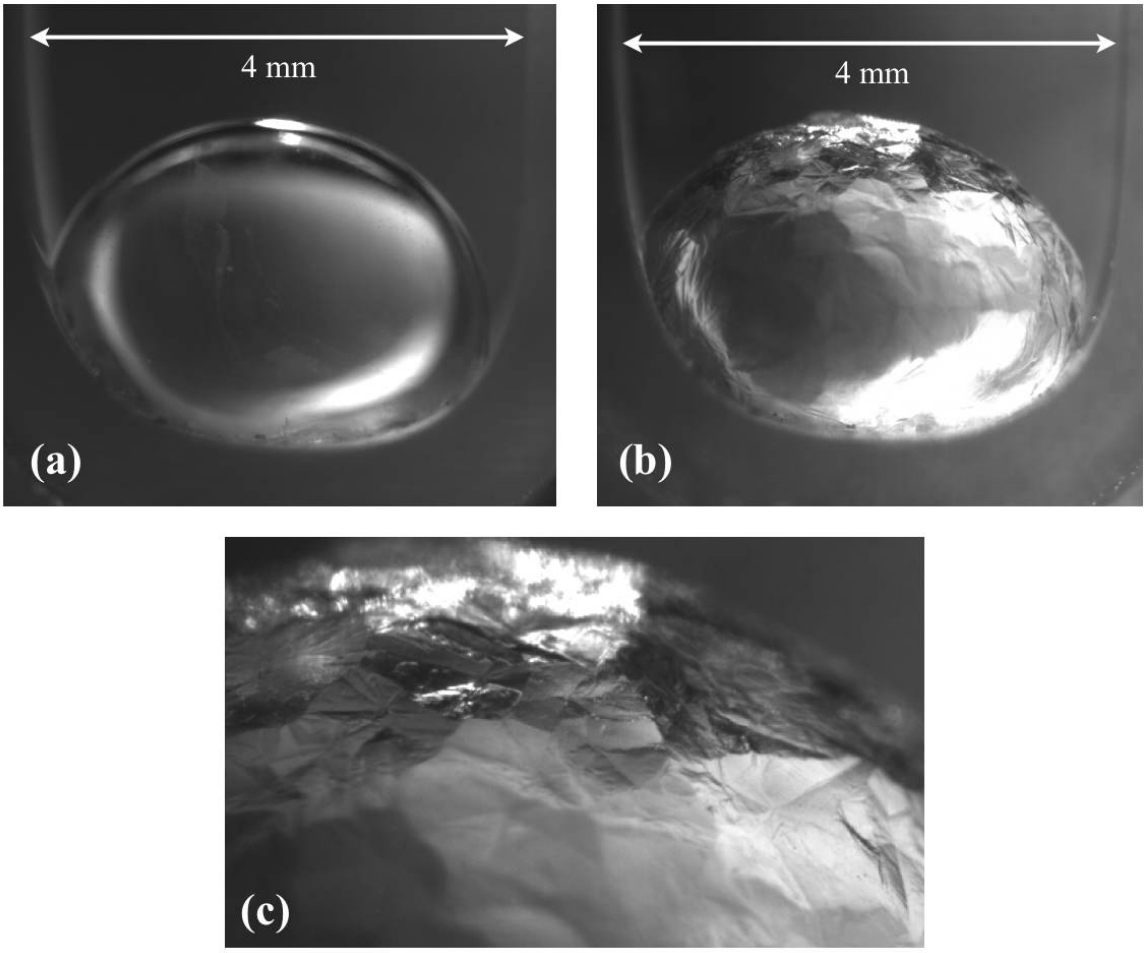

Figure 3.3: Faceted cyclopentane hydrate shell morphology: oil phase is pure cyclopentane with no surfactant, $T = 0.2^{o}$C (a) initial water drop, (b) hydrate ball, (c) enlarged view of the hydrate ball.

cyclopentane diffuses through the hydrate shell converting unreacted liquid water into hydrate. A criterion of drop darkening due to light scattering was used to detect further hydrate formation. It is important to note that the final hydrate ball diameter is not significantly different as compared to the initial water drop size, see Figure 1 from Taylor et al. [68]. These experiments were performed without any surfactant in the system. Taylor et al. also performed cyclopentane hydrate film thickness measurements at a planar water-cyclopentane interface and reported that the cyclopentane hydrate film thickness began at $\approx$ 12 μm and grew to a final thickness ($\approx$ 15-40 μm) which increased with sub-cooling. Sakemoto et al. [39] also observed similar faceted shell formation at the water-cylopentane interface and reported that sub-cooling primarily governs the facet size.

The process of cyclopentane hydrate growth at the water-oil interface can be divided into three main steps – namely nucleation, lateral surface growth and radial growth, as hypothesized in the calorimetric analysis. For the surfactant free case, lateral surface growth exhibits facet-like hydrate crystals which lead to formation of a hydrate shell around the water drop with unreacted water trapped inside. The faceted crystal structure apparently has junctions sufficiently robust that mass transfer (guest cyclopentane diffusing through the solid, based on work of Jakobsen et al. [34] studying CCl_3F hydrate) limits the water conversion to a very low rate. Figure 3.4 shows additional images of the faceted hydrate shell observed during the lateral surface growth.

3.3.2 Effect of oil-soluble surfactant

The effect of Span 80 on the ultimate cyclopentane hydrate morphology, after what is believed to be full water conversion, is shown in Figure 3.5. The Span

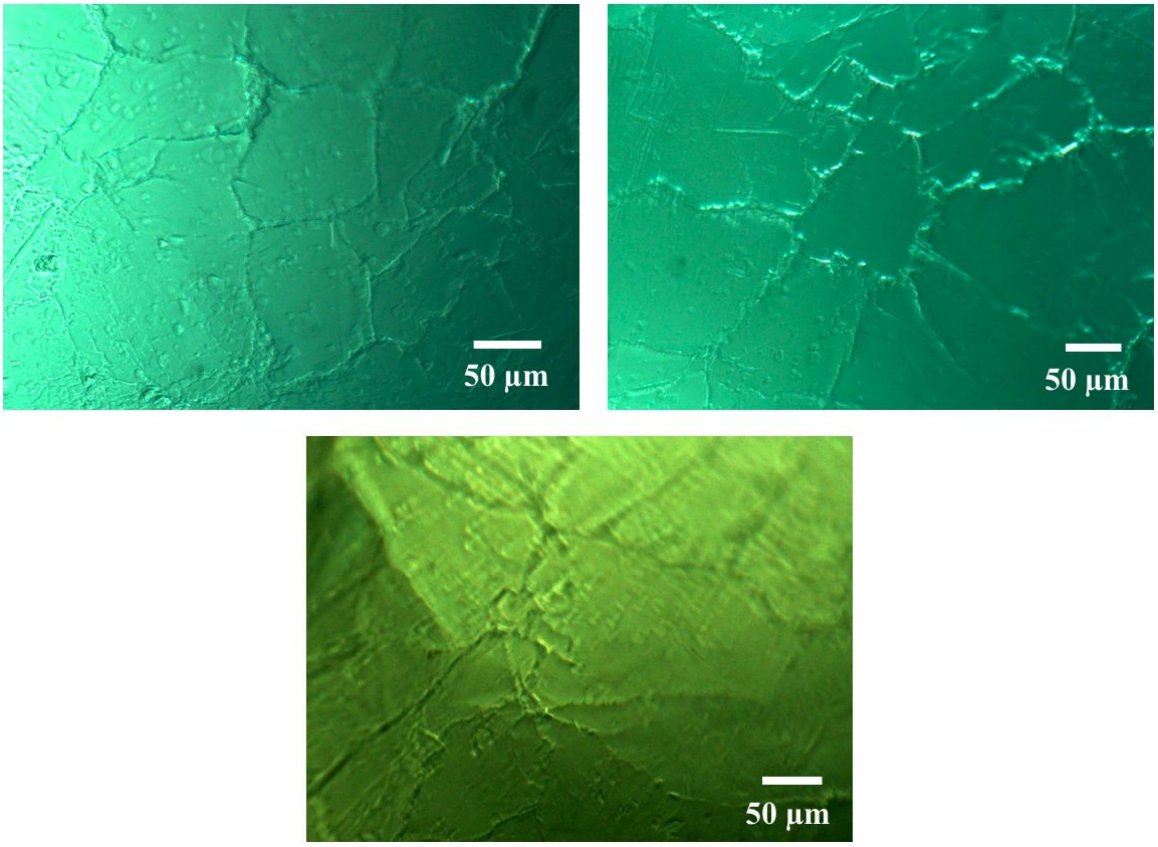

Figure 3.4: Faceted cyclopentane hydrate shell during the lateral surface growth at the water-cyclopentane interface in the absence of surfactant, $T = 0.2^{o}$C.

80 concentration, C_{S80}, is fixed at 0.1% (v/v) based on the cyclopentane volume. A hairy or mushy hydrate morphology is observed as compared to a faceted shell formation observed in the absence of Span 80. This structure has significant porosity, as evidenced by the final hydrate ball size being ~ 1.3 times the initial water drop diameter, or above two times the initial water volume; the difference in density of hydrate and water can account for only a few percent increase.

The process leading to the formation of a hairy and porous morphology in cyclopentane hydrate with sufficient surfactant present also involves a three-step process of nucleation, lateral growth, and radial growth. The process begins similarly to the surfactant-free case, with nucleation at the water-cyclopentane interface as soon as free liquid water becomes available. The nuclei grow laterally along the water drop surface, but develop a remarkable structure which is of primary interest here. Specifically, the hydrate crystals exhibit a three-dimensional (3D) hollow-conical morphology as opposed to a faceted plate structure. Figure 3.6 shows images of hollow-conical crystals. The hollow-conical crystal has its base, predominantly hexagonal, pinned at the water-cyclopentane interface with the vertex pointing into the water phase. The interior of the cone is filled with cyclopentane during this pinned phase. The pinning becomes unstable as the crystal grows larger, typically with the crystal > 100 μm across the open base of the cone, and water is observed to flow in to replace cyclopentane; the hydrate surface is preferentially wetted by water relative to cyclopentane. As a consequence of water filling the cone, the crystal becomes immersed in the water phase, regenerating the water-cyclopentane interface for further hydrate formation. The sequence of lateral crystal growth in the conical form and crystal merging back into the water phase occurs repeatedly until the water drop volume is packed with hydrate crystals, but retains some liquid water. This liquid water then undergoes outward radial flow and converts to hydrate where it

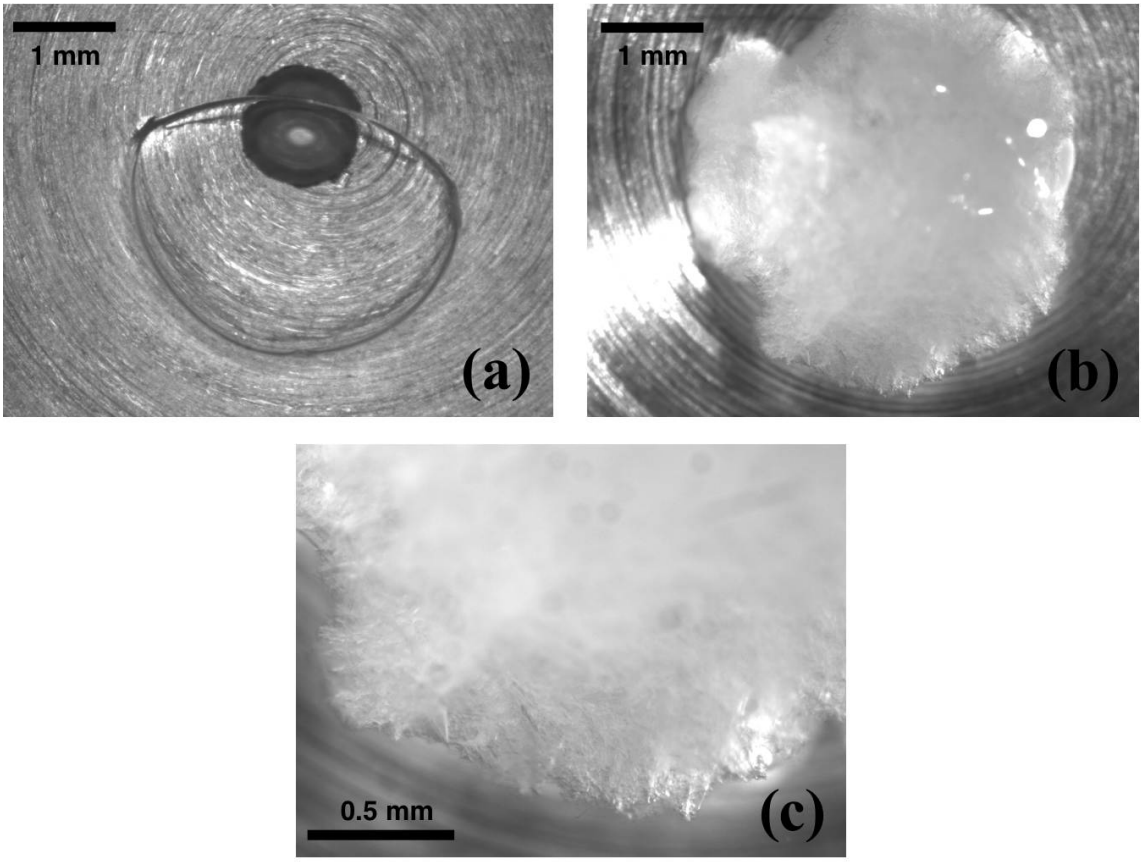

Figure 3.5: Effect of Span 80 on cyclopentane hydrate morphology: water drop in cyclopentane, $C_{S80} = 0.1\%$ (v/v), $T = 0.2^{o}$C. (a) initial water drop, (b) mushy/hairy ball after essentially complete water conversion to cyclopentane hydrate, (c) enlarged view of the hydrate ball.

contacts the cyclopentane. Cyclopentane flows into void space within the crystal packing and thus the observed hairy / porous morphology shown in Figure 3.5 is developed.

In the growth of hydrate crystals, a factor of critical importance is that hydrate formation is an interfacial process. The 'reaction' of water and cyclopentane to form a clathrate structure can only take place at the rates observed at the water-cyclopentane interface, as the two components are simultaneously present at high concentrations in the interfacial region. Any modification in the interfacial properties must be expected

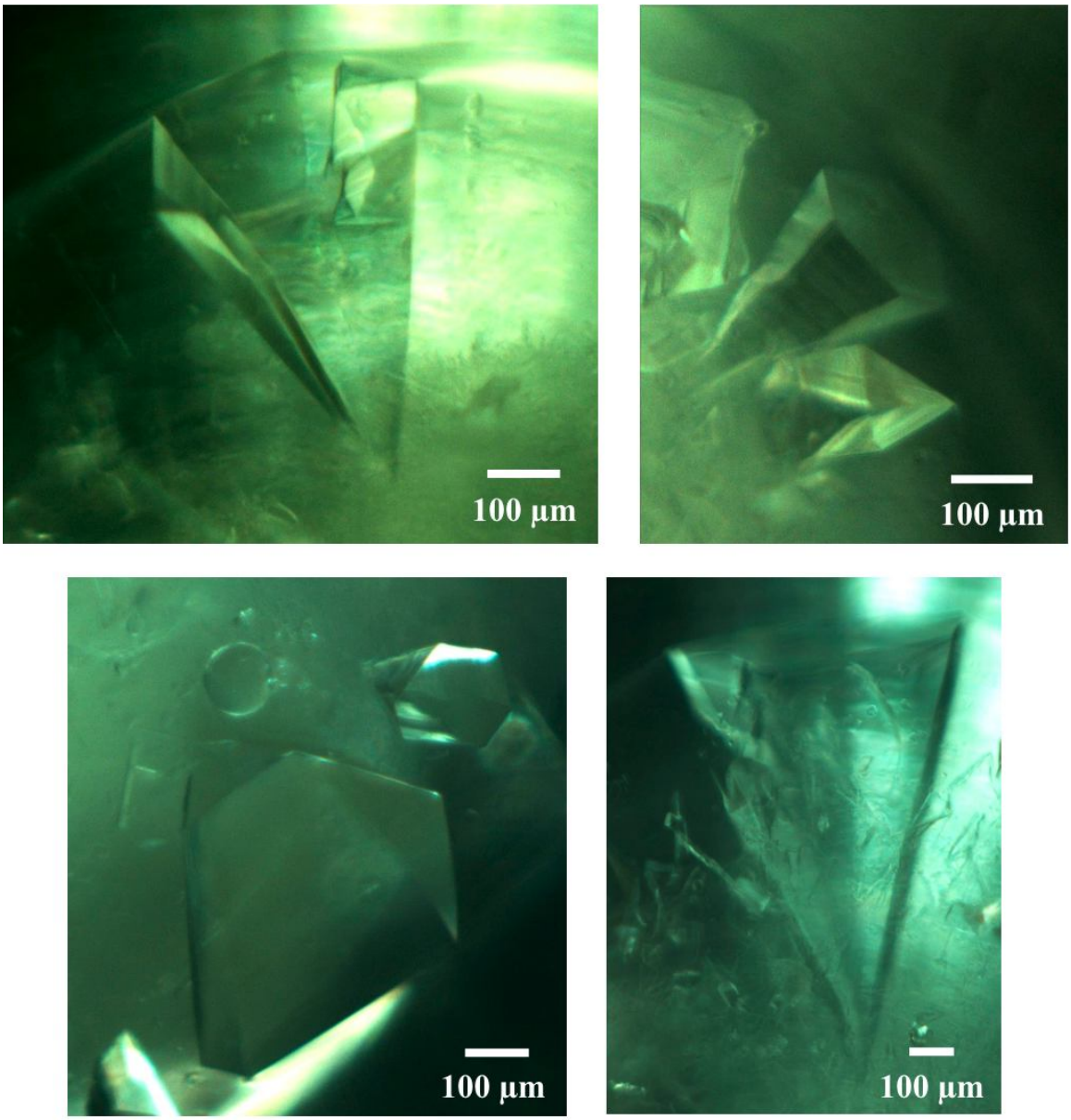

Figure 3.6: Hollow-conical cyclopentane hydrate crystals during the lateral surface growth at the water-cyclopentane interface, $C_{\mathrm{S80}} = 0.1\%$ (v/v), $T = 0.2^{\mathrm{o}}\mathrm{C}$.

to affect the hydrate formation, both in rate and in the mechanistic details of the process. Figure 3.7 shows the equilibrium water-cyclopentane interfacial tension as a function of Span 80 concentration, C_{S80}; all concentrations are on a volume percentage based on the cyclopentane volume. The interfacial tension (measured using a pendant drop method [71]) for a clean water-cyclopentane interface, *i.e.* for $C_{\mathrm{S80}} = 0$, is γ_c = 48.7 mN/m. The data in Figure 3.7 indicate saturation of cyclopentane *i.e.* a constant interfacial tension above a critical micelle concentration (CMC) $C_{\mathrm{S80,CMC}} \approx$ 0.03% (*v/v*). The data below the CMC can be fitted with a Langmuir adsorption isotherm and equation of state [72],

$$\frac{\Gamma_e}{\Gamma_\infty} = \frac{1}{1 + (\alpha/\beta C_o)}, \tag{3.1}$$

$$\gamma(\Gamma) = \gamma_c + RT\Gamma_\infty \left[ln\left(1 - \frac{\Gamma}{\Gamma_\infty}\right)\right], \tag{3.2}$$

where γ is the interfacial tension (as noted γ_c is for the clean water-cyclopentane interface), C_{S80} is the bulk Span 80 concentration, Γ is the surface concentration (subscripts e and ∞ for the equilibrium and maximum packing concentrations, respectively), R is the gas constant, T is absolute temperature, and finally α and β are the kinetic rate constants. The fitting parameters are Γ_∞ and (α/β), with the best fit values for the Span 80 / water / cyclopentane system reported in Table 3.1. The value of Γ_∞ corresponds to 45 Å^2 of area per adsorbed Span 80 molecule. This value is in close agreement with reported values for the same surfactant at the water-paraffin interface [73, 74].

The concentration of C_{S80} = 0.1% (*v/v*) is used for the cases shown in Figure 3.5. This is above the CMC value of $C_{\mathrm{S80,CMC}} \approx$ 0.03% (*v/v*) and thus the surface concentration at the water-cyclopentane interface will be at its maximum,

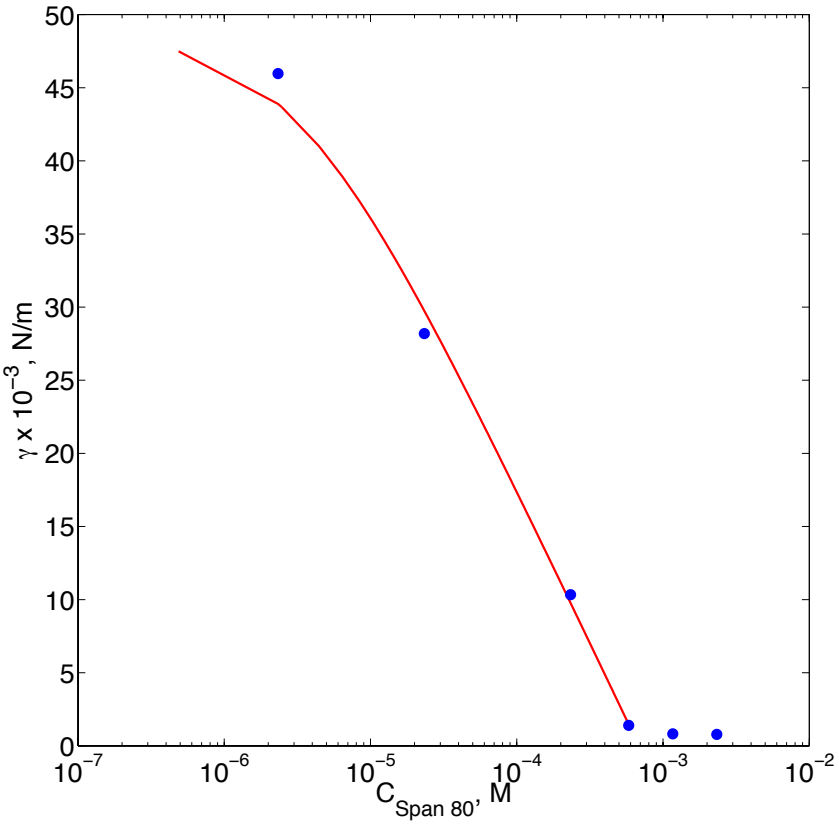

Figure 3.7: The equilibrium interfacial tension of water-cyclopentane with variable Span 80 concentration in cyclopentane, line: Langmuir fit.

CMC in cyclopentane (% v/v)	0.03
γ_{CMC} (mN/m)	0.80
Γ_∞ ($\times 10^{-6}$ mol/m^2)	3.69
α/β ($\times 10^{-3}$ mol/m^2)	3.45

Table 3.1: Langmuir adsorption isotherm parameters for Span 80 at water-cyclopentane interface.

Γ_∞. Hydrate nucleation and lateral crystal growth cause reduction in the available interfacial area for the same number of Span 80 molecules, unless desorption of the surfactant is very rapid. Our conjecture is that hydrate crystal growth laterally across the interface leads to crowding of Span 80 molecules in the remaining area, thus developing an excess surface pressure (*i.e.* Γ exceeds the maximum equilibrium surface concentration Γ_∞). Figure 3.8 shows a pictorial explanation of the argument. In this scenario, the excess surface pressure acts as a mechanical barrier to lateral crystal growth and forces the crystal to grow conically into the water phase. Figure 3.9 shows the evolution of a conical crystal at the water drop-cyclopentane interface. The growth of conical crystal can only take place at the cone base *i.e.* at the three phase contact of water-hydrate-cyclopentane. After the crystal grows sufficiently large, typically to $O(100)$ μm in size, the pinning loses stability and water fills the cone. This causes the hydrate crystal to become immersed in the water, thus regenerating the interface for further hydrate formation. The water front during filling of the cone is marked with a white dotted line and solid lines indicate the position of the cone in Figure 3.9.

A similar morphological characterization is carried out at a planar water-cyclopentane interface with 0.1% (v/v) Span 80 to validate the hypothesis presented in Figure 3.8. In this case, the interface is seeded with an externally-grown cyclopentane hydrate crystal. Similar to the crystals observed at the water drop-cyclopentane interface, hydrate crystals grown at the planar interface also showed hollow-conical crystal morphology; see Figure 3.10.

The argument of excess surface pressure ($\Gamma > \Gamma_\infty$) driving the conical crystal growth requires for its validity that the desorption rate of Span 80 is less than the hydrate crystal growth rate. In other words, if the Span 80 molecules desorb very rapidly from the interface, allowing equilibration of the surface concentration Γ for the

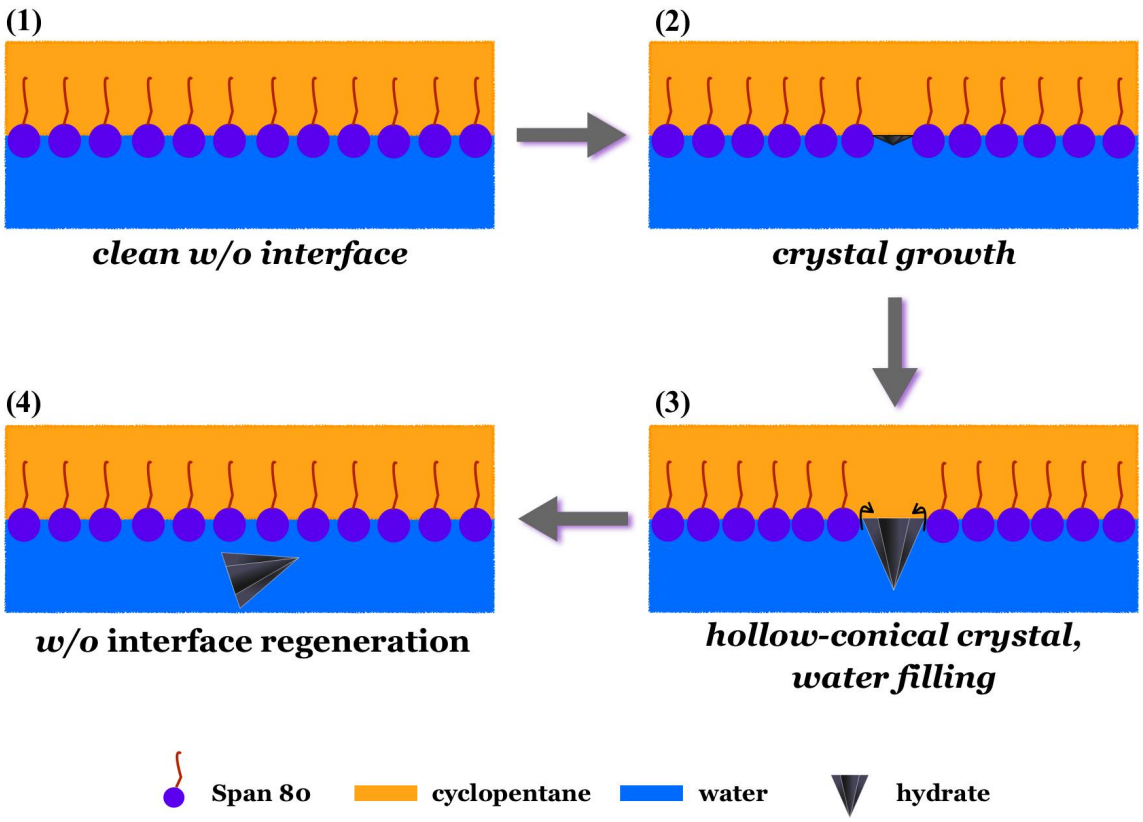

Figure 3.8: Schematic of the proposed cyclopentane hydrate lateral surface growth hypothesis: water-cyclopentane interfacial area is reduced by the crystal growth and the surfactant crowding in the remaining area (excessive surface pressure) leads to conical crystal shape. Interface is regenerated by pushing the crystal into the bulk water phase.

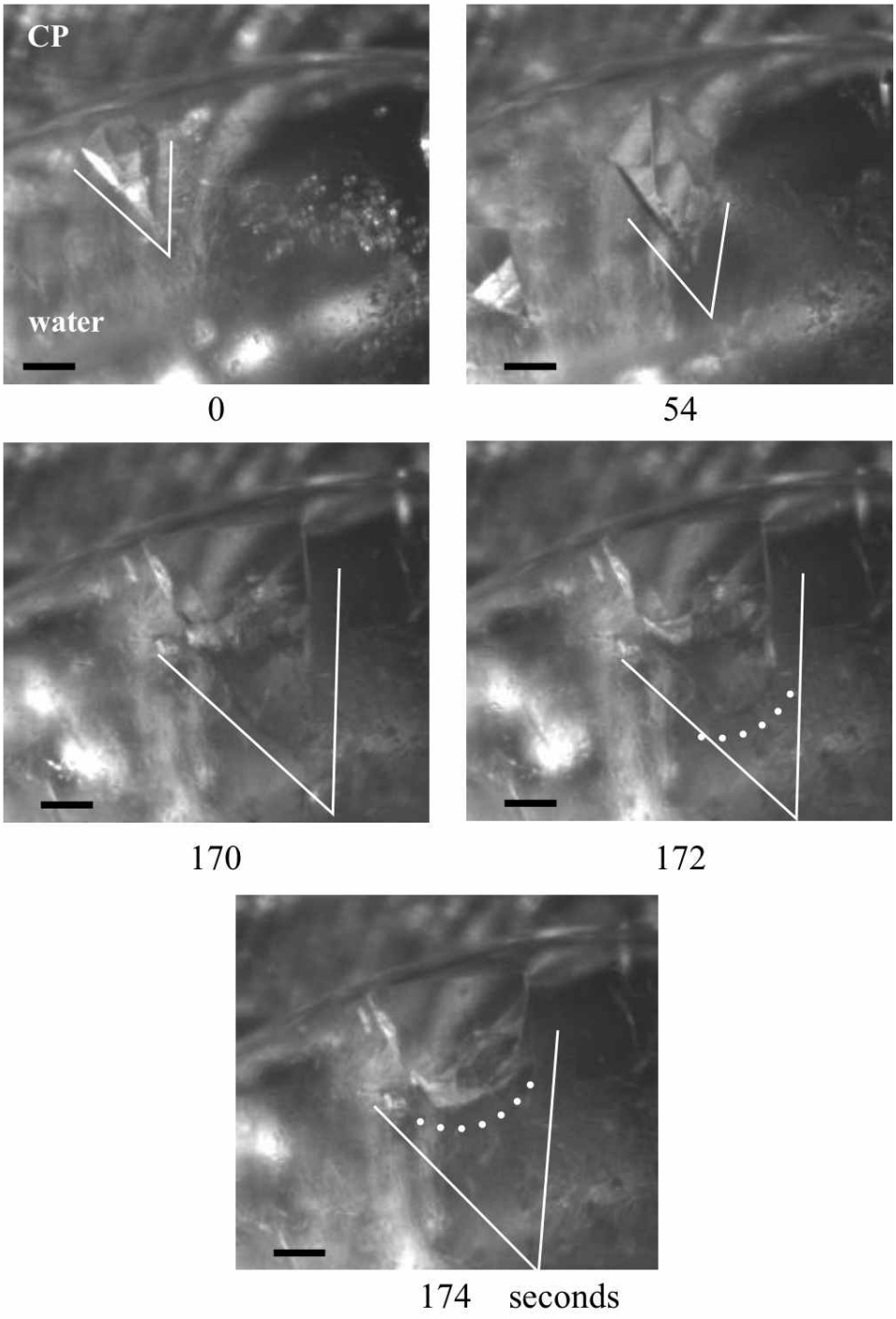

Figure 3.9: Lateral surface hydrate growth: hollow-conical crystals at curved water-cyclopentane interface (enlarged section of a 4 μl water drop), $C_{S80} = 0.1\%$ (v/v), $T = 0.2^{o}$C, scale bar = 0.1 mm (solid lines show the vertex of the conical crystal and dotted white line shows the water front filling the cone).

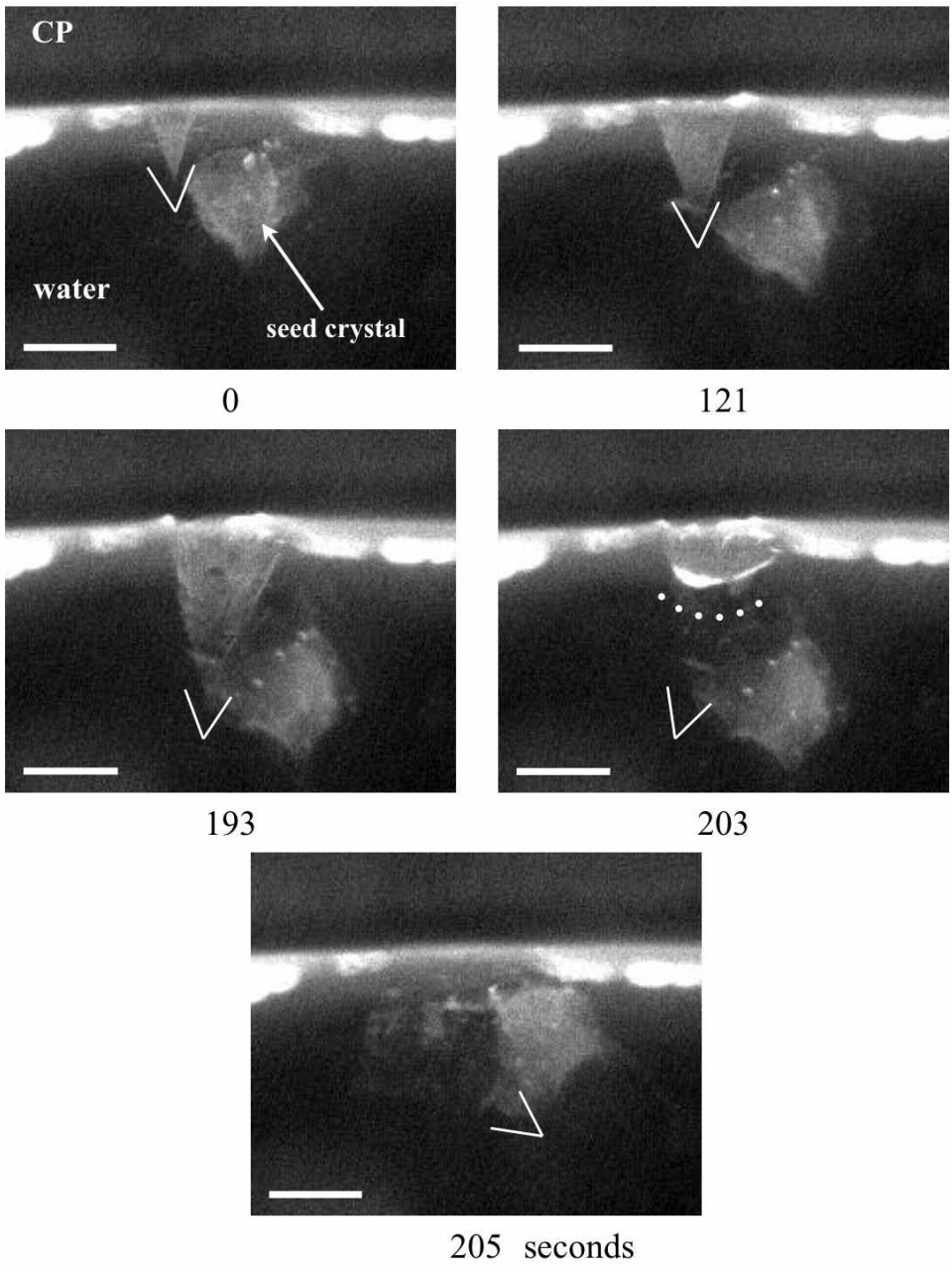

Figure 3.10: Lateral surface hydrate growth: hollow-conical crystals at a planar water-cyclopentane interface, $C_{S80} = 0.1\%$ (v/v), $T = 0.2^{o}$C, scale bar = 0.1 mm (solid lines show the vertex of the conical crystal and dotted white line shows the water front filling the cone).

new reduced area, no excess surface pressure will be generated due to crystal growth at the interface. To validate our argument, a similar single-drop morphology experiment is performed at a higher hold temperature (and thus reduced sub-cooling), $T_{\text{hold}} = 4$ °C, with the same Span 80 concentration of $C_{S80} = 0.1\%$ (v/v) in cyclopentane. Reduction of the sub-cooling by 3.8°C (over half the sub-cooling relative to the equilibrium dissociation temperature of $T_{\text{eqm}} \approx 7$ °C) should slow the hydrate crystal growth rate; we assume that Span 80 desorption rate is not significantly affected by this temperature change. Note the reduction in sub-cooling does not have major effect on hydrate nucleation as our protocol uses ice melting to overcome the induction time. At lower sub-cooling (higher temperature), crystal growth is much slower (note the times in Figure 3.11) and most of the crystals are plate-like (see Figure 3.13 for detailed view), in contrast to conical crystals obtained at higher sub-cooling. The slow lateral hydrate growth, and associated slower reduction in the interfacial area, is believed to provide sufficient time for Span 80 desorption from the interface to mitigate the interfacial crowding. The observation of plate-like crystals is consistent with our argument that rapid hydrate growth leads to excess surface pressure due to the crowding of surfactant is responsible for the observed conical crystal growth. Figure 3.11 compares the hydrate morphologies at 0.2°C and 4°C. The time required for the hydrate growth increased by an order of magnitude due to drop in sub-cooling. Though the crystals at reduced sub-cooling are predominantly plate-like rather than conical, water wetting of the hydrate causes the crystals to eventually be immersed into the water drop and leads to the hairy / porous hydrate growth qualitatively similar to the morphology at the higher sub-cooling level, although differing in detail, as shown in an enlarged view in Figure 3.11.

A similar morphological characterization at 0.2°C for different Span 80 concentrations is shown in Figure 3.12. The water drop volume is 4 μl in each case. A

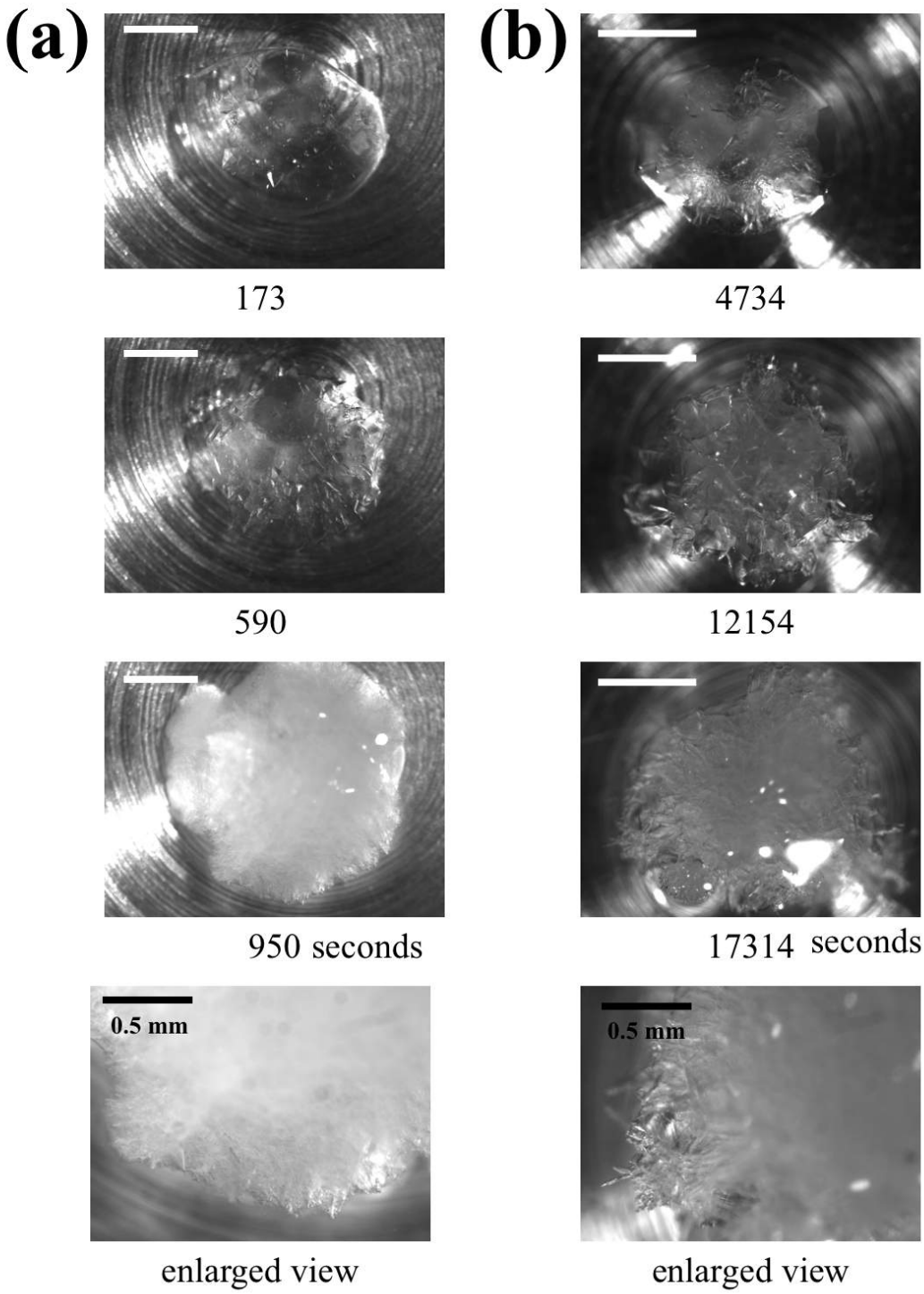

Figure 3.11: Cyclopentane hydrate morphologies in cyclopentane, $C_{S80} = 0.1\%$ (v/v), 4μl water drop, (a) 0.2°C, (b) 4°C. Time is measured from onset of ice melting.

faceted hydrate shell morphology, similar to the surfactant free case, is observed for the low concentration of $C_{S80} = 0.0001\%$ (v/v). Note that for this concentration of Span 80, the interfacial tension is only reduced to $\gamma = 46$ mN/m from $\gamma_c = 48.7$ mN/m. For $C_{S80} = 0.001\%$ (v/v), interfacial tension is $\gamma = 28$ mN/m and the observed hydrate morphology is shown in Figure 3.12(b). For this case, it is observed that a complete hydrate shell develops around the water drop immediately after ice melting and the shell eventually buckles with the bulk water exiting the shell in what appears visually almost like boiling, leading to further hydrate formation in lumpy (but notably not hairy) morphology. The absence of conical crystals for these low Span 80 concentrations suggests that the lower Γ values at these concentrations are not enough to generate the excess surface pressure assumed to be responsible for the conical crystal growth. The system with $C_{S80} = 0.01\%$ (v/v) Span 80 follows a very similar pattern as the 0.1% case, where the nucleation is followed by lateral surface growth in the conical form, as seen in Figure 3.13. The conical hydrate crystals become immersed in and eventually pack the water phase, with subsequent radial hydrate growth leading to the hairy / porous morphology. At these higher Span 80 concentrations — approximately $C_{S80} > 0.01\%$ (v/v) — Γ values approach Γ_∞ and are enough to generate the excess surface pressure during the lateral crystal growth to force the conical crystal formation.

The immersion of hydrate crystals, either conical or plate-like, into the water phase can be explained by wettability arguments. The wettability of a solid depends on the contact angle θ of a liquid drop at the solid surface. In case of water-hydrate-oil system (refer Figure 3.14), $\theta < 90$ suggests water-wet hydrate and $\theta > 90$ represents oil-wet hydrate surface. Young's equation represents the balance of interfacial tensions at

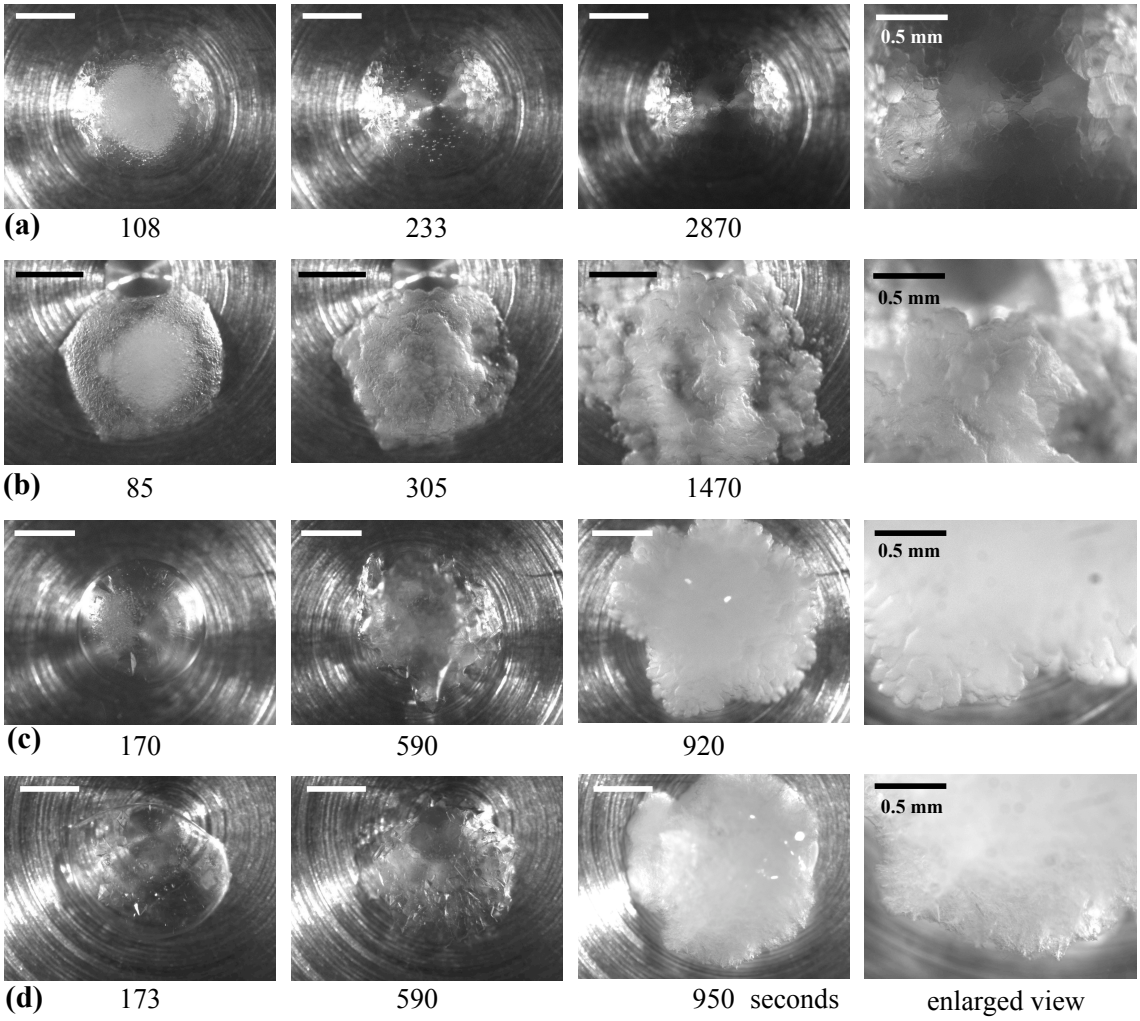

Figure 3.12: Cyclopentane hydrate crystal morphologies at various C_{S80} (v/v) - (a) 0.0001%, (b) 0.001%, (c) 0.01%, (d) 0.1%. Water drop volume = 4 μl, T= 0.2°C, numbers indicate the elapsed time in seconds from the start of ice melting, scale bar = 1 mm unless otherwise noted.

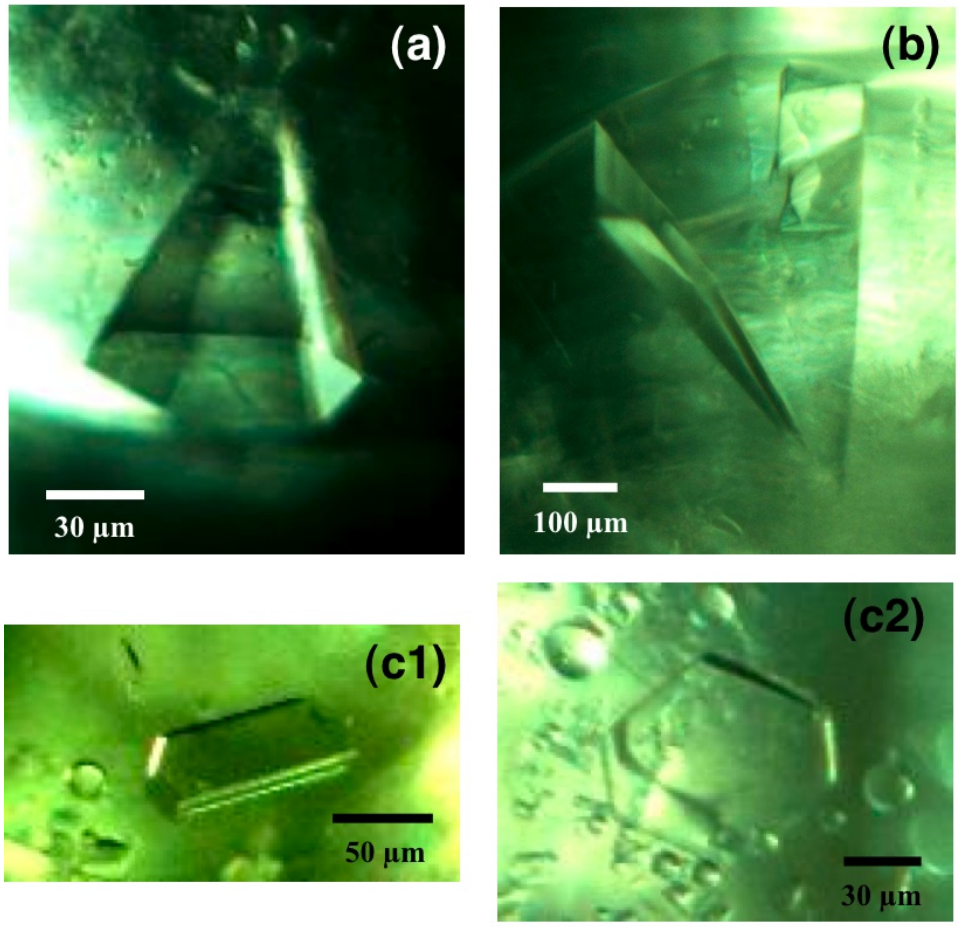

Figure 3.13: Cyclopentane hydrate crystal morphologies (a) hollow-conical at C_{S80} = 0.01%, T = 0.2°C, (b) hollow-conical at C_{S80} = 0.1%, T = 0.2°C, (c) plate-like at C_{S80} = 0.1%, T = 4°C. All percentages are *v/v* based on cyclopentane.

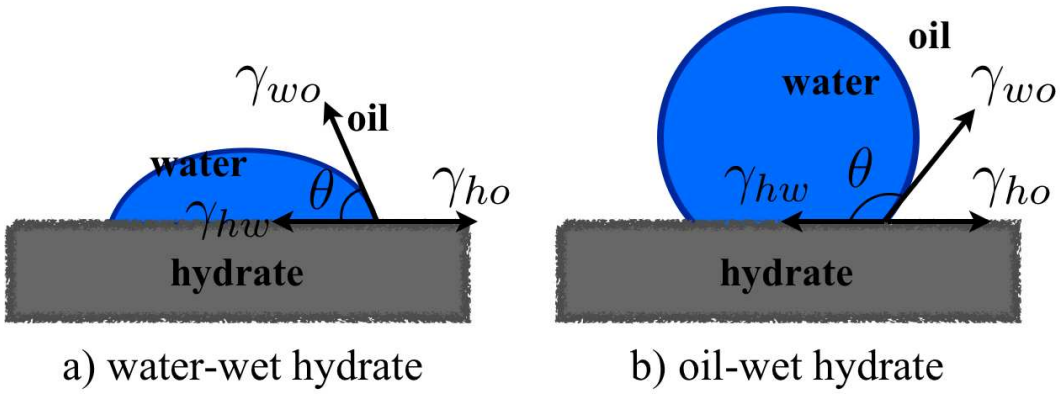

Figure 3.14: Interfacial tension balance at the hydrate-water-oil (h-w-o) interface, γ is interfacial tension and θ is the contact angle of water on the hydrate surface.

the 3-phase contact point,

$$\gamma_{ho} = \gamma_{hw} + \gamma_{wo} \times \cos\theta, \tag{3.3}$$

where θ is the contact angle of water on the hydrate surface and γ is the interfacial tension with subscripts w, h, o representing water, hydrate, oil phases respectively. Wettability can also be represented in terms of a spreading coefficient,

$$S_{h-w} = \gamma_{ho} - \gamma_{wo} - \gamma_{hw}. \tag{3.4}$$

When $S_{h-w} > 0$, spontaneous spreading of a water drop occurs on the hydrate surface. The addition of surfactant that reduces γ_{wo} and γ_{hw} can make the hydrate more water-wet. Recall that, 0.1% Span 80 concentration leads to a very low water-cyclopentane interfacial tension, $\gamma_{wo} \sim 1$ mN/m. In case of spherical particles at the water-oil interface [75], wettability (contact angle) replaces the HLB criterion used to quantify the water or oil-liking tendency of surfactants. A schematic illustration of spherical particles at the water-oil interface is shown in Figure 3.15. Though the

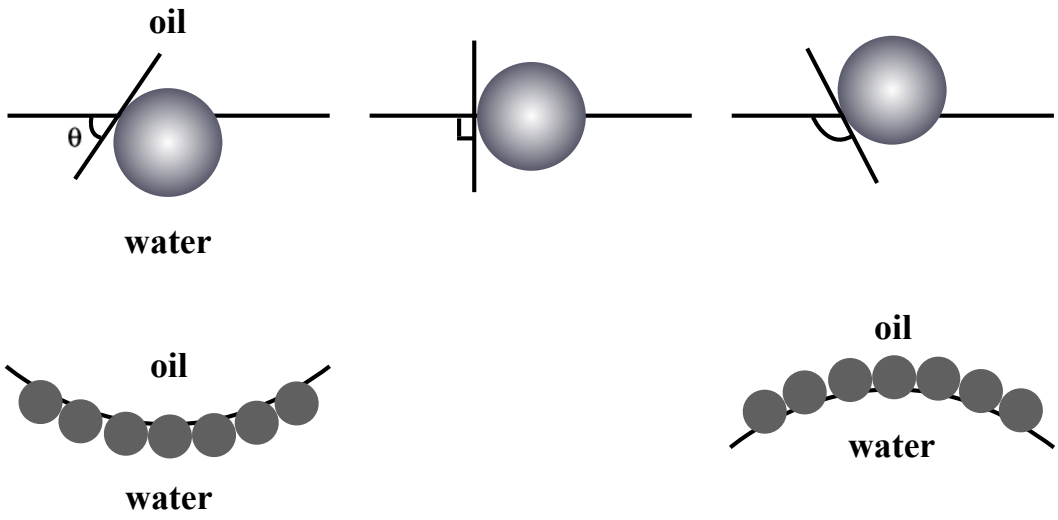

Figure 3.15: Position of spherical particle at the planar water-oil interface for a contact angle θ less than 90^o (left), equal to 90^o (center) and greater than 90^o (right). Lower images show to the probable position of particles at a curves interface for the corresponding contact angle, adapted from Binks (2002).

hydrate crystal shape is not spherical, wettability arguments should remain the same. Thus the hydrophilic conical hydrate crystal gets preferentially wetted by water and merges back into the water phase as soon as water wets the cone interior.

The merging of hydrate crystals into the water continue until the drop volume is completely filled with crystals. Then the unreacted liquid water flows outwards leading to radial hydrate growth. The radial outward flow of water is along the hydrate crystals as a significant reduction in γ_{wo} causes spontaneous spreading of water on hydrate crystals. Figure 3.16 shows a sequence of images during the radial growth for a water drop in cyclopentane with $C_{\mathrm{S80}} = 0.1\%$. A curved water interface, marked with an arrow (at 541 seconds), slowly diminishes as the water rises along the hydrate crystals and further growth occurs. It can be seen that the right corner of the images develop into a hairy morphology as the unreacted bulk water keeps flowing along the hydrate crystals and reacts with readily available external cyclopentane.

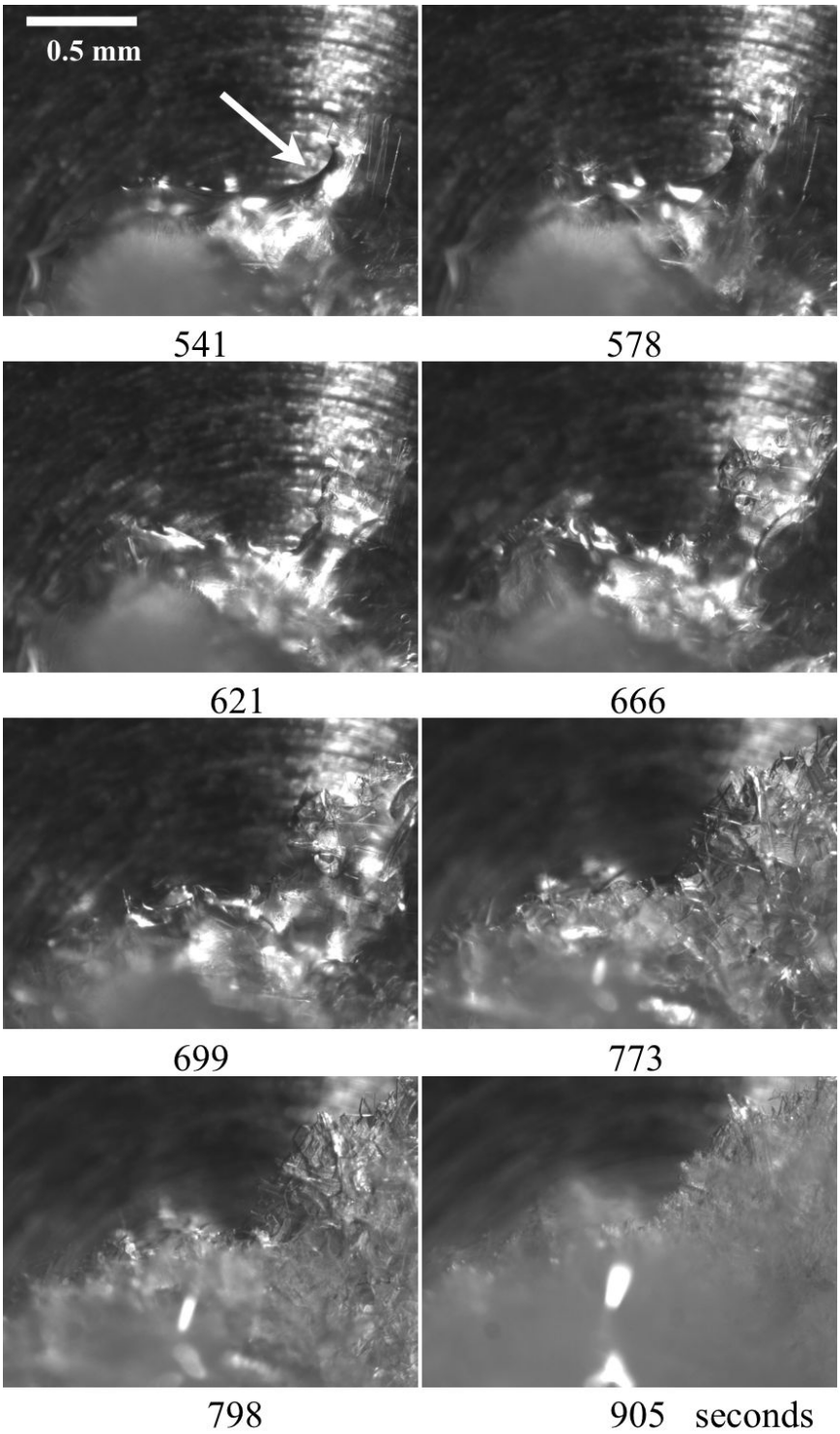

Figure 3.16: Radial growth of cyclopentane hydrates, water drop in cyclopentane, C_{S80} = 0.1% (*v*/*v*), T = 0.2°C, white arrow shows a curved water-cyclopentane interface which diminishes with further hydrate growth.

To study the effect of other surfactants on the cyclopentane hydrate morphology, Span 80 is replaced with a less surface-active surfactant ethylene glycol monohexadecyl ether (refered as $C_{16}E_1$) surfactant. $C_{16}E_1$ has the same carbon number hydrophobic tail but a much smaller head group as compared to Span 80. See Figure 3.17(a) for the molecular structures. Figure 3.17(b) compares the cyclopentane hydrate morphologies in the presence of $C_{16}E_1$ and Span 80 for the same molar concentration of 2.33 mM, *i.e.* $C_{S80} = 0.1\%$ (v/v). The hydrate morphology is a fish scales type shell formation around the water drop as compared to hairy morphology observed in the presence of Span 80.

For the 2.33 mM molar concentration of $C_{16}E_1$, cyclopentane-water interfacial tension is 44.5 mN/m. This clearly indicates that $C_{16}E_1$ is much less surface active as compared to Span 80. In another experiment performed with about ten times more $C_{16}E_1$ concentration (21mM), similar faceted hydrate shell morphology is observed. The interfacial tension value obtained for this concentration was 34.6 mN/m, again not nearly as low as obtained for lower Span 80 loadings. The surfactant crowding effect observed to be responsible for the conical crystal behavior is apparently absent in case of $C_{16}E_1$ for the concentrations studied here.

3.3.3 Effect of cyclopentane fraction

The cyclopentane hydrate equilibrium temperature is found to decrease with a drop in cyclopentane fraction in the external oil phase, see Figure 3.18. A light mineral oil is used as a second oil component to adjust the concentration of cyclopentane. The hydrate equilibrium point is obtained from the onset of an endothermic hydrate dissociation peak (μDSC) during a slow heating (0.25°C/min) of hydrates from -5°C to 15°C. The PVTsim calculations are performed using the Peng-Robinson equation

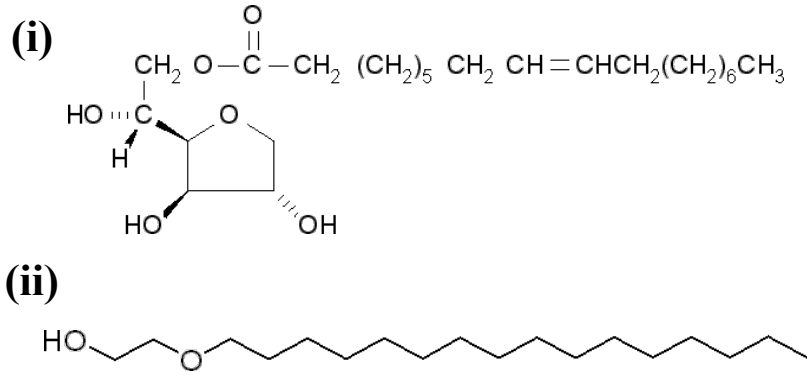

(a) Surfactant molecular structures

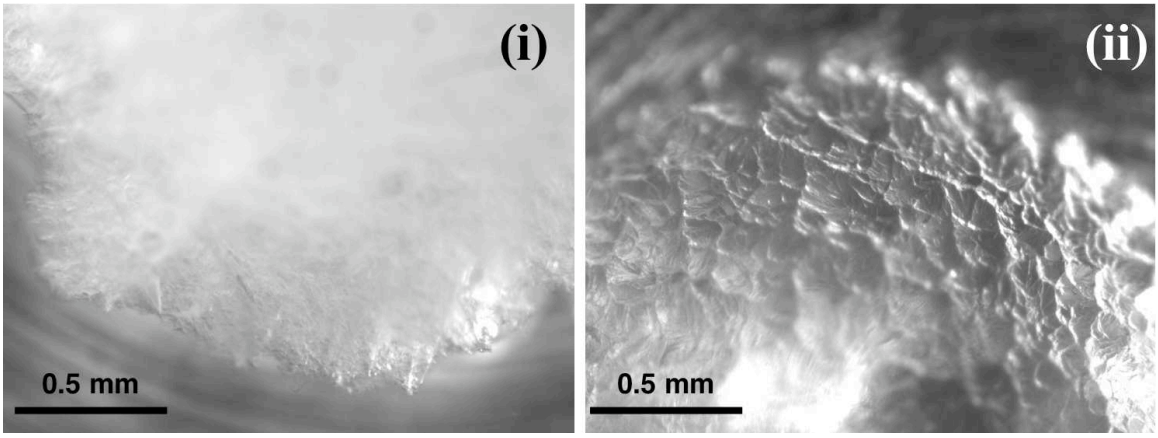

(b) Hydrate morphologies

Figure 3.17: The effect of oil-soluble surfactants on cyclopentane hydrate morphologies, oil phase is cyclopentane, (i) sorbitan monooleate - Span 80, (ii) ethylene glycol monohexadecyl ether - $C_{16}E_1$, concentration = 2.33 mM, $T = 0.2^oC$

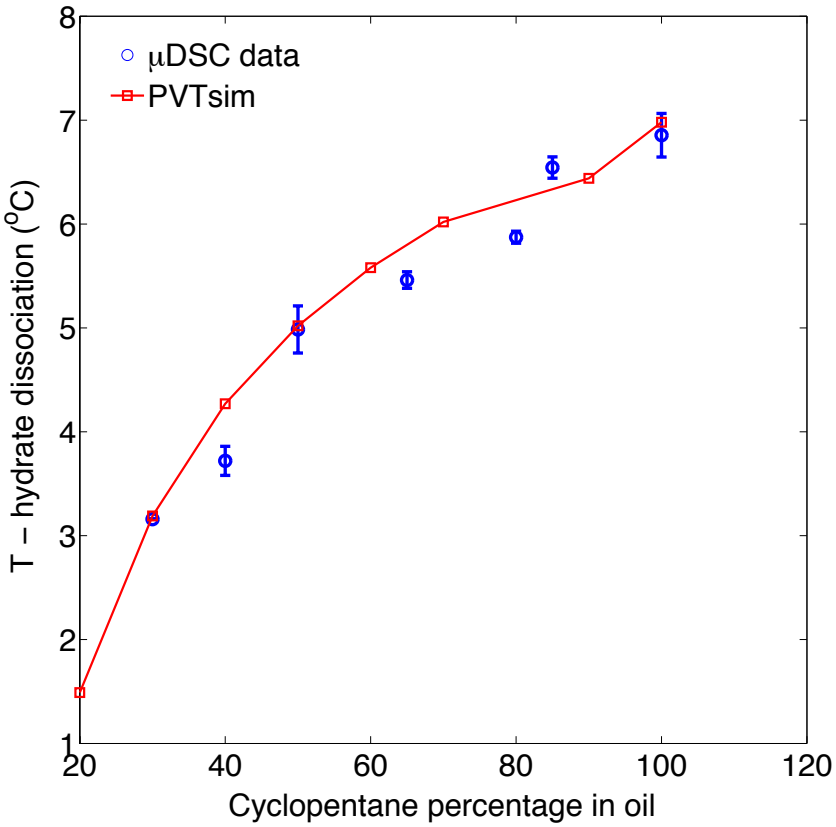

Figure 3.18: Effect of cyclopentane concentration on the cyclopentane hydrate equilibrium temperature, circles: experiments, squares: PVTsim calculations.

of state where n-decane is used as the second oil component due to unavailability of mineral oil composition. A reasonable agreement between experimental and calculated values is observed.

Figure 3.19 shows the cyclopentane hydrate morphologies for three different cyclopentane concentrations of 100%, 65% and 50% by volume, along with the times required for a complete shell formation given in the caption. The hydrate shell is found to have smaller facets as the cyclopentane concentration decreases. The lower equilibrium temperature with a drop in cyclopentane concentration also leads to a drop in the driving force or sub-cooling for the hydrate growth at a fixed temperature and thus the time required for a complete shell formation increases, as seen in Figure

3.19. The hydrate growth sequence for the same three oil compositions at C_{S80} = 0.1% (v/v) is shown in Figure 3.20. The presence of Span 80 leads to similar conical crystal behavior, as observed in case of 100% cyclopentane, for oil mixtures containing 65% and 50% cyclopentane as well. The process of conical crystal growth and crystals merging back into the water phase followed by a radial outward flow of water leads to the hairy morphology in each case. The time required for complete growth is also found to increase with the drop in cyclopentane concentration due to reduced sub-cooling.

3.3.4 Effect of Anti-agglomerant

A commercial water-soluble AA, a confidential quaternary ammonium salt solution in ethylene glycol and iso-propyl alcohol, is obtained from project sponsors. Figure 3.21 demonstrates the effect of AA on the cyclopentane hydrate morphology. The presence of AA in the water drop completely eliminates the interfacial effects of Span 80, the conical crystal behavior and immersion of crystals into the water phase, on the crystal morphology. A polycrystalline hydrate shell is observed in the presence of AA even at C_{S80} = 0.1% (v/v).

Hydrate ball - water drop interaction

The hairy cyclopentane hydrate surface is highly hydrophilic and is rapidly wetted by a pure water drop. In another set of experiments where hydrate nucleation is triggered by seeding with an externally prepared cyclopentane hydrate crystal instead of ice melting, it is observed that the seed hydrate crystal immediately gets engulfed by the water drop. The hydrate growth behavior of conical crystal growth, crystals merging back into the water and then the radial growth developing into the hairy

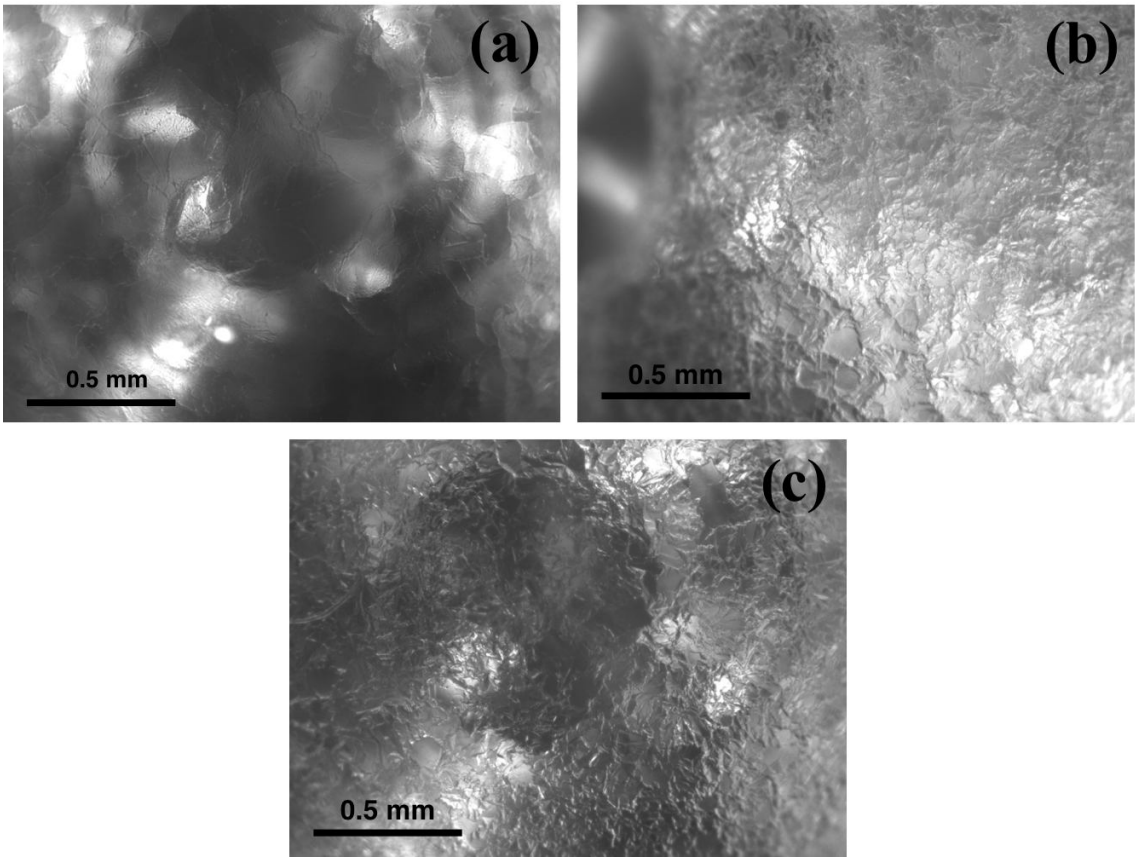

Figure 3.19: Cyclopentane hydrate morphologies at different cyclopentane concentration in the oil phase, no surfactant, $T = 0.2^{o}$, (a) 100% (75 seconds), (b) 65% (135 seconds), (c) 50% (435 seconds) cyclopentane by volume (light mineral oil is used as a second oil component), numbers the time in seconds from the onset of ice melting to a complete shell formation around the water drop.

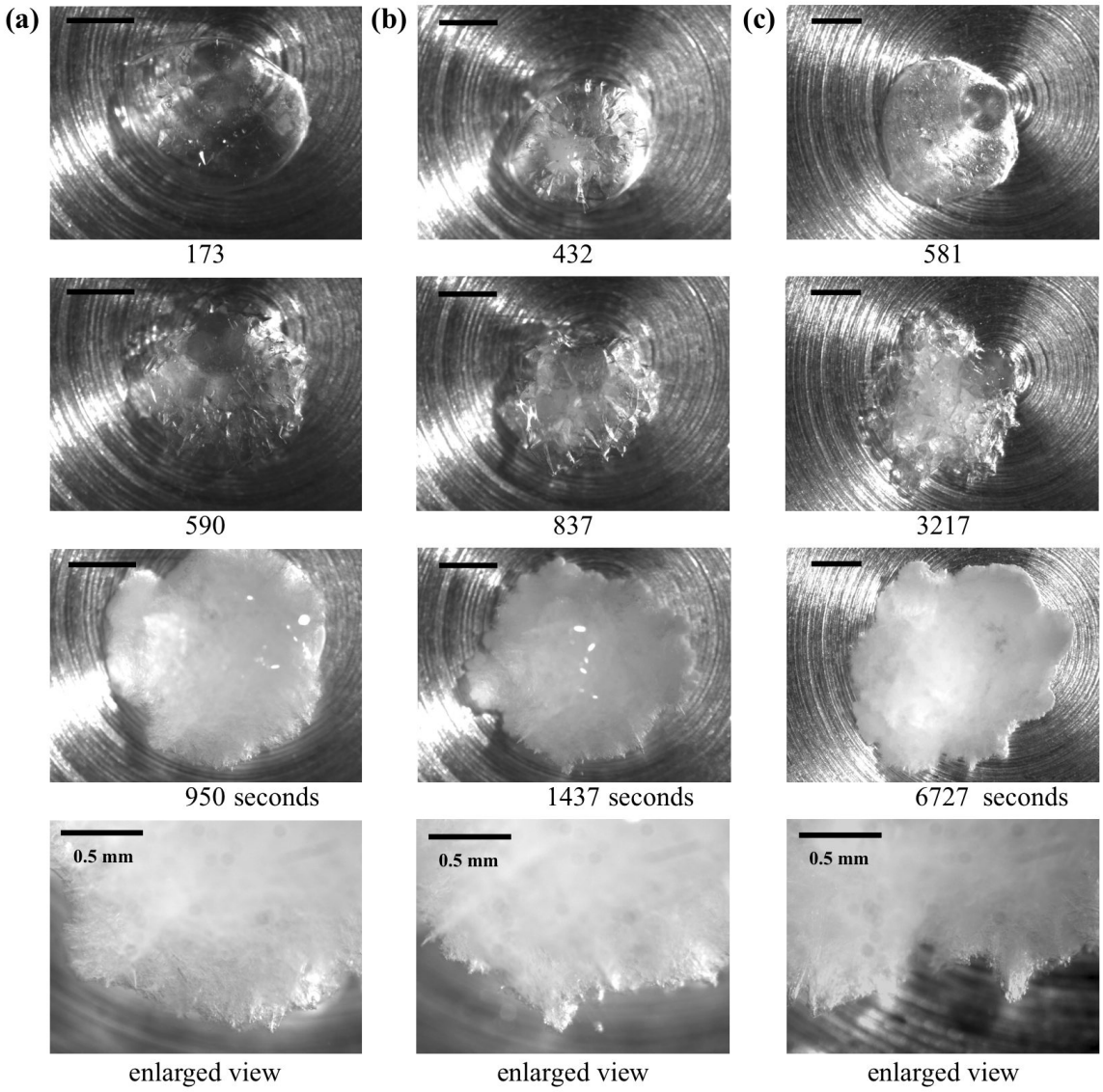

Figure 3.20: Cyclopentane hydrate morphologies at different cyclopentane concentration in the oil phase, $C_{S80} = 0.1\%$ (v/v), $T = 0.2^{o}$, (a) 100%, (b) 65%, (c) 50% cyclopentane by volume (light mineral oil is used as a second oil component), numbers indicate the elapsed time in seconds from the onset of ice melting.

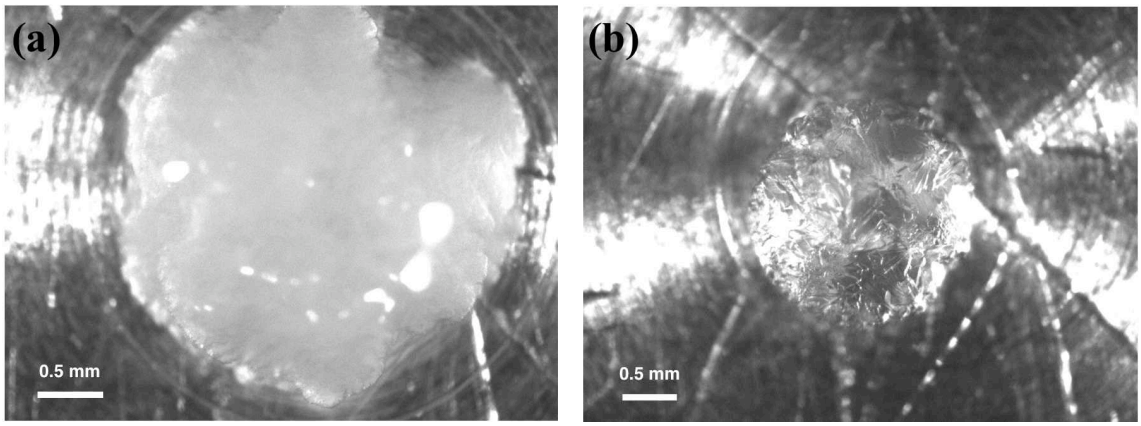

Figure 3.21: Effect of AA on cyclopentane hydrate morphology, oil phase: cyclopentane, $C_{S80} = 0.1\%$ (v/v), $T = 0.2^{o}$ (a) 4μl pure water drop, (b) 4μl water drop with 1% by wt AA.

morphology is found to be independent of the nucleation protocol used. The point to be noted is that the hydrate surface gets preferentially wetted by pure water and thus is hydrophilic in nature. The hydrate shell formed around the water drop containing AA, see Figure 3.21(b), is also found to be hydrophilic in nature as a pure water drop immediately wets the shell. This suggests that cyclopentane hydrate formed in the presence of AA is hydrophilic and the possibility of AA adsorbing onto the hydrate surface is minimal.

However, when a water drop containing AA is contacted with the hairy hydrate surface, it does not wet the hydrate surface and forms a contact angle as shown in Figure 3.22(a). Similar behavior is observed with the hydrate shell obtained from an another water drop containing AA; see Figure 3.22(b). Note that in these experiments Span 80 is always present in the external cyclopentane and thus any water phase without AA will lead to mushy hydrate instead of faceted shell. When hydrate nucleation is triggered by an external seed crystal in case of water drop containing AA as in Figure 3.23, the hydrate seed crystal forms a contact angle and does not

get engulfed into the water drop as observed in the absence of AA. The experimental observations confirm that the presence of AA used in this study makes water less hydrophilic and appears to be the main reason for the hydrate crystals not getting immersed into the water phase even in the presence of Span 80 in cyclopentane. For the experiment shown in Figure 3.23(a), hydrate growth starts at the contact of seed crystal and water drop. The enlarged view of the hydrate growth front can be seen in Figure 3.23(b). It appears that hydrates growing along the water-cyclopentane interface pushes the water drop away from the contact line and finally forms to a "comet-shaped" hydrate shell.

3.3.5 High-pressure propane hydrate morphology

Here we present preliminary results for a high pressure propane hydrate formation at a water drop suspended in light mineral oil. In the absence of surfactant (Span 80) in the oil phase, a faceted and polycrystalline hydrate shell is formed around the water drop; see Figure 3.24(a). Tanaka et al. [55] have reported similar polycrystalline hydrate shell formation around the water drop for methane hydrates. Figure 3.24 shows similarities in the faceted shell morphology of gas hydrates and cyclopentane hydrate.

Figure 3.25 shows the morphology of propane hydrate crystals formed with a water drop immersed in light mineral oil containing Span 80, $C_{\mathrm{S80}} = 0.1\%$ (v/v) based on the oil volume. A hairy hydrate morphology is observed as compared to faceted shell formation observed in the absence of Span 80. The propane hydrate morphology has strong qualitative similarities with the morphological characteristics of cyclopentane hydrate crystals suggesting that the cyclopentane hydrate is a very good atmospheric model for high pressure gas hydrates.

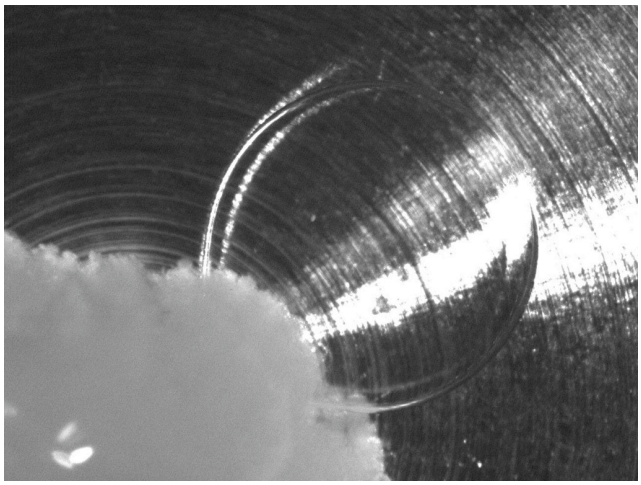

(a) Mushy hydrate ball - AA water drop

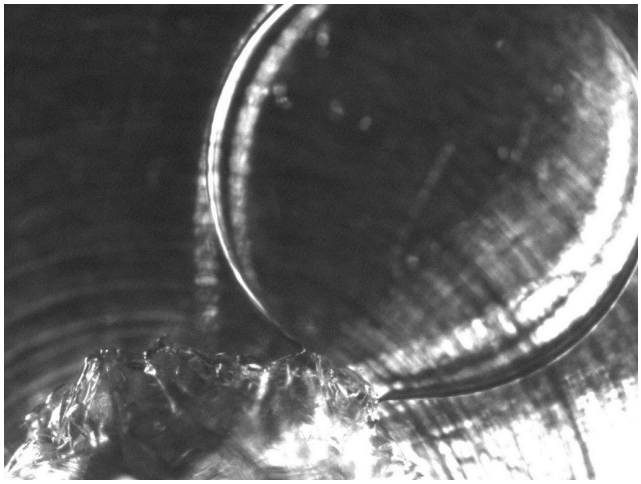

(b) Hydrate shell (obtained from AA water drop) - AA water drop

Figure 3.22: Contact angle of water drop containing 1% AAs on different cyclopentane hydrate surface morphologies, oil phase: cyclopentane, $C_{S80} = 0.1\%$ (v/v), $T = 0.2^{o}$C.

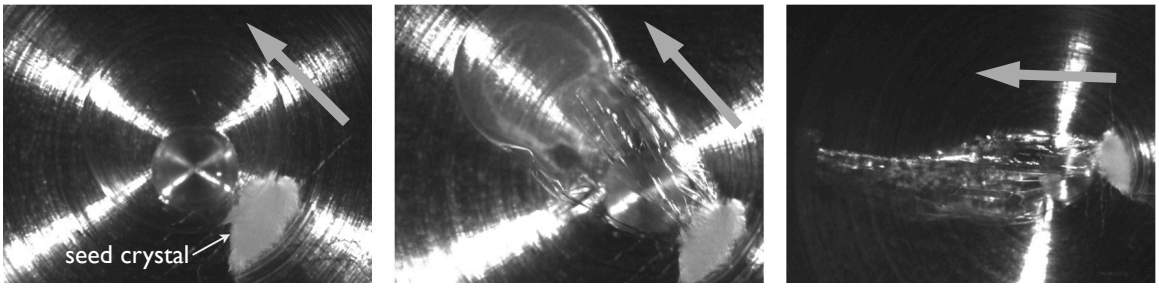

(a) Hydrate growth sequence, arrow indicates the growth direction away from the seed crystal

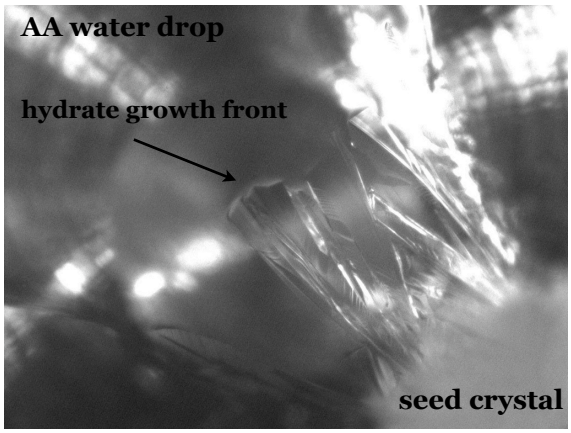

(b) Intermediate stage in the above growth sequence

Figure 3.23: Cyclopentane hydrate morphology after seeding the AA containing water drop (1% by wt) with an external hydrate crystal, oil phase: cyclopentane, $C_{S80} = 0.1\%$ (v/v). Final morphology is a comet like faceted hydrate shell as shown in part (a), $T = 0.2^{o}$C.

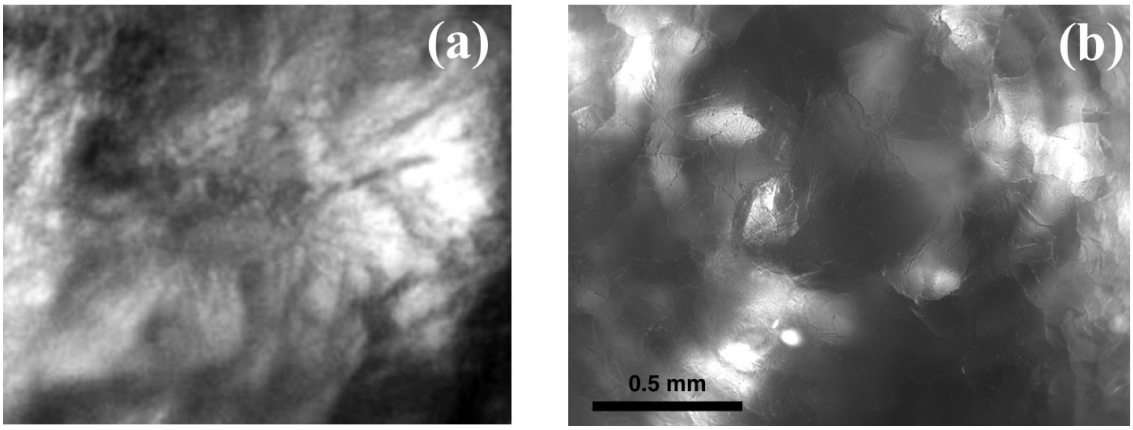

Figure 3.24: Comparison of hydrate morphologies at a water drop, (a) propane, 0.2°C and 0.38 MPa , (b) cyclopentane, 0.2°C. No surfactant present.

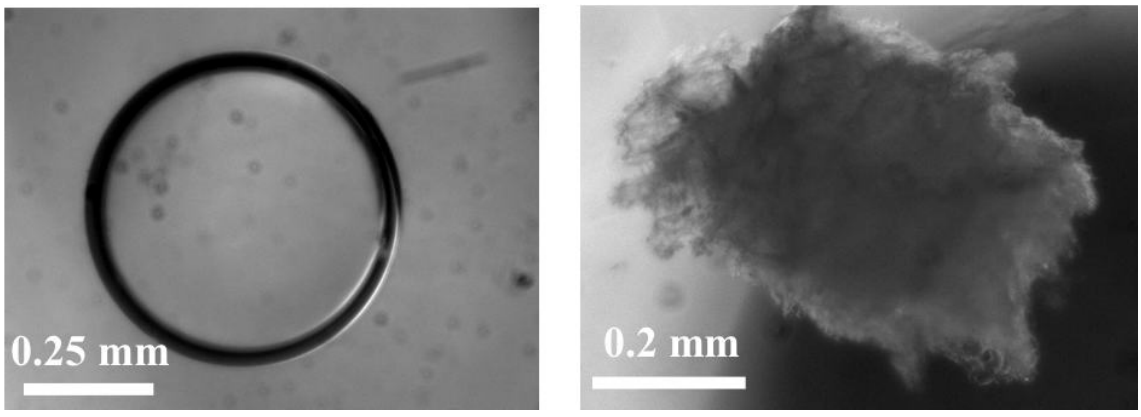

Figure 3.25: Effect of Span 80 on propane hydrate morphology: water drop in light mineral oil, $C_{\mathrm{S80}} = 0.1\%$ (v/v), $T = 0.2$°C, (a) initial water drop, (b) hairy hydrate ball.

3.4 Conclusion

Experimental observations of cyclopentane hydrate growth show that the morphology is dramatically impacted by the surfactant loading and the temperature. A crucial feature in this system with the need for a 'reaction' between components on the two sides of the formation of crystals at an interface is that interfacial properties have a significant impact on the hydrate crystal morphology. In the absence of any surfactant, lateral growth of hydrate leads to a thin shell formation around the water drop with unreacted liquid water trapped inside. This faceted, polycrystalline shell formed by the joining of numerous hydrate facets slows down further radial growth of hydrate due to mass transfer limitations.

The flat cyclopentane hydrate crystals observed during the lateral growth in the absence of surfactant are replaced by unique hollow-conical crystals which grow away from the interface as well as laterally at surfactant (Span 80, sorbitan monooleate) concentrations beyond 0.01% (v/v). The observed crystal behavior is found to be dependent on Span 80 concentration and temperature, and our work supports the argument that this dependence is due to the critical role played by the relative rates of desorption of Span 80 molecules and lateral crystal growth. Growth only in the interfacial zone combined with the competition for the interface between the crystals and surfactant is believed to be the key factor in the mechanism leading to the hollow-conical growth. The conical crystals observed in this study, with dimensions ranging from 10^2 – 10^3 microns, are unique in the crystallography literature to the best of our knowledge. The conical hydrate crystals are preferentially wetted by water and become immersed in the water phase as a consequence of water filling the cone, regenerating the water-oil interface for further hydrate formation. The sequence of lateral crystal growth in the conical form and crystals merging back into the water

phase followed by outward radial flow of water leads to the observed hairy / porous hydrate morphology.

The cyclopentane hydrate surface, either faceted shell or hairy, is highly hydrophilic in nature supported by the observed instantaneous spreading of pure water. The presence of commercial anti-agglomerant appears to make the water phase less hydrophilic and thus reduces this observed tendency of water to wet the hydrate surface. The slightly hydrophobic nature of water in the presence of anti-agglomerant also inhibits the merging of hydrate crystals into the water phase and inhibits the hairy hydrate growth.

The observed similarities in the hydrate morphology of propane (high pressure) and cyclopentane (atmospheric) hydrate, both with and without surfactant, suggest that the cyclopentane hydrate is a very good atmospheric model for high pressure gas hydrates.

Chapter 4

Rheology of cyclopentane hydrate-forming emulsions

4.1 Introduction

Development of an excessive pressure drop along the flow line is one of the critical issues associated with almost every flow assurance problem related to solid build-up by paraffins, scales, asphaltenes and hydrates. Deposition of hydrates can be more severe as it may not only lead to large pressure drops but can possibly block the pipeline leading to unplanned shutdowns. In addition, the hydrate growth is more rapid and unpredictable than the deposition problems associated with waxes or asphaltenes. Though various mitigation strategies are available to tackle hydrate issues, understanding the rheological properties of fluids after hydrate formation is a very important aspect in the design of subsea facilities. The hydrate mitigation strategy of *slurry flow* using techniques like addition of anti-agglomerants or cold flow technology, in particular, calls for a detailed knowledge of rheological properties before and after hydrate formation.

A limited amount of work has been done in the past and we will briefly review the studies related to hydrate slurry rheology. Camargo et al. [76, 77] studied

rheological characteristics of gas hydrate suspensions in asphaltenic crude oil using a laboratory scale Pressure-Temperature (P-T) cell which acts as a double coaxial cylinder configuration rheometer. A mixture of 90% methane and 10% ethane on molar basis is used as the gas phase in their study. They reported that hydrate suspensions exhibit shear thinning and thixotropic behavior, and shear thinning becomes more pronounced in concentrated suspensions, speculating that this thinning behavior is related to colloidal interactions between solid particles. Camargo et al. [77] also proposed a phenomenological model relating the viscosity of hydrate suspension to the size of aggregates, resulting from the balance between attractive forces and shear stresses. Andersson and Gudmundsson [78] characterized hydrate-in-water slurry flow properties in a flow loop built at Norwegian University of Science and Technology (NTNU), where a tube viscometer is a part of their flow loop. Sinquin et al. [79] characterized flow properties of hydrate particles dispersed in the oil phase in laminar and turbulent flow regimes. In the laminar regime, Newtonian behavior is reported in most cases and relative viscosity is found to increase with the increasing hydrate solid fraction. However, at large solid contents when the inter-particle forces can be high, they observed a shear thinning behavior and modeled it by introducing an effective volume fraction depending on the aggregation rate. Similarly, in the turbulent regime, the friction factor is found to increase with the emulsion water cut. Sinquin et al. also mentioned that settling may be dominant for low viscosity oils at low velocities, and thus rheology is difficult to characterize in such systems. In a flow loop reactor operating on a gas-lift principle, Fidel-Dufour et al. [80] studied rheology of methane hydrate slurries obtained from water-in-dodecane emulsion in the presence of an anti-agglomerant additive IPE202 patented by IFP (Institut Français du Pétrole, France). They assumed the agglomeration between hydrate particles and water drops to be irreversible, modeled it using the population balance approach, and reported

that hydrate aggregates are porous in nature (fractal dimension = 1.8). Colombel et al. [81] proposed a unified model for the agglomeration between hydrate particles in *w/o* emulsion where they combined contact-induced agglomeration and shear-limited agglomeration to predict the viscosity of slurry during hydrate formation. In terms of rheological characterization of gas hydrates using commercial laboratory scale rheometers, Schüller et al. [82] have used Physica UDS200 and Physica MCR500 rheometers coupled with a high-pressure cell, while Rensing et al. [83] utilized a high-pressure cell from TA Instruments on the AR G2 rheometer for shear and oscillatory measurements. A standard rheometer with a high-pressure cell usually allows narrower operating parameter space than atmospheric operation due to added experimental constraints.

To overcome the practical difficulties associated with high-pressure conditions necessary for gas hydrate rheology, an atmospheric pressure model system, ensuring a safe operation under ambient conditions, is a possibility. Using the similarities in the hydrate and ice properties, as both mostly contain water, Rensing et al. [84] used ice slurry as an analogue for hydrate slurry. They studied rheological properties of ice slurries in water-in-crude oil emulsions over a wide range of water volume fractions, ranging from 0.1 to 0.7, using either fresh water or brine. Detailed and carefully performed shear rheology and yield stress measurements are reported in their study, but the work significantly lacks in comparing the results with any hydrate rheology data. Though ice is a simple analogue to hydrates, a comparison with the hydrate rheology will explain the amount of transferable information from a model ice system to actual hydrates. To this end, we have used an atmospheric pressure hydrate former cyclopentane as the guest molecule. As a model system, cyclopentane offers several advantages over ice – it forms structure II hydrates which are the most common form encountered in petroleum fields and it is immiscible with

water, which introduces the mass transfer limitations usually present in case of gas hydrate emulsion systems. Recall that, gas in such systems is usually soluble in the oil phase at elevated pressures. Also, the observed qualitative similarities in the morphological characteristics of cyclopentane and propane hydrate, as reported in the crystal morphology study, suggest that cyclopentane is a better atmospheric model for high-pressure gas hydrates as compared to ice.

In the present study, we present the rheological characteristics of both water-in-oil (w/o) and oil-in-water (o/w) cyclopentane hydrate-forming emulsions. We begin in the next section with description of experiments, followed by the discussion on w/o emulsions. The results are presented for a range of water cuts at a fixed shear rate of 10 s^{-1} and at variable shear rates for a 25% w/o emulsion. Combining the understanding from morphological characteristics of cyclopentane hydrates with the rheology data, a mechanism is proposed to explain the viscosity evolution during hydrate formation in oil-continuous emulsions, supported by data at different temperatures and surfactant loadings. This is followed by the description of o/w emulsions. It is observed that w/o emulsions are stable up to 45% by volume of internal water fraction, with 45% - 57.5% found to be the transition period where emulsions are unstable; above this water fraction, the emulsion inverts to form water-continuous emulsions. In the following section, we present a probability analysis of hydrate formation, with change in viscosity as a criterion to detect the hydrate formation in 40% by volume w/o emulsion. The effect of sub-cooling and shear rate on the critical time for hydrate formation is reported. The evolution of emulsion viscoelastic properties during the hydrate formation for a range of water cuts is presented towards the end.

4.2 Experimental section

4.2.1 Material properties

The oil phase of emulsions in this study is a mixture of three oils: light mineral oil, Halocarbon 27 oil and cyclopentane. The density and viscosity of Halocarbon 27 oil are 1.9 gm/cm^3 and 100 cP respectively, the properties of other components are reported in Chapter 2. Composition of the oils is adjusted to achieve the oil mixture density close to that of dispersed phase water at 25°C. Cyclopentane constitutes 50% of the oil phase volume. Though the density matched oil phase will not remain density matched over all the operating temperatures, it certainly helps in reducing the effects associated with sedimentation due to density difference.

The temperature dependence of the viscosity of each oil is given in Figure 4.1. The oil data points were obtained from ramps of increasing and decreasing shear rate using a cone/plane or a Couette geometry; water viscosity results are from the International Organization for Standardization and from the review by Debenedetti [85], while the cyclopentane viscosity data are from Ma et al. [86].

For the light mineral oil for $T < -15$°C, error bars increase greatly and it has been suggested that the oil undergoes wax formation. For the Halocarbon oil, the pour point is -40°C. All the experiments presented in this work are with temperatures well above these transitions.

4.2.2 Emulsions

The emulsions of different compositions are prepared by a drop-wise addition of dispersed phase into the continuous phase, and applying mechanical stirring using a IKA T25 digital Ultra-Turrax homogenizer operating at 7000 rpm for 5 minutes. Each

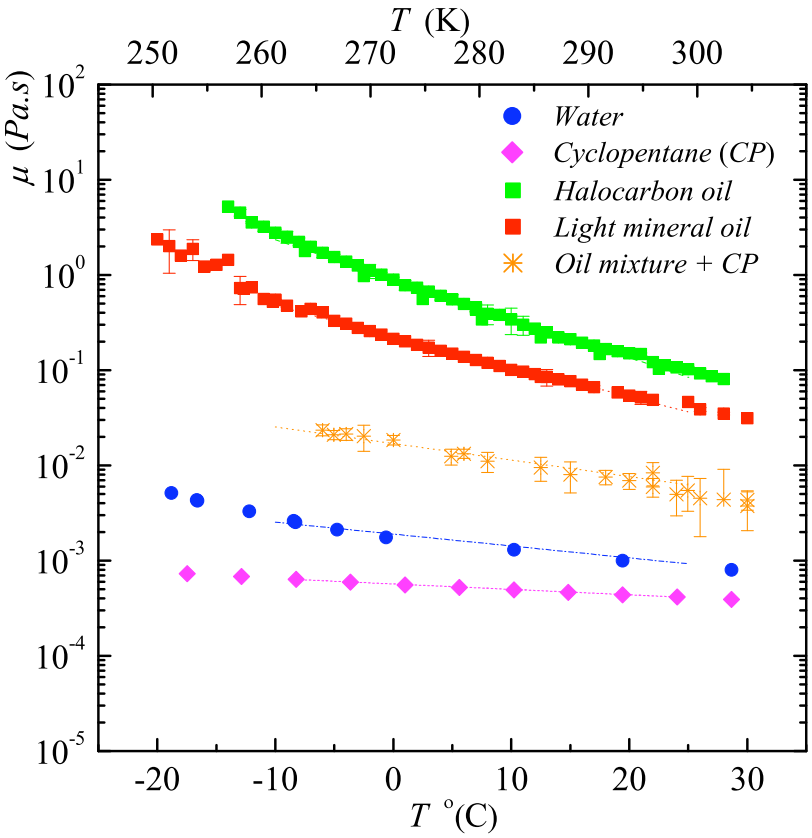

Figure 4.1: Shear viscosity versus temperature for the Halocarbon oil, the light mineral oil, the density matched oil mixture (containing cyclopentane), the standard and supercooled water, and the cyclopentane. Water data from International Organization for Standardization and Debenedetti (2003); cyclopentane data from Ma et al. (2003).

Emulsion	Time (hours)	Mean drop size (μm)	Standard deviation (μm)
25% *w/o*	0	8.1	3.7
25% *w/o*	24	9.3	4.6
30% *o/w*	0	11.2	5
30% *o/w*	24	11.5	4.8

Table 4.1: Droplet size distribution of emulsions as a function of time.

time a 60 ml emulsion sample is prepared in a standard 100 ml beaker. Reproducibility of emulsion droplet size has been confirmed from optical microscope photomicrographs (Nikon AZ100). A freshly prepared emulsion sample, with 80% dilution of 25% *w/o* and 70% dilution of 30% *o/w* emulsion into respective continuous phases, is transferred into a rectangular capillary (0.1 $\times$ 1 mm) placed over a glass slide for microscopy. Figures 4.2 and 4.3 show photomicrographs of the 25% *w/o* and 30% *o/w* emulsions respectively up to 24 hours after preparation. Emulsions are found to be stable against coalescence for several hours as the droplet size distribution remains roughly constant (see Table 4.1). The variations seen are believed to be a result of sampling rather than an evolution in size.

4.2.3 Rheology

The rheology data is obtained using a stress-controlled AR 2000 rheometer equipped with a concentric cylinder geometry with a stator diameter of 30 mm, rotor diameter of 28 mm and length of 42 mm. A typical sample size used in this geometry is 19.6 ml. The temperature is controlled with a Peltier jacket and is monitored through thermocouple. The rheometer geometry is always well insulated from the surrounding to minimize moisture condensation at low temperatures.

The emulsion prepared at room temperature is gently transfered to the rheometer where the temperature is previously set to 15°C. The temperature is then decreased

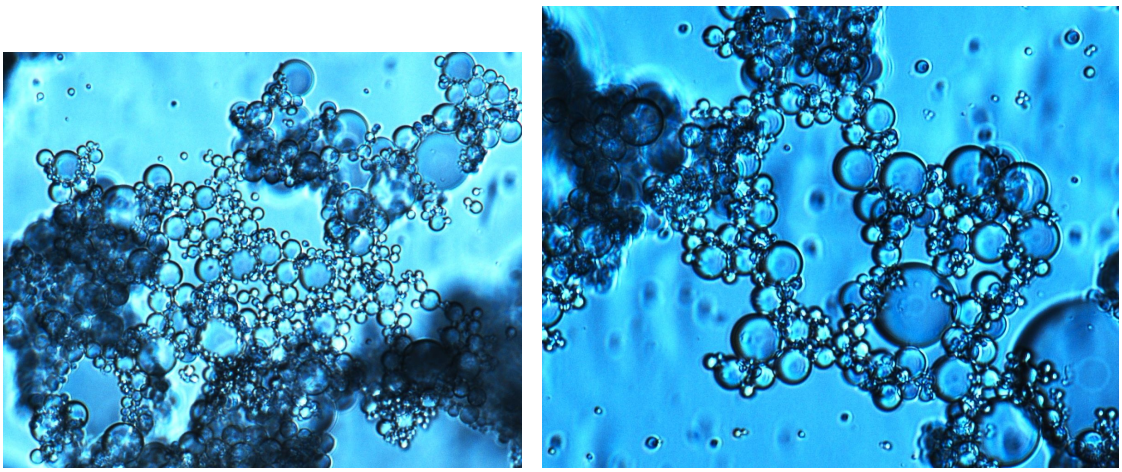

(a) 0 hours (b) 24 hours

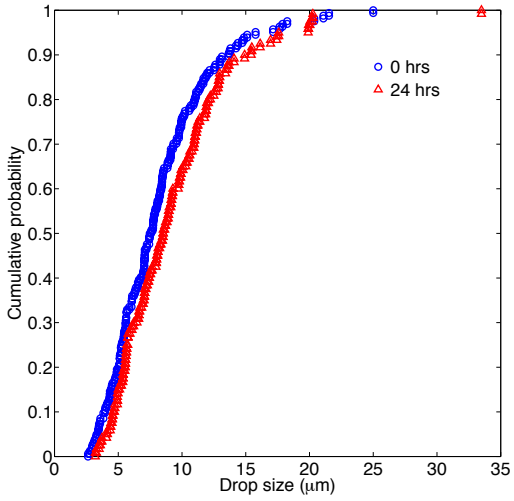

(c) Cumulative probability

Figure 4.2: Photomicrographs [225 μm $\times$ 180 μm] and drop size distribution of 25% *w/o* emulsion. Time is reported after emulsification.

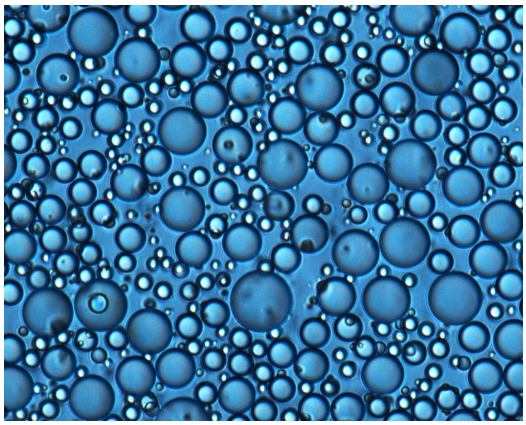

(a) 0 hours

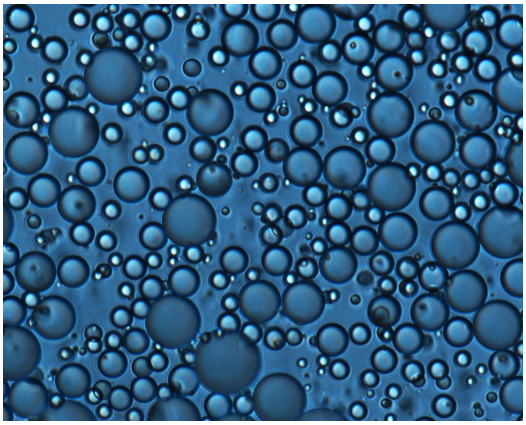

(b) 24 hours

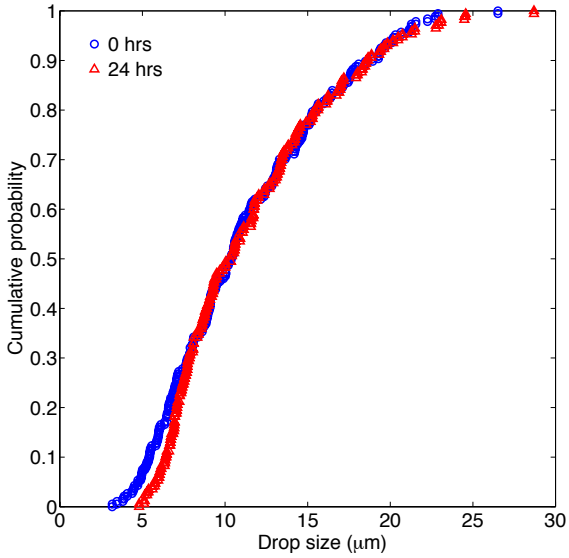

(c) Cumulative probability

Figure 4.3: Photomicrographs [225 μm $\times$ 180 μm] and drop size distribution of 30% *o/w* emulsion. Time is reported after emulsification.

to T_{hold}, with a temperature ramp of 2°C/min at a fixed shear rate ($\dot{\gamma}$); T_{hold} = -2°C for *w/o* emulsions and 0.2°C for *o/w* emulsions in most of the cases. To overcome the long and stochastic induction time associated with cyclopentane hydrate nucleation, the emulsion is seeded with externally-grown cyclopentane hydrate seed crystals as soon as temperature reaches T_{hold} and is assigned as a zero time.

4.3 Results and discussion

4.3.1 Oil-continuous emulsions

Figure 4.4 shows viscosity evolution for oil-continuous emulsions with variable water cuts at T_{hold} = -2°C and $\dot{\gamma} = 10\ \text{s}^{-1}$. A relatively slow increase in the viscosity is observed in each case at early times after seeding, followed by a more rapid upturn in the viscosity. In case of high water cut emulsions, this rapid upturn is very abrupt and leads to development of a sufficient yield stress to stop the flow. Stoppage of the flow indicates development of a yield stress above the instrument limit, and this stress is τ_y ($\phi_{w/o}$ = 0.3, 0.4) > 3000 Pa. At lower water cut emulsions, *e.g.* $\phi_{w/o} = 0.25$, a break in the curve shows that the material has achieved a maximum in stress which we call as an approximate yield stress of the material at this water cut, *i.e.* τ_y ($\phi_{w/o}$ = 0.25) ≈ 300 Pa. The final hydrate slurry viscosity is found to decrease with drop in water cut as water is the limiting component in case of oil-continuous emulsions. For example, at $\phi_{w/o} = 0.4$ cyclopentane is present ∼ 2.5 times the stoichiometric requirement to convert all water into hydrates.

Figure 4.5 shows the effect of shear rate on the viscosity evolution of 25% *w/o* emulsion. A similar behavior of initial slow rise in viscosity followed by a rapid upturn is observed for each shear rate. At low shear rate of $\dot{\gamma} = 1\ \text{s}^{-1}$, the abrupt

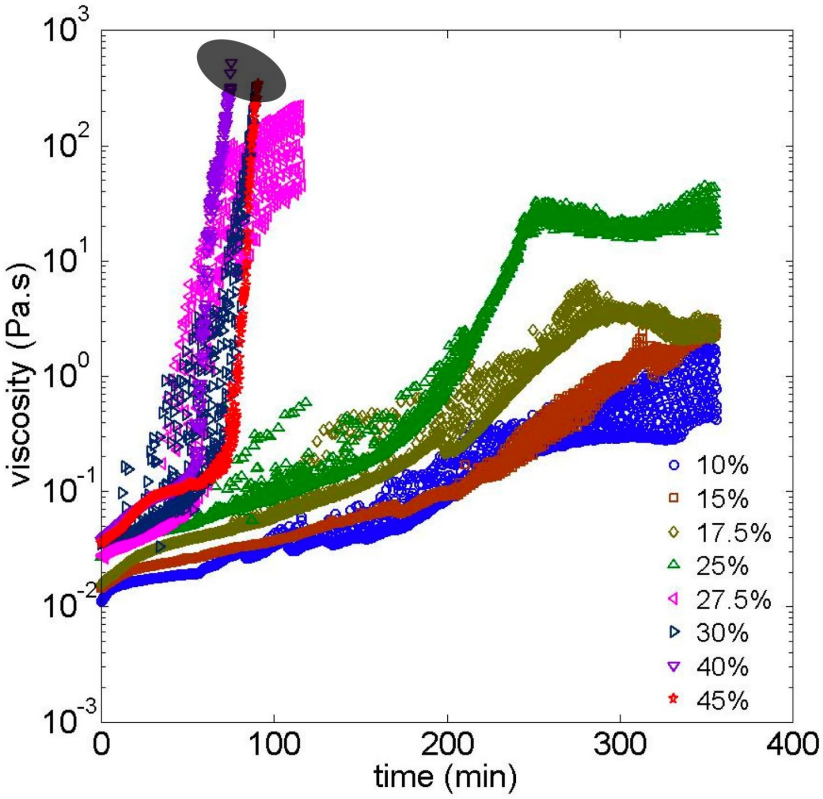

Figure 4.4: Viscosity vs. time for variable water cut *w/o* emulsions, $\dot{\gamma} = 10\ \mathrm{s}^{-1}$, T = -2°C = -2°C, seeding with external cyclopentane hydrate crystals at 0 minutes. Marked points in grey represent rheometer jamming.

viscosity upturn leads to development of the yield stress above the instrument limit and stops the flow. With increasing shear rate, it is observed that the rapid upturn in viscosity occurs relatively at earlier times and the final hydrate slurry viscosity decreases. Figure 4.6 shows the viscosity of hydrate slurry obtained from 25% *w/o* emulsion as a function of shear rate at which it is formed. The final hydrate slurry is then subjected to increasing and decreasing shear rate ramps where it is sheared for 10 minutes at each shear rate. The results are shown in Figure 4.6. The hydrate slurry exhibits a shear thinning behavior and the shear rate during formation appears to have a major effect on the slurry properties. The unusual hysteresis, *i.e.* larger viscosities at decreasing shear rates after material have been sheared at a higher shear rate, is observed in some cases like 10 s^{-1} data in Figure 4.6, clearly indicates the complicated nature of the material. A rough estimate of the shear thinning index n, with viscosity μ of form $\mu \propto \dot{\gamma}^{(n-1)}$, is found to be in between 0.4 to 0.2 for the hydrate slurry obtained from 25% *w/o* emulsion.

The change in viscosity after hydrate formation for the *w/o* emulsions is roughly an order of magnitude. Clearly, a simple transition from water droplets to rigid hydrate spheres cannot explain such a large increase in the viscosity. As shown for the studies with single millimeter size drops in Chapter 3, the presence of Span 80 in the oil phase leads to a hairy and porous cyclopentane hydrate morphology. This hairy hydrate ball is almost 20-30% larger in diameter as compared to the initial water drop and thus leads to development of porosity (ϵ) into the system. For small water drops of 10 μm size as observed in emulsions, a hydrate crystal comparable to the size of drop grows quickly and immediately develops into the hairy structure. This should lead to increase in the porosity immediately after onset of hydrate formation, rather than after a delay as in the mm scale drops. Also, it is observed that the hairy cyclopentane hydrate surface is highly hydrophilic in nature. Any water drops in the

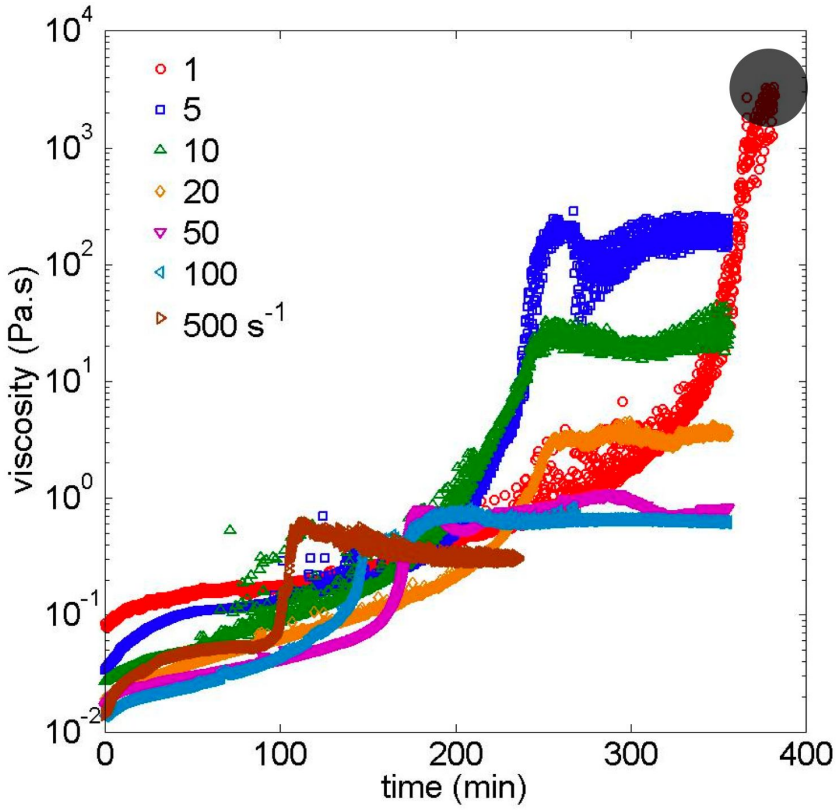

Figure 4.5: Viscosity vs. time for 25% *w/o* emulsion at variable shear rates, T = -2°C, seeding with external cyclopentane hydrate crystals at around 0 minutes. Marked point in grey represents rheometer jamming.

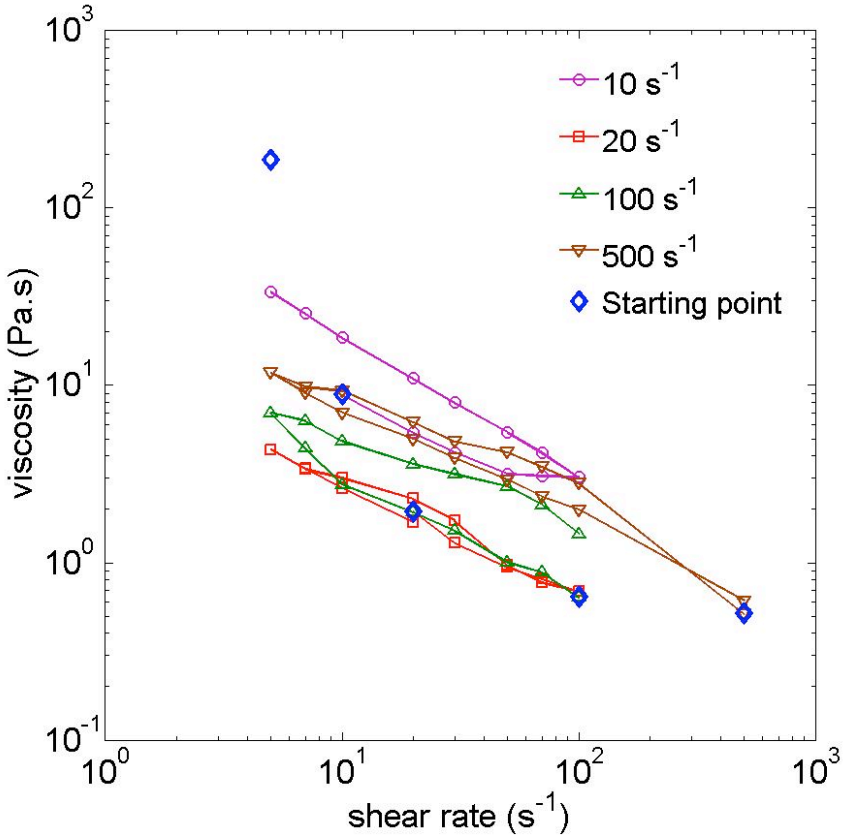

Figure 4.6: Shear rate ramps on the hydrate slurry obtained at a fixed shear rate, hollow blue diamonds represent the initial slurry viscosity for 25% *w/o* emulsion *i.e.* end points of Figure 4.5. Slurry undergoes cycle of increasing-decreasing shear rates in each case. $T = 0.2^{o}$C

vicinity completely wet the hydrate surface and undergo further hairy hydrate growth. The porosity allows the effective volume fraction ϕ_{eff} to be considerably larger than the initial water volume fraction ϕ_{o}; $\phi_{\text{eff}} = \phi_{\text{o}}/(1-\epsilon)$.

Based on our experimental observations, we propose a hypothesis to explain the viscosity evolution during hydrate formation in oil-continuous emulsions, as shown in Figure 4.7. Random nucleation leads to conversion of a few water drops into hairy hydrate balls which get immediately wetted by adjacent water drops. The wetted water film around the hydrate surface may serve as a liquid bridge to facilitate the agglomeration of hydrate particles and can itself undergo further hydrate formation. As the hairy hydrate growth spans the volume, it leads to porosity development and increases the effective dispersed phase volume fraction. The hairy and porous hydrate structure, enhanced due to water wetting characteristics of the hydrate surface, will lead to a jammed state if the applied stress is lower than the yield stress of the material. If the applied stress exceeds the yield stress of the material, it will break down the structure and in turn will limit the viscosity increase, as observed in Figure 4.5. As per our hypothesis, the water wetting tendency of hydrophilic hydrates suspended in the hydrophobic oil phase has a significant impact on the hydrate agglomeration process. If the water wetting tendency of hydrates is reduced or eliminated, hydrate particles should remain isolated from each other and thus remain flow-able. To validate the point, similar experiments are performed for the 25% *w/o* emulsion at a fixed shear rate of 10 s^{-1} but at variable sub-coolings. Higher sub-cooling should lead to faster conversion of water drops into hairy hydrate balls without allowing enough time for unreacted water droplets to wet the hydrate surface. Figure 4.8 shows the viscosity evolution at four different experimental temperatures. The final hydrate slurry shows almost an order of magnitude drop in viscosity for 4°C of increase in sub-cooling. On a similar front, Sjöblom et al. [63] concluded

that capillary attractive forces between hydrate particles due to free water films are a key cause of hydrate agglomeration and plugging. As reported by Sjöblom et al., the liquid water film thickness on the hydrate surface is found to decrease with the increasing sub-cooling and thus led to the observed decreasing trend of hydrate particle-particle adhesion force with increase in sub-cooling. In another set of studies, McCulfor et al. [87] studied suspension of glass particles in mineral oil as a model system for hydrate suspension and reported that addition of small amounts of water leads to large increases in viscosity due to formation of water bridges between glass particles that give rise to capillary forces between them. McCulfor et al. also studied the effectiveness of two surfactants, Span 80 (same surfactant as used in our study) and Arquad 2HT (quaternary ammonium salts), as anti-agglomerants in reducing the viscosity increase observed in the presence of added water. A fairly gradual decrease in the suspension viscosity is observed as Span 80 concentration is increased from 0.05% to 1% by wt, but only 0.05 wt % addition of Arquad 2HT is found to bring the viscosity down to the value obtained without added water and thus showing more effective anti-agglomerant properties. The observed behavior with Arquad 2HT is explained through an increase in the contact angle of water on glass in the presence of oil (static contact angle $\approx 160^{o}$) and thus greater reduction in the ability of water to wet the glass particles.

We have also observed that Span 80 loading alters the rheological behavior of our hydrate-forming emulsion. A higher surfactant loading leads to a lower slurry viscosity, as seen in the data for 15% *w/o* emulsion in Figure 4.9(a), but reducing Span 80 loading result in a rapid increase and higher viscosity at such a low water cut. A similar effect is observed for high water cut emulsions, as shown in Figure 4.9(b), where lower Span 80 loading results in development of high yield stress but an abundance of Span 80 improves the flowability, thus acting as an anti-agglomerant.

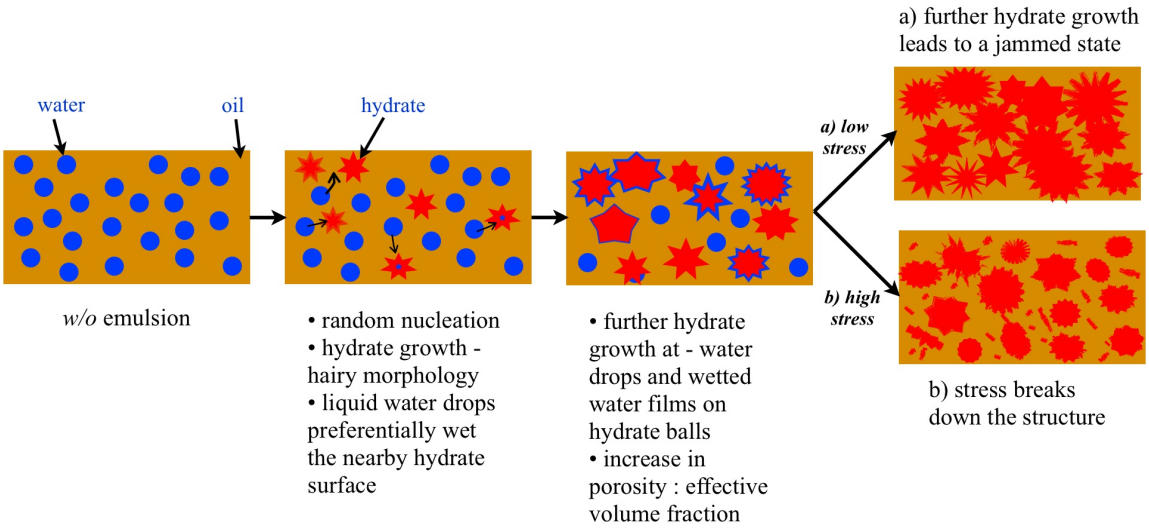

Figure 4.7: Proposed mechanism of hydrate agglomeration in water-in-oil (w/o) emulsion.

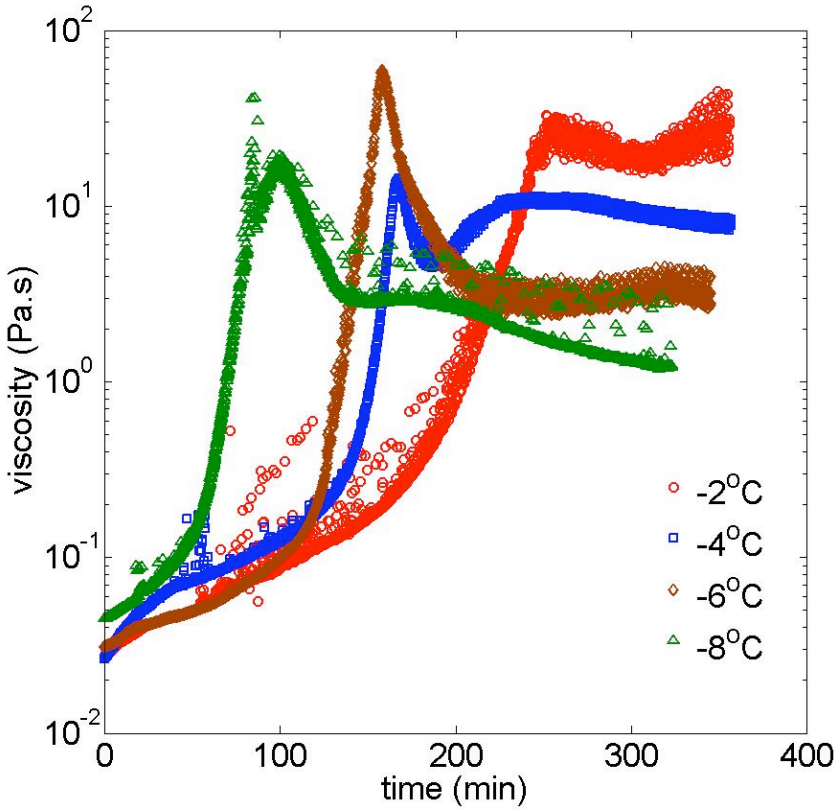

Figure 4.8: Viscosity vs. time for 25% w/o emulsion at variable temperatures, $\dot{\gamma} = 10$ s^{-1}, seeding with external cyclopentane hydrate crystals at around 0 minutes.

The mechanism of this effect is unknown, and may be related to the influence of Span 80 on the contacts between hydrate particles.

4.3.2 Water-continuous emulsions

Figure 4.10 shows the emulsion viscosity as a function of water volume fraction. Data is obtained at $\dot{\gamma} = 10\ s^{-1}$ and $T = 0.2^oC$. A sudden drop in emulsion viscosity going from 45% to 57.5% water volume fraction indicates the inversion of emulsion continuous phase from oil to water. In the transition range of 45% to 57.5% water volume fraction, emulsions are found unstable and thus are not selected for the rheological studies.

Figure 4.11 shows the viscosity evolution during hydrate formation in water-continuous emulsions. Similar to the oil-continuous experiments, hydrate nucleation is triggered by seeding with external cyclopentane hydrate crystals. The water-continuous studies are performed at $T_{hold} = 0.2^oC$ as compared to -2°C used for oil-continuous emulsions to avoid the bulk solidification into ice. In case of high dispersed phase fraction like 40% *o/w*, a rapid rise in viscosity leads to development of a yield stress above the instrument limit and stops the flow. With decreasing oil fraction, a flow-able and less viscous hydrate slurry is obtained.

Water is not the limiting component for most of the water-continuous emulsions, as was the case with oil-continuous emulsions. For example, the water and cyclopentane content in a 38% *o/w* emulsion almost equals the stoichiometric ratio required for cyclopentane hydrate and thus for all the internal oil volume fractions beyond 38%, cyclopentane becomes the limiting component. Also recall that cyclopentane constitutes 50% of the oil phase in our emulsion formulations and the hydrate equilibrium temperature is shown to be dependent on the cyclopentane fraction in

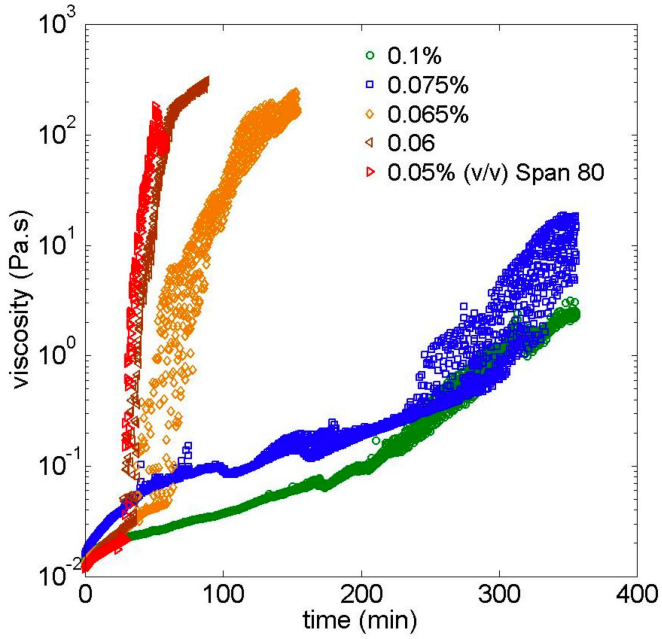

(a) 15% *w/o* emulsion

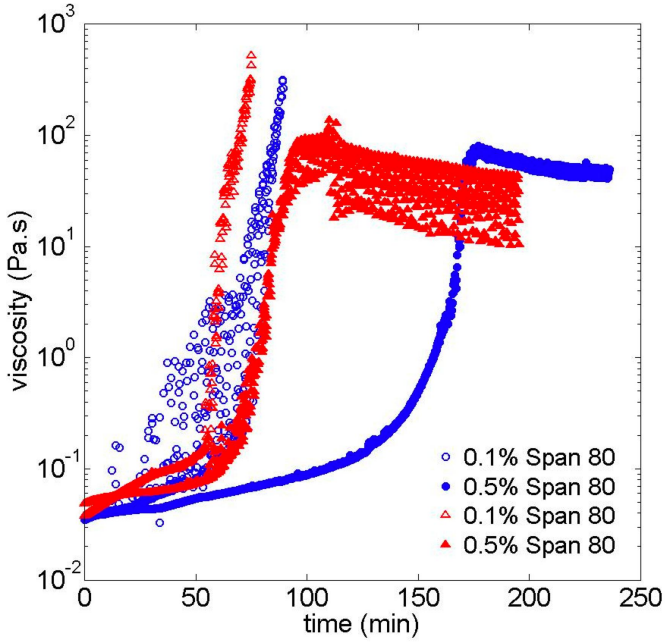

(b) 30% *w/o* (circles), 40% *w/o* (triangles) emulsions

Figure 4.9: The effect of Span 80 loading (% *v/v*) on rheological behavior of *w/o* emulsions, $\dot{\gamma} = 10\ \mathrm{s}^{-1}$, T = -2°C.

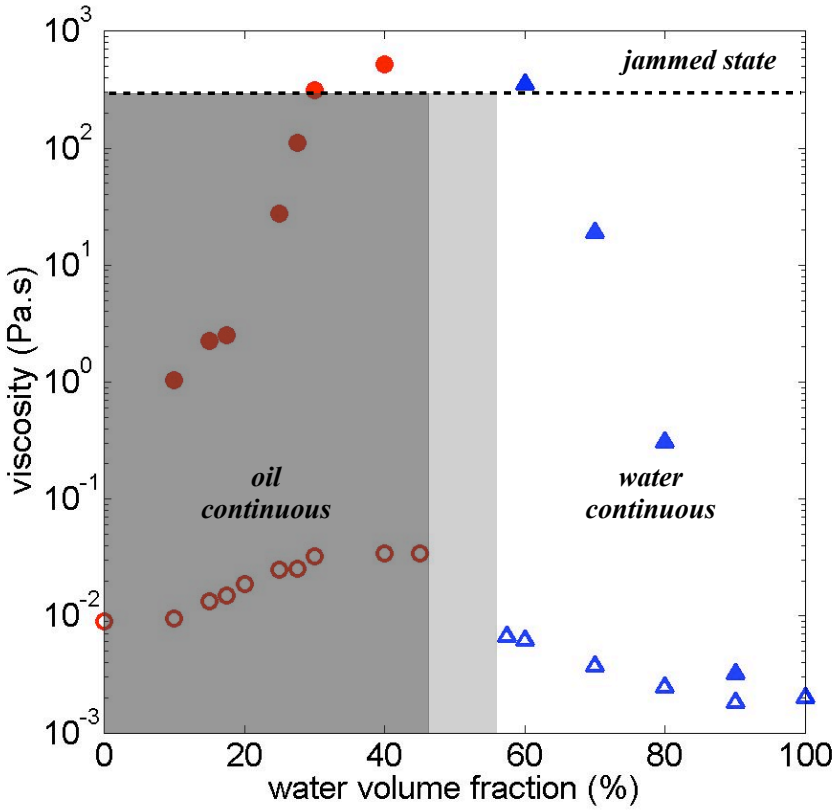

Figure 4.10: Emulsion (open symbols) and hydrate slurry (solid symbols) viscosity for variable water volume fractions, $\dot{\gamma} = 10\ s^{-1}$. circles: oil-continuous and triangles: water-continuous system. The region marked as 'jammed state' beyond $\approx$ 200 Pa.s represents flow cessation due to hydrate plugging.

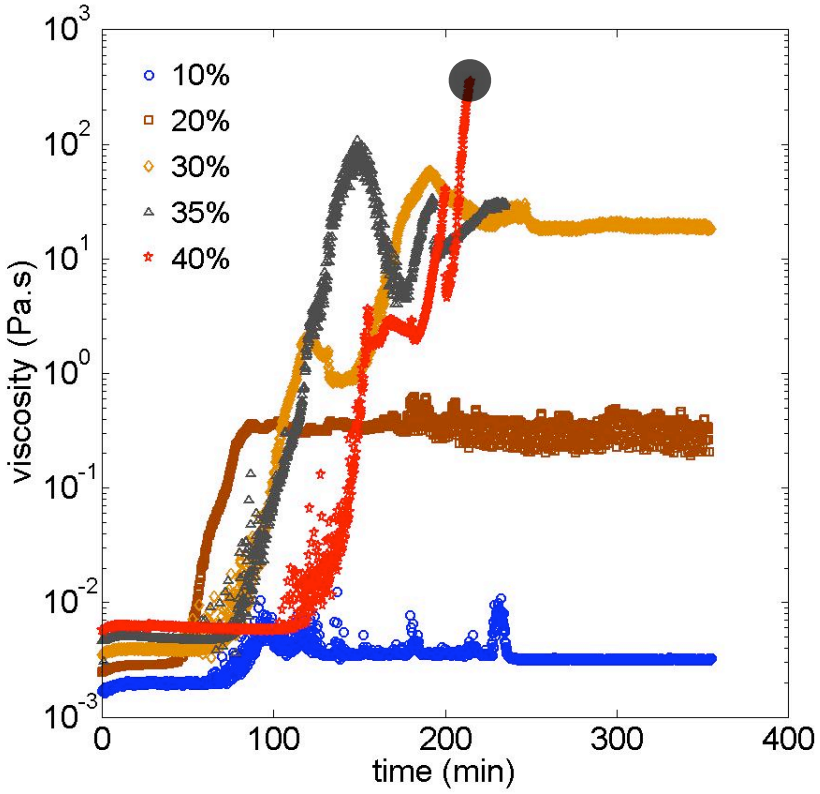

Figure 4.11: Viscosity vs. time for variable oil fraction o/w emulsions, $\dot{\gamma} = 10\ \mathrm{s}^{-1}$, $T = 0.2^{\circ}\mathrm{C}$, seeding with external cyclopentane hydrate crystals at 0 minutes. Marked point in grey represents rheometer jamming.

the oil phase; refer to Figure 18 from Chapter 3. Cyclopentane consumption in the process of hydrate formation will reduce its percentage in the external oil phase. The maximum possible cyclopentane consumption into hydrates will be limited by the minimum required percentage in the oil phase to maintain the hydrate equilibrium point above the experimental temperature $T = 0.2$°C.

Figure 4.12 shows the effect of shear rate on the viscosity evolution for 30% *o/w* emulsion. The hydrate slurry viscosity is found to decrease with increasing shear rate. Figure 4.13 shows the viscosity of hydrate slurry as a function of shear rate at which it is formed, marked as starting point. The hydrate slurry is then subjected to continuous cycles of increasing and decreasing shear rates where it is sheared for 10 minutes at each shear rate. It is observed that shear rate cycles bring the final slurry viscosity values close to each other for all the slurries obtained at different formation shear rates. Unlike oil-continuous emulsions, the water-continuous hydrate slurries follow a usual hysteresis behavior, *i.e.* slurry sheared at high shear rate exhibits lower viscosities during decreasing shear rate ramp. In Figure 4.13, the hydrate slurry formed at 500 s^{-1} exhibits minimal hysteresis while the slurry formed at 1 s^{-1} has the maximum hysteresis and eventually attains similar viscosities as obtained for the 500 s^{-1} case. For the hydrate slurry obtained from 30% *o/w* emulsion at 500 s^{-1}, the shear thinning index $n \approx 0.33$.

Figure 4.10 shows the hydrate slurry viscosity for all the water volume fractions studied here. Similar to the emulsion viscosity, the hydrate slurry viscosity increases with increasing water volume fraction and then follows a decreasing trend as the emulsion inverts from oil-continuous to water-continuous. In both the emulsions, higher end of dispersed phase fractions, *i.e.* roughly 30% to 60% of water volume fraction, lead to rheometer jamming. This suggests that one of the possible ways to mitigate hydrate plugging in high water cut water-in-crude oil emulsions is to enhance

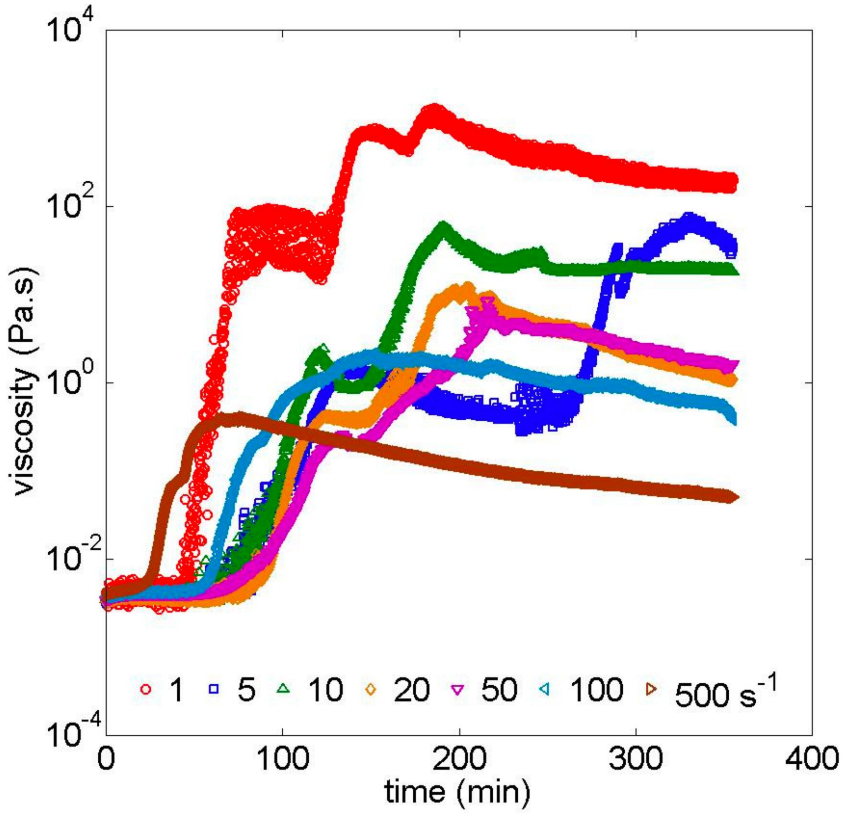

Figure 4.12: Viscosity vs. time for 30% *o/w* emulsion at variable shear rates, $T = 0.2^{o}$C, seeding with external cyclopentane hydrate crystals with time measured from the point of seeding.

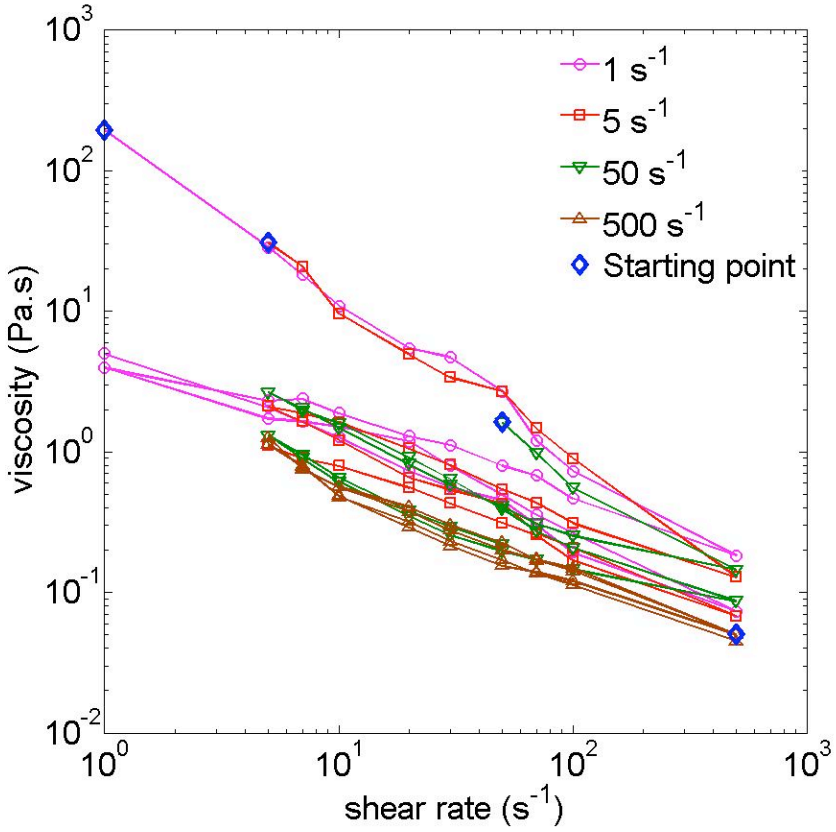

Figure 4.13: Shear rate ramps on the hydrate slurry obtained at a fixed shear rate, hollow blue diamonds represent the initial slurry viscosity for 30% *o/w* emulsion *i.e.* end points of Figure 4.12. Slurry undergoes 2 cycles of increasing-decreasing shear rates in each case. T = 0.2°C

the water amount to invert the emulsion and make a flowable hydrate slurry in water.

4.3.3 Probability analysis of hydrate formation

A 40% *w/o* emulsion is selected for this set of studies and the data is obtained using a strain-controlled ARES rheometer equipped with a Couette geometry having a cup diameter of 34 mm, cylinder diameter of 32 mm, and cylinder length of 33.5. The temperature is set using a cooling bath and monitored with a thermocouple placed at the bottom of the cup. The emulsion composition is exactly same as described before except that Span 80 is added at $C_{\mathrm{S80}} = 0.05\%$ (v/v).

The hydrate formation is studied by a rapid temperature quench of the emulsion and the viscosity is recorded as a function of time. Note that there is no seeding with external cyclopentane hydrate crystals and the hydrate nucleation occurs randomly under the applied sub-cooling. The emulsion prepared at room temperature is gently transfered to the rheometer where the temperature is previously set to the lower working temperature and set into motion. The viscosity measurements are performed for different shear rates and variable experimental temperatures. Figure 4.14 shows a viscosity evolution for the 40% *w/o* emulsion at T = -6.3°C and -9.8°C for $\dot{\gamma} = 10$ s^{-1} and 1 s^{-1} respectively. The viscosity first increases slightly due to temperature effects, then stays constant until a critical time t_c, as defined in Figure 4.14(a), whereupon it rapidly increases by orders of magnitude. This dramatic measured viscosity change is qualitatively reproducible, but not at the same t_c value. However, for a set of ten runs, a range of critical times is obtained. The large scatter observed at the final state seems to be associated with slip and therefore the actual value of the viscosity is probably not meaningful in this case, except to indicate that the material has become dramatically more efficient in stress transition.

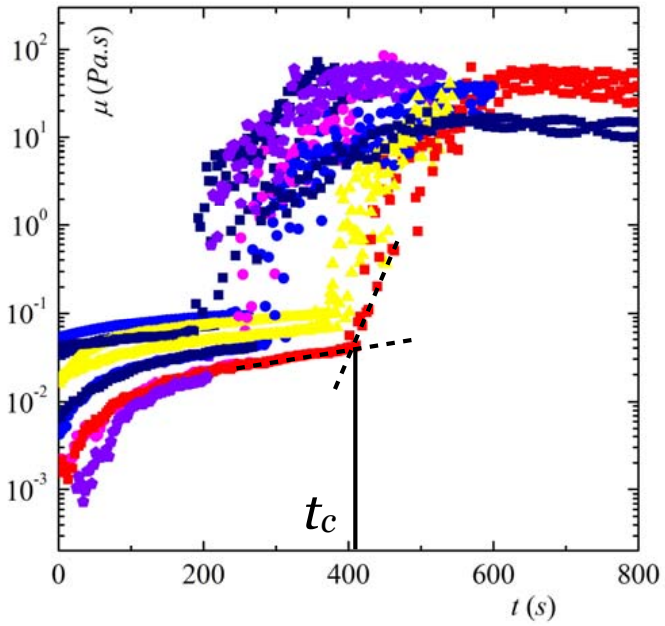

(a) T = -6.3 ± 0.6°C, $\dot{\gamma}$ = 10 s^{-1}

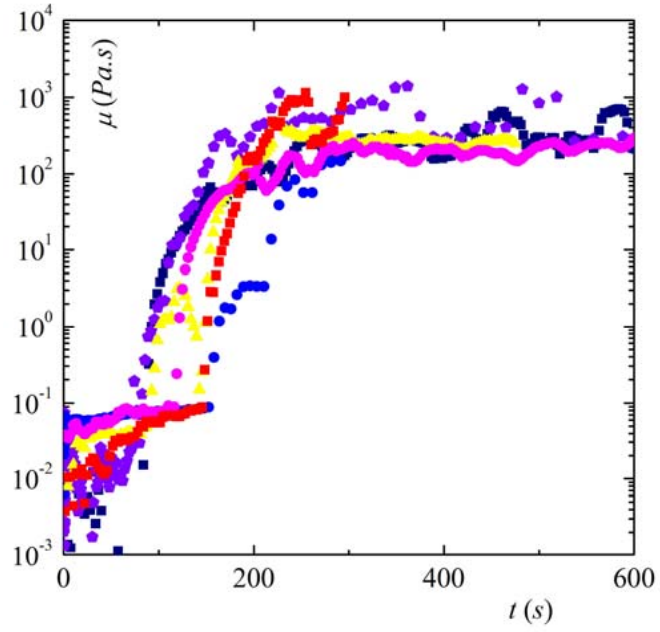

(b) T = -9.8 ± 0.6°C, $\dot{\gamma}$ = 1 s^{-1}

Figure 4.14: Hydrate-forming 40% *w/o* emulsion, viscosity (μ) versus time. Different symbols denote different replicates, all at the stated conditions.

Experiments at three different temperatures and three different shear rates have been performed so that the cumulative critical time probability $P(t_c)$ can be measured. A value of $P = 0$ means that the large viscosity increase did not occur in any cases at this time, and $P = 1$ means the irreversible transformation occurred in all cases by this time. Another measure which can be extracted from the probability is the time required for half the experiments to exhibit the abrupt viscosity increase, $t_{1/2}$ and is represented as a function of shear rate for different temperatures. Figure 4.15 shows critical time probability P and half time $t_{1/2}$ for the 40% *w/o* hydrate-forming emulsion. The critical time probability P at different shear rates is found to be predominantly controlled by the temperature, *i.e.* the level of sub-cooling. Also, the half-life critical time $t_{1/2}$ increases with the temperature and seems to be independent of the shear rate in case of 40% *w/o* emulsion.

4.3.4 Oscillatory rheology

AR 2000 rheometer with a concentric cylinder geometry is used for the oscillatory tests. The emulsion is transfered to the rheometer at room temperature and then the temperature is decreased to T_{hold} at 2°C/min, where it is held constant. The oscillatory stress is fixed at 0.05 Pa at a frequency of 1 Hz. Figure 4.16 shows the evolution of storage modulus (G') for variable water cut *w/o* emulsions at T_{hold} = -10°C.

Similar to the rapid viscosity increase observed in the rapid temperature quench shear rheology experiments, G' for the 40% *w/o* emulsion suddenly increases by several orders of magnitude at the onset of hydrate formation, as shown in Figure 4.16(a). The temperature dependence of critical time for the phase transition is observed in oscillatory tests as well. The critical time for phase change is longer at

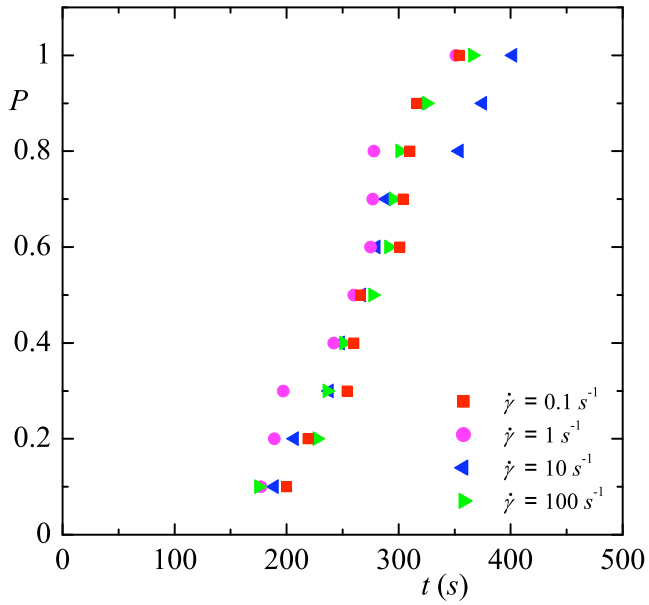

(a) Critical time probability as a function of time for T = -6.3 ± 0.6°C

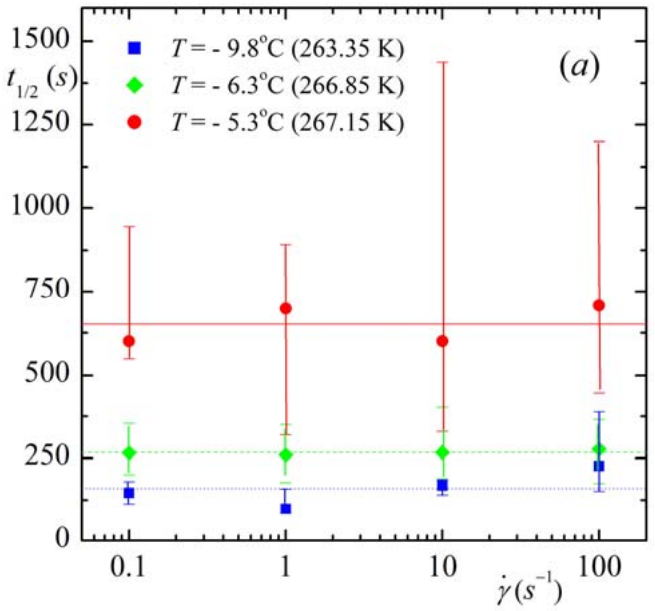

(b) $t_{1/2}$ versus shear rate ($\dot{\gamma}$)

Figure 4.15: Hydrate-forming 40% *w/o* emulsion.

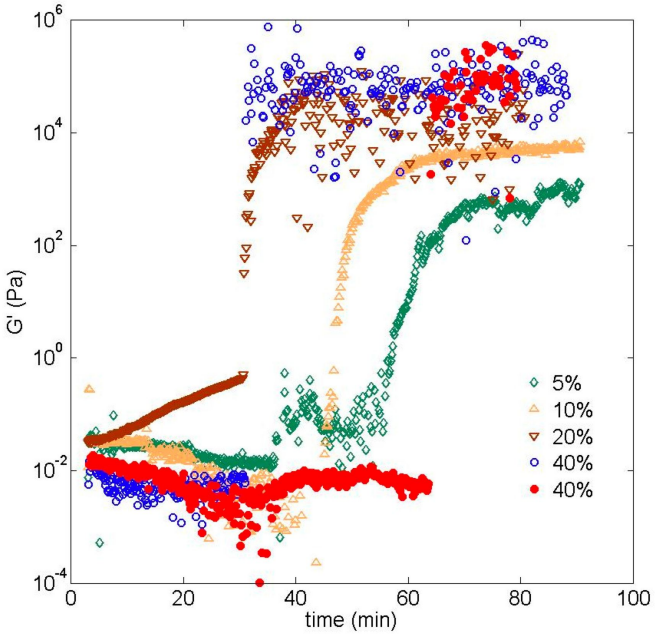

(a) Storage modulus (G') versus time

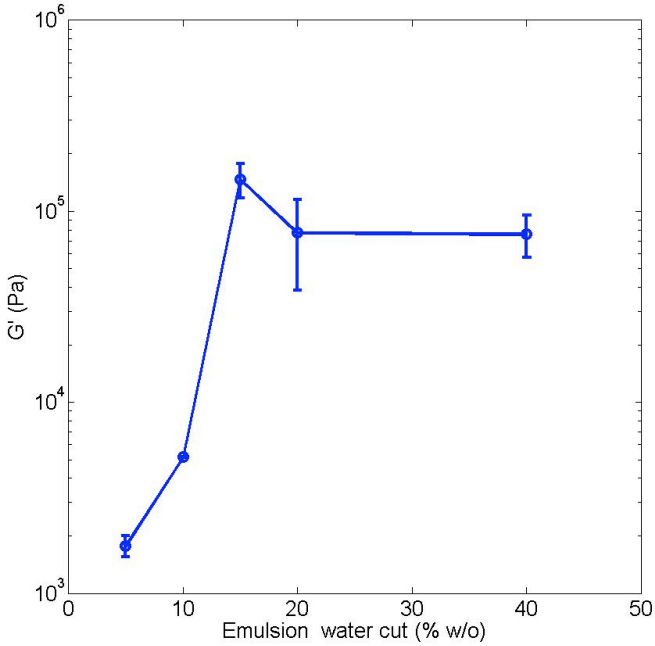

(b) Storage modulus of hydrate slurry versus parent w/o emulsion water cut

Figure 4.16: Linear viscoelastic rheology of variable water cut w/o emulsions. T = -10°C except in part (a) where filled circles for 40% emulsion are obtained at -7°C, stress = 0.05 Pa and frequency = 1 Hz.

-7°C as compared to -10°C as seen in Figure 4.16(a), again qualitatively similar to the results shown in Figure 4.15(b).

The increase in G' becomes gradual at lower water cuts as compared to an instantaneous jump observed in case of 40% *w/o* emulsion , as shown in Figure 4.16(a) and the growth time, defined as the amount of time from the onset of phase change to achieve a steady G' value, increases with decreasing water cut. Recall that this is a reactive crystallization process and once the nucleation occurs, the rate of hydrate growth will depend on how fast hydrate particles and water drops interact with each other, see mechanism shown in Figure 4.7. For higher water cut emulsions, water drops are in close proximity with each another and hairy and porous hydrate growth can quickly propagate through the system resulting in the observed instantaneous jump for the 40% emulsion. For lower water cuts, the average distance between water drops increases and thus additional time is necessary to complete the process of hydrate formation and agglomeration. The final G' value of the hydrate slurry is found to increase with the emulsion water cut and from limited tests done so far, it appears that 10% water volume fraction is close to the critical water cut above which the system tends to show a complete plugging behavior under the applied oscillatory stress.

4.4 Conclusion

The rheological properties of cyclopentane hydrate-forming emulsions over a wide range of water volume fractions are presented. The hydrate slurry viscosity increases with water cut in case of oil-continuous emulsions and decreases with water cut for water-continuous emulsions. The high dispersed phase fraction emulsions, approximately 30% to 60% water volume fraction, showed a rapid viscosity increase

upon hydrate formation and lead to rheometer plugging.

The observed increase in the emulsion mechanical properties after hydrate formation cannot be explained just from the solidification of internal phase drops. In case of water-in-oil emulsions, it is postulated that the hairy and porous hydrate growth along with enhanced agglomeration due to liquid water films around the hydrophilic hydrate surface serving as liquid bridges lead to development of porosity in the system. The resulting effective volume fraction in this case can be much greater than the initial emulsion water cut. The observed dependence on the degree of sub-cooling, with lower slurry viscosity obtained at higher sub-cooling, and the possible anti-agglomerant like effect of high Span 80 loadings, support our proposed mechanism. Further experimentation with other surfactants / anti-agglomerants, with an ability to significantly modify the water wetting tendency of hydrate surface, is proposed to gain more insight into the role of water capillary bridges in the hydrate plug formation.

Chapter 5

Flow Rheometer

5.1 Development

In multiphase systems, microstructure of the material govern its rheological properties to a great extent. Although techniques such as small angle light scattering are being implemented in a new generation of standard rheometers, their use becomes limited at operating conditions required for the hydrate formation. This led us to a develop a tool, *flow rheometer* designed with the capability of measurement of mechanical properties coupled with morphological characteristics through direct visualization. Even though used primarily for hydrate-forming emulsions, flow rheometer applications can be extended to other multiphase systems. It has been used to characterize waxy oils and shear thickening in worm-like micellar solutions (cetyl trimethyl ammonium bromide and sodium salicylate in water), but the results are not reported here due to lack of correspondence to the main theme of this thesis.

5.1.1 Apparatus

Figure 5.1 shows a flow rheometer schematic along with an actual experimental setup. The usual test section is a glass tube with 5 mm internal diameter and

Parts	Specifications
Test section	Glass tube, ID 5 mm, OD 9 mm, length 70 cm
Piston	Gas-tight glass syringe (Hamilton Co.)
Driving system	Translating stage, M403-6PD (PI- www.pi.ws)
Pressure transducers	± 1, 5 psi (Omega)
Thermocouples	T type
Coolant	Ethylene glycol + water
Signal conditioning block	SC-2345 (National Instruments)
Data acquisition	LabVIEW 7.1

Table 5.1: Technical specifications, Flow rheometer.

2 mm wall thickness, and can be easily replaced with variable diameter tubes. A gas-tight glass syringe coupled with a linear translating stage is used to drive an oscillatory pressure-driven flow inside the test section. The other end of the test section is connected to a reservoir; the reservoir diameter is 10 cm. A pressure transducer and thermocouples are in place for the differential pressure drop and temperature measurements. The temperature is controlled with an external cooling bath recirculating the coolant (ethylene glycol and water mixture) through a transparent rectangular acrylic chamber surrounding the test section. The entire setup is fixed on a vertical rail; as shown in Figure 5.1. The imaging and light transmission system are mounted on a parallel rail using mobile connectors facilitating their vertical movement along the test section. A data acquisition board (SC-2345) from National Instruments and LabVIEW are used for temperature and pressure acquisition. Table 5.1 provides technical specifications of various components of the flow rheometer.

5.1.2 Operating mode

A reciprocating motion of the piston (glass syringe) produces an oscillatory flow inside the test section. Figure 5.2 shows a typical differential pressure transducer

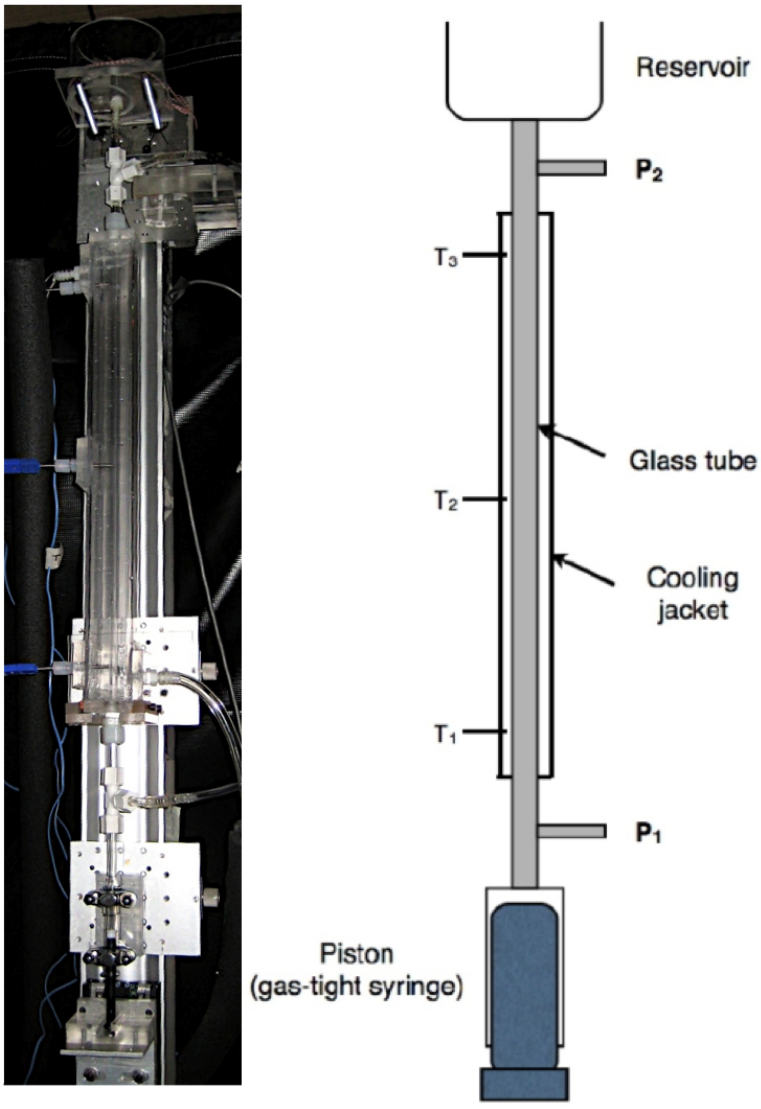

Figure 5.1: Experimental set up and schematic of Flow Rheometer

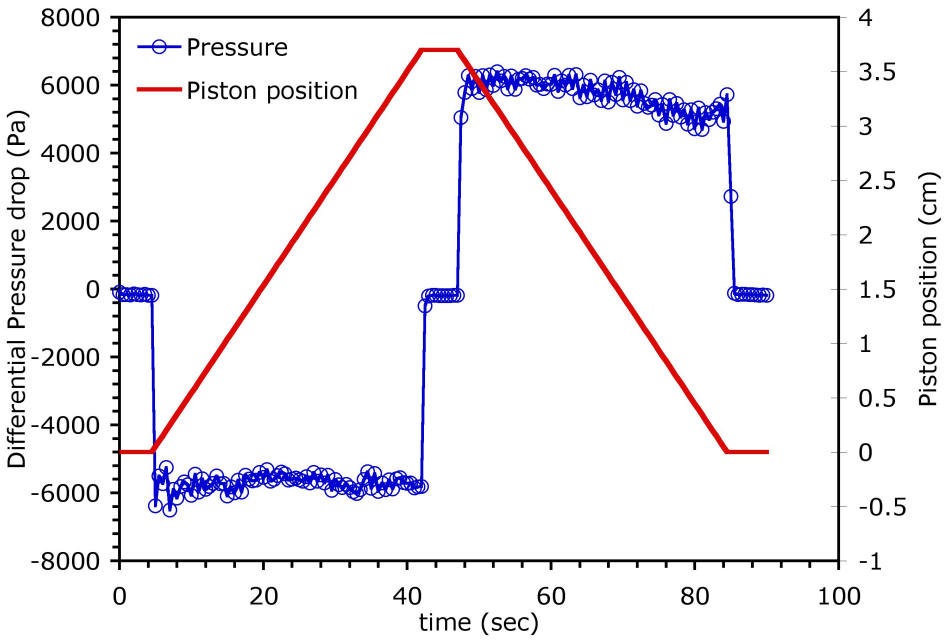

Figure 5.2: Differential transducer response versus piston position. (system: mineral oil)

response. The transducer records zero in the rest position (*i.e.* no flow) and the polarity of the transducer response depends on the direction of the flow. For the set-up shown in Figure 5.1, the upward motion of piston records negative differential pressure drop and the downward motion provides positive value. For any type of fluid, the wall shear stress τ_w is given as

$$\tau_w = \frac{\Delta P D}{4L}, \tag{5.1}$$

where D is a pipe diameter, L is length and ΔP is the differential pressure drop recorded by the pressure transducer.

5.2 Results and discussion

5.2.1 Newtonian fluid characterization

A light mineral oil is used as a Newtonian fluid for the validation tests. Figure 5.3(a) shows the measured differential pressure drop as a function of mean test section velocity at $T = 25^{o}$C.

If we assume a simple Poiseuille flow inside the tube, the Hagen-Poiseuille equation relates ΔP to mean pipe velocity U:

$$\Delta P = \frac{32\mu U L}{D^2}. \tag{5.2}$$

The light mineral oil viscosity obtained from the flow rheometer is 51 cP as compared to 46 cP obtained from a standard AR 2000 rheometer equipped with a cone and plate geometry, 40 mm diameter and 2^o of truncation angle.

Figure 5.3(b) compares the light mineral oil viscosity data at different temperatures. It can be seen that the mineral oil viscosity follows an Arrhenius dependence,

$$\mu(T) = A \exp[E/RT], \tag{5.3}$$

where T is in K and $R = 8.314$ J mol^{-1} K^{-1} is the gas constant. For the mineral oil, $A = 1.7 \times 10^{-10}$ Pa.s and $E = 47702.4$ J mol^{-1} for $263.16 \leq T \leq 298.16$ K. It is observed that at the lower end of this temperature range, flow rheometer records lower viscosities. This is believed to be due to the temperature variation across the length inside the cooling jacket as it cannot reach the thermal accuracy and uniformity of the Peltier system operating on a small gap (45 μm) in cone and plate geometry of AR 2000 rheometer.

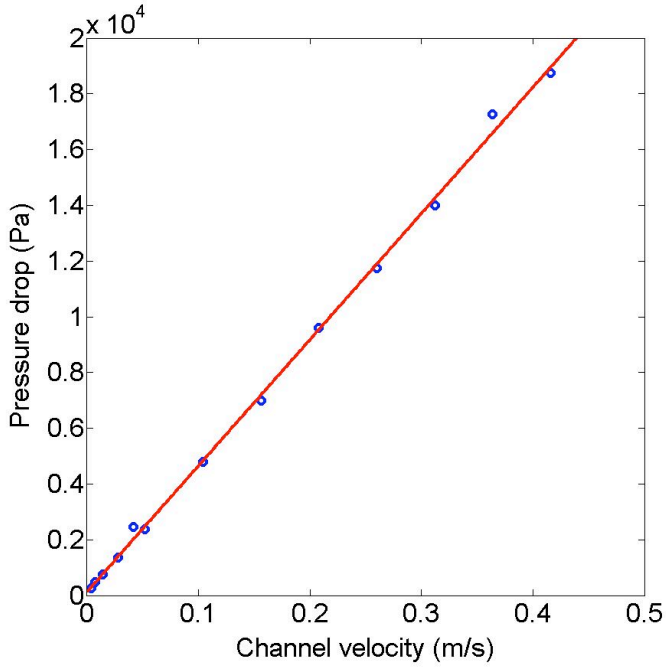

(a) Newtonian behavior, ΔP *vs* channel velocity at 25°C.

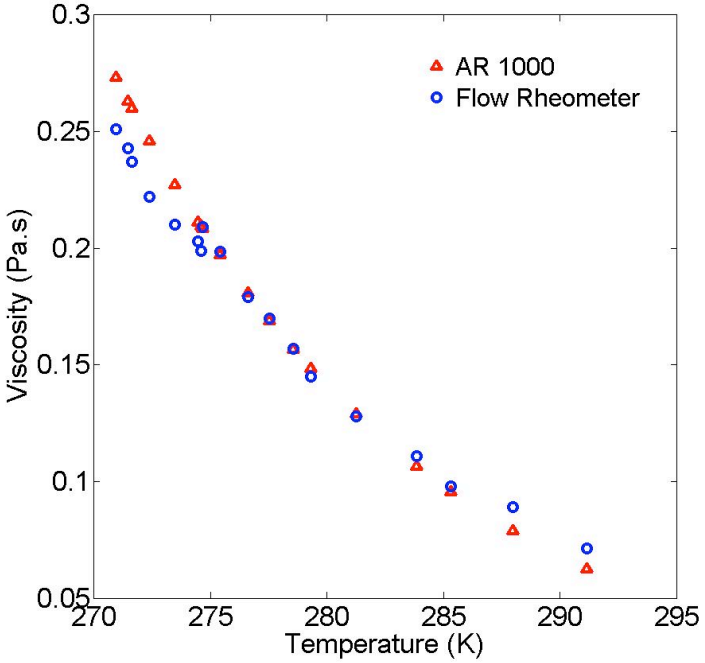

(b) Flow rheometer and AR 1000 comparison, Arrhenius behavior.

Figure 5.3: Light mineral oil properties

5.2.2 Waxy oil characterization

Precipitation of long chain paraffinic components, generally termed as wax, from crude oil is also a key flow assurance issue in the petroleum industry. Below a particular temperature, known as wax appearance temperature (WAT), waxy components start to precipitate out of the oil phase and deposit on the pipeline wall, thus reducing the available area for the flow. We present here characterization of such a wax-forming oil to demonstrate the flow rheometer capabilities by comparing the results against a standard rheometer.

The oil phase is a mixture of Halocarbon 700 oil (H700) and n-decane, in the ratio of 80:20 by volume. H700 is a high molecular weight polymer of chlorotrifluoroethylene (PCTFE). The WAT of this mixture, as obtained from μDSC, is $\approx$ -4°C.

Figure 5.4 shows the wall shear stress as a function of temperature at a fixed wall shear rate of 10 s^{-1}. The stress increases initially due to temperature dependence and then a change in the slope of stress response is observed with the precipitation of wax crystals at around -3°C. The discrepancy in the onset temperature from rheology and WAT obtained from DSC can be associated with the temperature variation across the test section length; the reported value is an average of three thermocouple readings. Also, the data in μDSC is obtained during a controlled temperature decrease at 1°C/min while the data in flow rheometer is obtained from a constant hold at each temperature for five minutes. During the increasing temperature cycle, a hysteresis is observed in the shear stress response. A similar hysteresis behavior is also observed in a standard AR 2000 rheometer using a concentric cylinder geometry (28 mm rotor diameter and 1 mm gap). The purpose of these tests is not a detailed characterization of the waxy oil but to test the limits and confidence level in the flow rheometer.

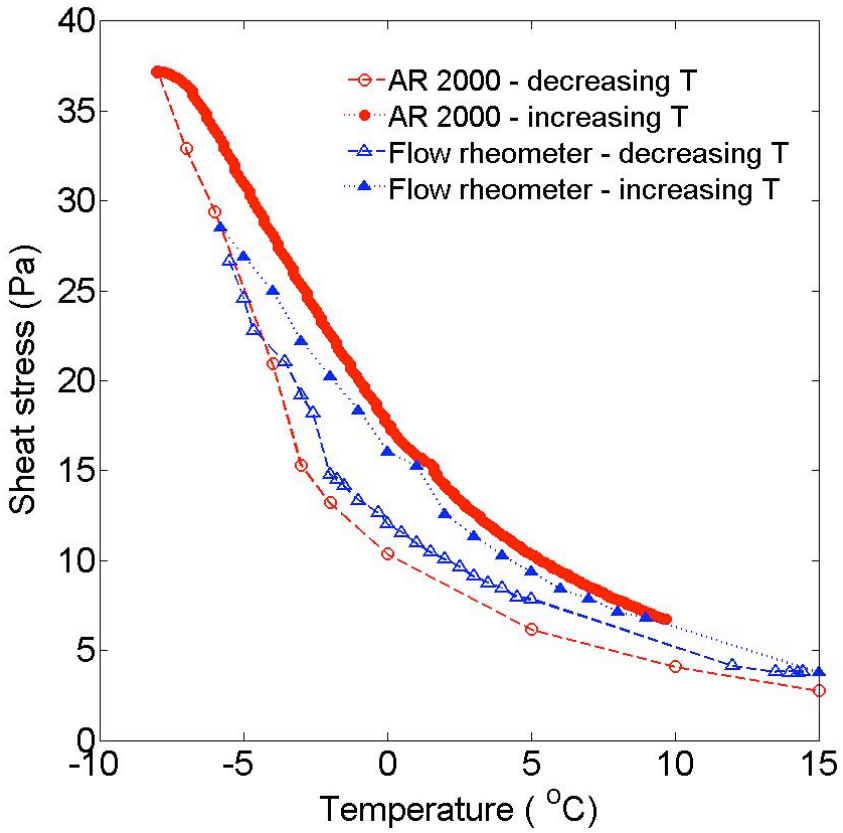

Figure 5.4: Hysteresis behavior associated with wax-forming oil mixture, H700 + *n*-decane, 80:20 by volume. Wall shear rate in flow rheometer and shear rate in AR 2000 = 10 s^{-1}.

5.2.3 Hydrate-forming water-in-oil emulsion

Figure 5.5 shows a stress response (calculated from the measured pressure drop) as a function of temperature for a 40% *w/o* hydrate-forming emulsion. The temperature is decreased from 10°C to -6.5°C and then increased to 10°C. The temperature ramp rate depends on the cooling bath pump capacity but an idea about the rate of temperature decrease can be obtained from Figure 5.5. The wall shear stress increases slightly as the temperature decreases due to temperature dependence of the emulsion. Hydrate formation is detected from a sudden jump in the pressure-drop observed at around -6.25°C which eventually led to plug formation inside the test section. This stress behavior is similar to the rapid viscosification observed for the same 40% *w/o* emulsion in standard rheometer experiments.

Figure 5.6 shows the emulsion images before and after hydrate formation. A uniform, homogeneous emulsion develops into a segregated, heterogeneous structure after hydrate formation and scatters more light. It appears that solidified water drops / hydrate balls develop an interlocking structure and also have contacts with the glass wall. It is observed that the network of hydrate balls is porous in nature and heterogeneous along the test section length, as some oil compartments are seen trapped in the hydrate plug. As the temperature approaches the hydrate equilibrium point of 5°C during the heating ramp, the wall contacts start loosening and close to 6°C, the applied flow is enough to break the wall contacts and destroy the network. The resulting suspension of solid hydrate particles showed a large pressure drop, $O(10^4)$ Pa. After a complete dissociation, the system returns to its liquid state having a much different appearance than the original emulsion. It appears that the emulsion is destabilized as a few large water drops are seen floating around.

To gain more insight into the hydrate plug network, the 40% *w/o* emulsion is

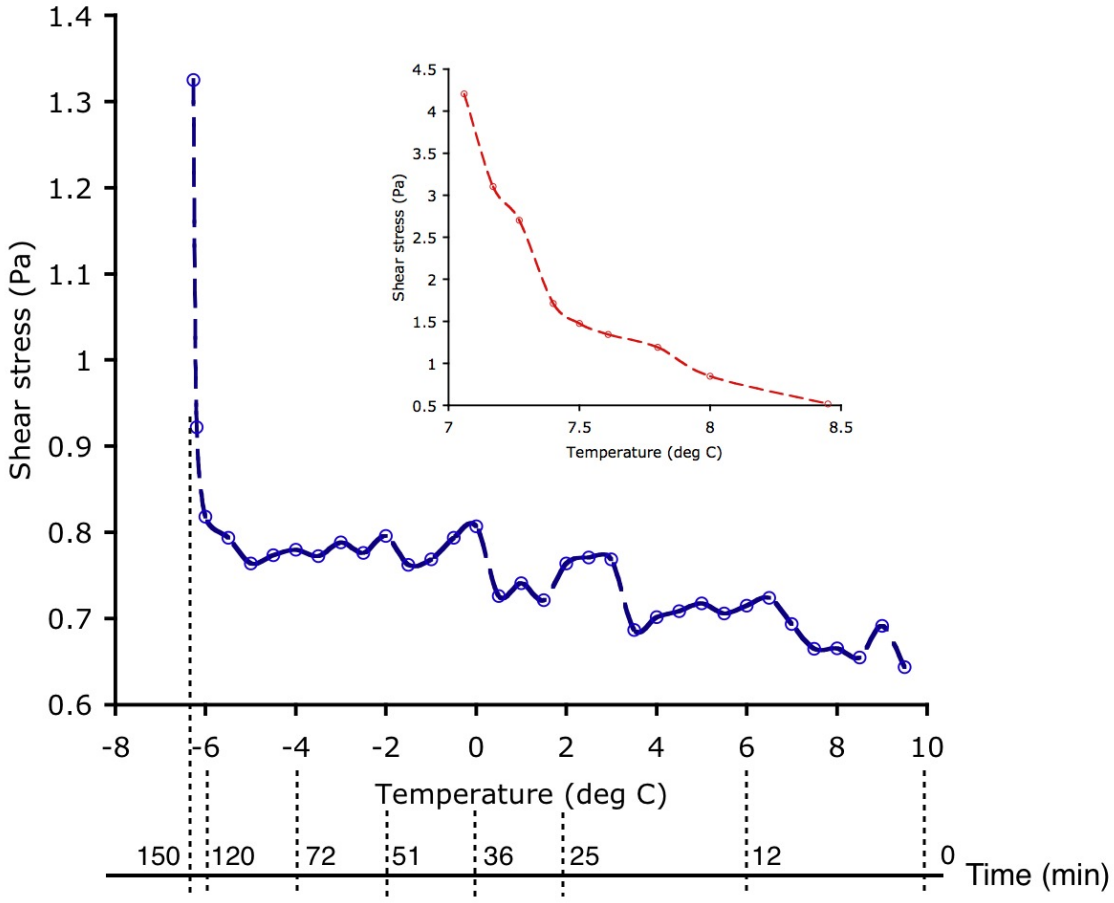

Figure 5.5: Stress response for 40% *w/o* emulsion, blue: decreasing temperature and red: increasing temperature, 5 mm inner diameter glass tube, velocity: ± 1.5 cm/s with amplitude: ± 4.75 cm

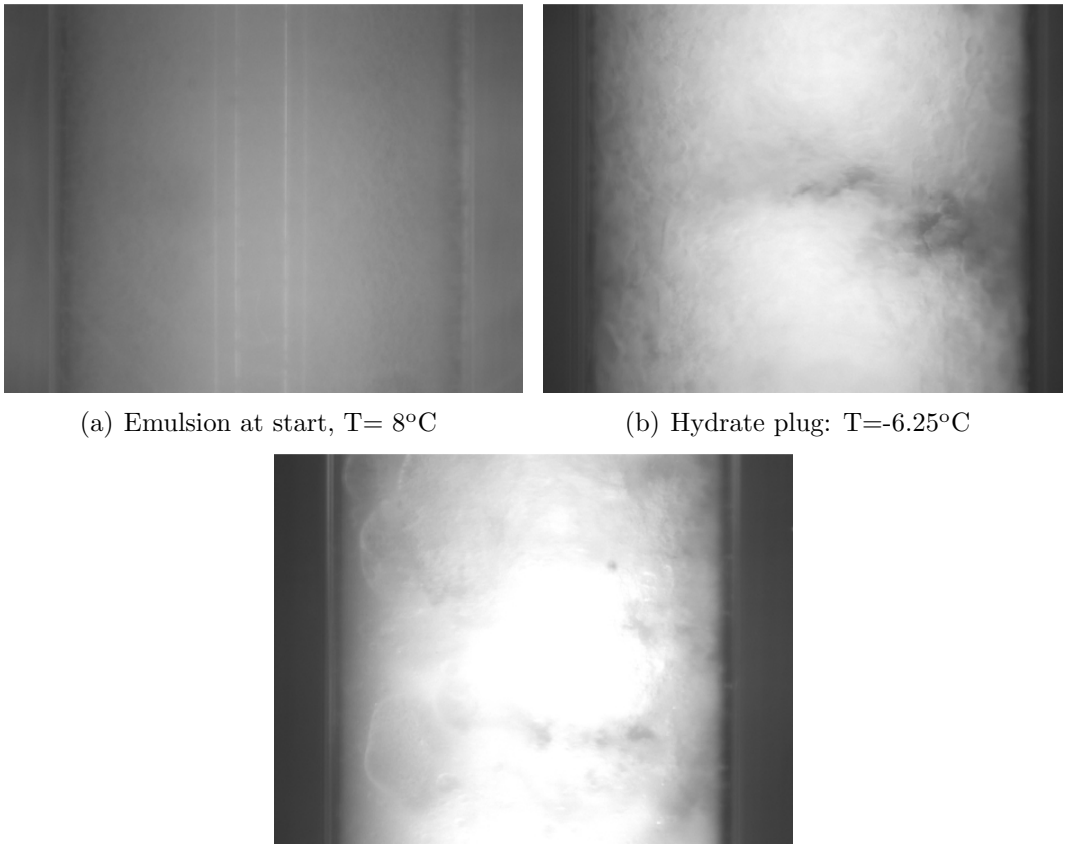

(a) Emulsion at start, T= 8°C

(b) Hydrate plug: T=-6.25°C

(c) Destabilized emulsion: T = 9°C

Figure 5.6: State of the emulsion corresponding to stress values from Figure 5.5, tube diameter is 5 mm.

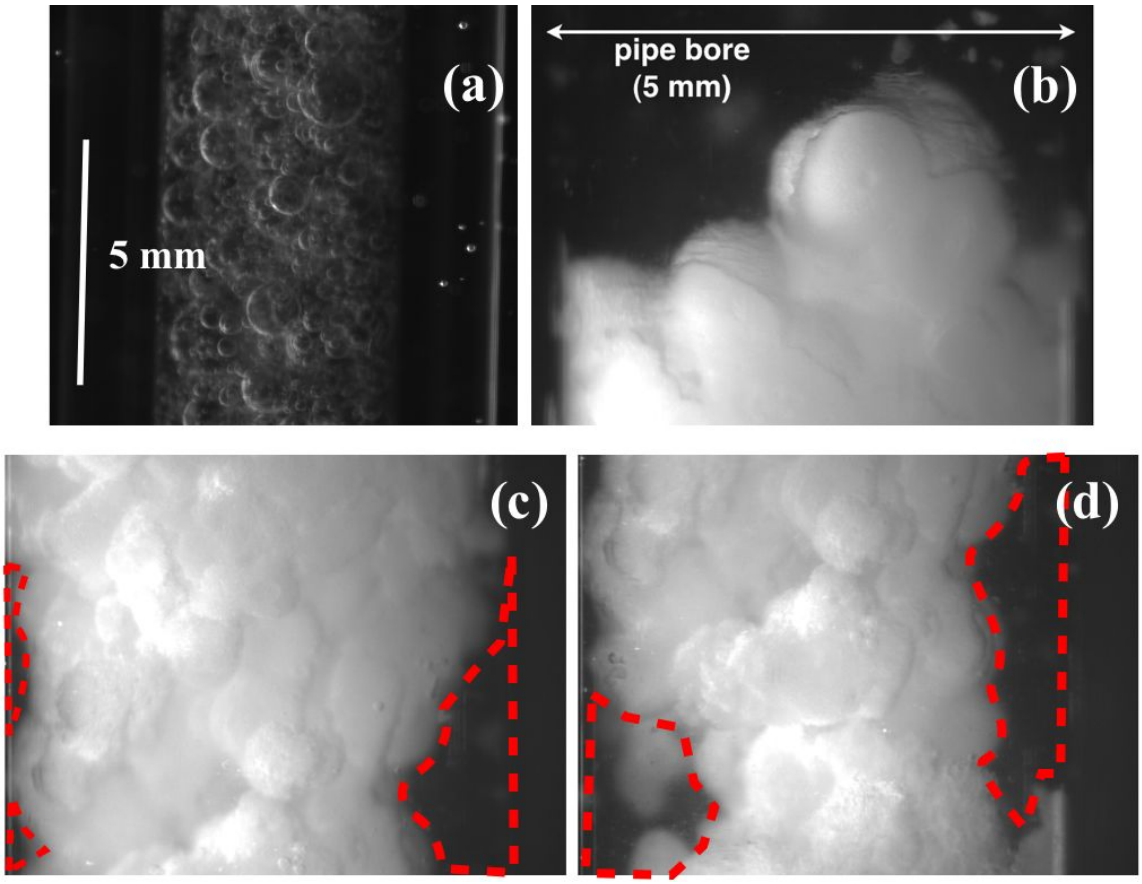

Figure 5.7: (a) modified 40% *w/o* emulsion, (b) - (d) cyclopentane hydrate plug images at different locations across the test section length, $T = 3.5^{o}$C, regions marked in dotted red lines indicate the open gaps in the hydrate plug filled with oil.

modified by reducing the Span 80 concentration to 0.05% (v/v) and emulsifying at a lower intensity, 500 rpm for 5 minutes. Figure 5.7(a) shows a picture of the modified emulsion with millimeter size water drops as compared to O(10) microns. The modified emulsion is subjected to the same temperature protocol as shown in Figure 5.5. After hydrate formation at -6°C, the temperature is increased to 3°C and held constant. Figure 5.7 shows the plug images at three different locations along the test section.

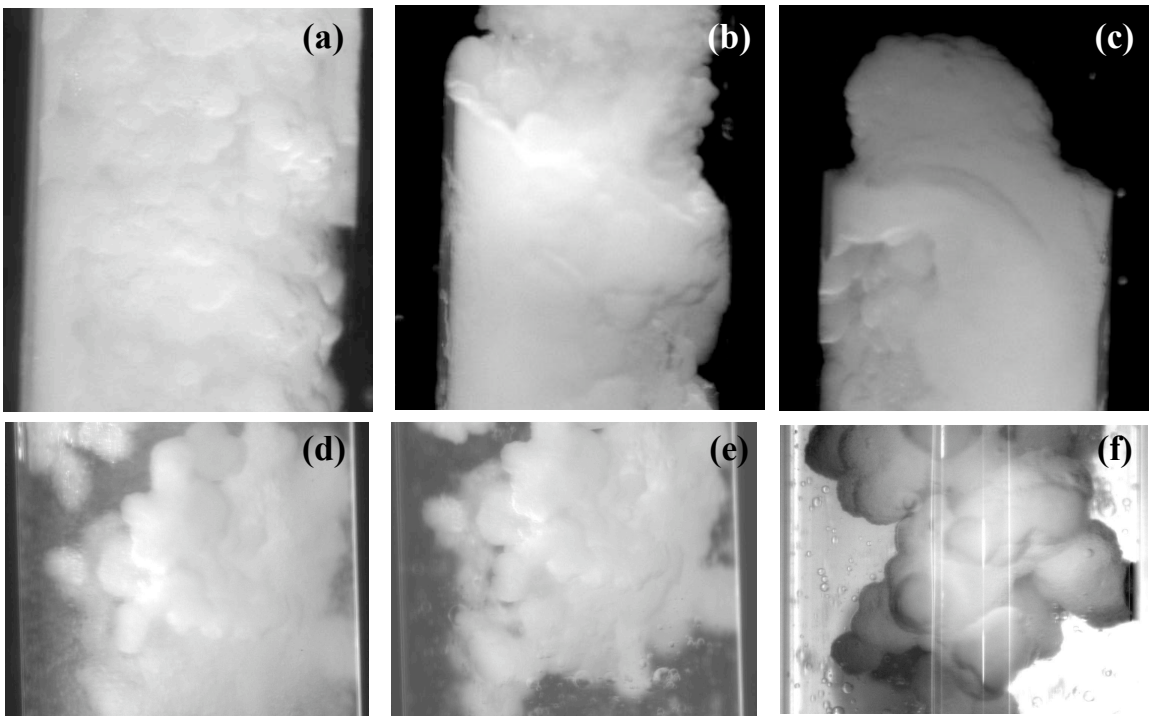

Figure 5.8: Cyclopentane hydrate plug images at different locations of test section: 5 mm ID glass tube. 40% *w/o* hydrate-forming emulsion.

The hydrate plug appears to be a complex network of hydrate balls having cotton-like appearance. Recall that, similar hairy and whitish hydrate morphology was observed in single-drop experiments. The heterogeneous structure with open gaps filled with the oil phase can be seen across the cross-section; see Figure 5.7. The observed hydrate plug characteristics strongly support the proposed mechanism for the viscosity increase of oil-continuous emulsion that the hairy and porous hydrate growth and enhanced agglomeration due to liquid water films around the hydrophilic hydrate surface serving as liquid bridges are mainly responsible for the porosity development. Figure 5.8 shows additional images of cyclopentane hydrate plugs.

5.3 Summary

Ability to provide a coupled information about the mechanical properties and microstructural characteristics of the material, makes the flow rheometer a proper platform to gain useful knowledge for the modeling of such a complex reactive crystallization process of hydrate formation. From a more practical perspective, development of a high-pressure version of the flow rheometer for gas hydrate system is in progress. Figure 5.9 shows a schematic and a prototype model. Test section is a 2 x 12 x 180 mm rectangular channel machined out of aluminum (Al 6061). It is surrounded by an in-built cooling jacket. A high-pressure dual piston (600 ml, 7500 psi maximum) with a linear translating stage is a driving assembly, connected to the test section through ABS plastic transition pieces. The test section includes a 6 mm long quartz window for direct visualization. The prototype has been tested for pressures up to 150 psi.

Acknowledgement

We greatly appreciate the efforts of G. Abdullah, F. Baradji, M. Bruce and R. Ferguson (Department of Mechanical Engineering, City College of New York) in the design and machining of the high-pressure flow rheometer.

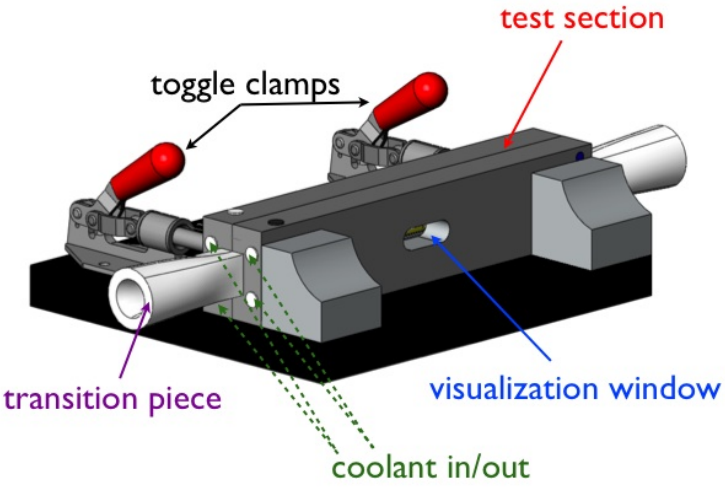

(a) Schematic

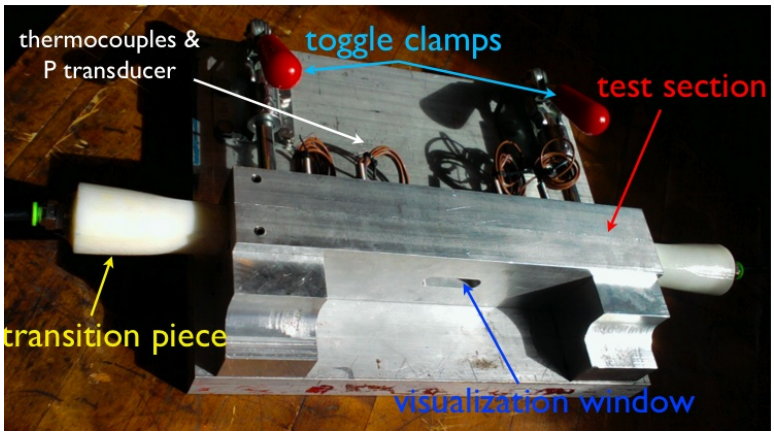

(b) Experimental setup

Figure 5.9: A high-pressure version of flow rheometer.

Appendix A: Supplementary information on hydrate crystal morphology

Effect of Span 80

Faceted hydrate shell - Span 80 interaction:

Figure A.1(a) shows a faceted hydrate shell formed at a single water drop placed in cyclopentane, without any surfactant. As reported before, a thin faceted crust is formed around the water drop; this morphology arises from the growing together of numerous small leaf-like crystallites. Deformation of the shell away from a spherical shape and the polycrystalline structure are both evident in the magnified view shown in Figure A.1(b). Addition of Span 80 to the supernatant cyclopentane at levels far in excess of the 0.1% (v/v) level causes the shell to break allowing water and cyclopentane to contact. This leads to more formation of hydrates and hairy morphology as seen in Figure A.1(c). The faceted morphology seen without surfactant develops into a needle-covered, perhaps dendritic, structure after the external addition of surfactant into the oil phase, qualitatively very similar to the one observed in the presence of Span 80 at the time of nucleation. The reason for the influence of Span 80 on this shell breakage is not fully understood. Addition of Span 80 after formation of a shell appears to weaken junctions between surface crystals, and the internal

liquid pressure then leads to breakage. Water then flows out to contact the external cyclopentane, leading to rapid hydrate formation.

Effect of water drop size:

The behavior of conical crystal shape, immersion into the water phase and then radial growth leading to the hairy hydrate morphology observed in the presence of Span 80 ($C_{\mathrm{S80}} = 0.1\%\ v/v$) at the time of nucleation is found to be independent of the water drop size. In case of small water drops of 100 μm diameter, the conical crystals grow to the size of drop and immediately enter into radial growth. Figure A.2 shows the effect of water drop size on the time $t_{lateral}$ required for the lateral crystal growth of hydrates; *i.e.* the time required for the conical crystal growth and immersion into the water drop just before the radially outward flow of water occurs. The time for lateral growth $t_{lateral}$ is defined in Figure A.4 in the following section. It appears from the preliminary results that $t_{lateral}$ varies linearly with the water drop volume but further analysis is needed to understand the phenomenon.

Effect of water-soluble surfactants

Figure A.3 compares the cyclopentane hydrate morphology with and without Triton X-100 in the water drop suspended in cyclopentane containing Span 80. Triton X-100 is a non-ionic, water soluble surfactant with a HLB of 13.5 (as reported by Sigma-Aldrich). Although the final hydrate morphology appears qualitatively similar in both the cases, it appears that the hydrate morphology is more like a smooth mushy or cotton-like appearance as compared to the hairy structure observed in case of pure water drop. Figure A.4 shows the variation in linear dimensions of the water drop during the hydrate growth, made dimensionless by the initial ice ball

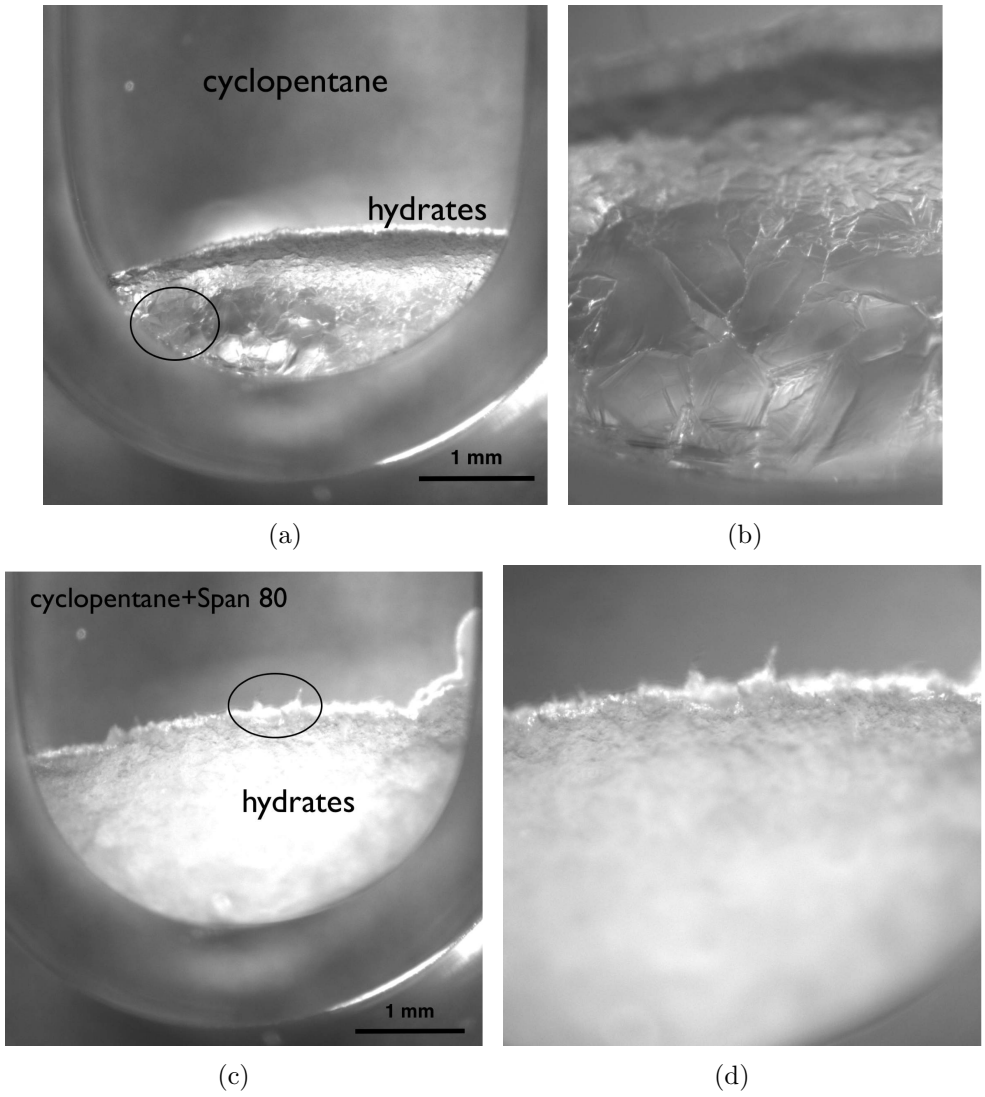

Figure A.1: (a) Pure cyclopentane hydrates - faceted, (b) Magnified view of the circled area in figure A.1(a), (c) After external addition of Span 80 to cyclopentane - dendritic, (d) Magnified view of the circled area in figure A.1(c); $T = 2.5^{o}$C (magnified views are not exactly to the scale of circled parts of original image).

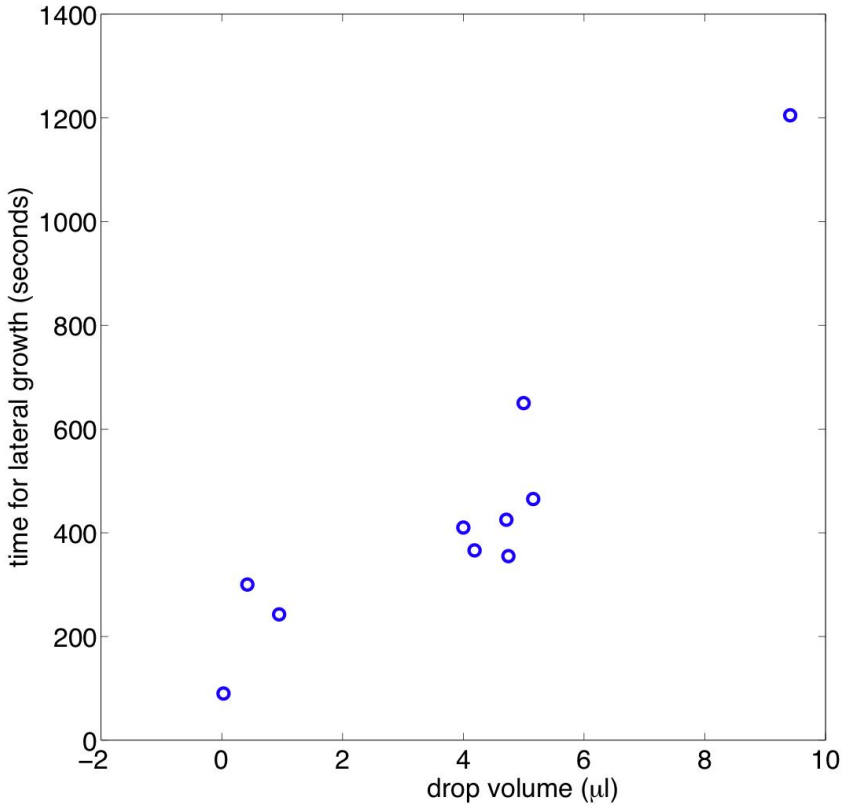

Figure A.2: Effect of water drop volume on the time required for the lateral surface growth (just before entering into radial hairy growth), $C_{S80} = 0.1\%$ (v/v) in cyclopentane.

dimensions. It remains close to unity during the initial nucleation and lateral growth phase followed by a rapid increase related to radial growth developing into the hairy / mushy structure. For the same size water drops (4 μl), the water drop containing Triton X-100 enters the radial growth comparatively earlier, *i.e.* t_{lateral} (as defined in Figure A.4) is smaller and develops rapidly into the mushy morphology.

Göbel et al. [88] have studied the water-cyclohexane interfacial tension as a function of Triton X-100 concentration in cyclohexane. We assume that the interfacial properties will not change drastically for cyclopentane as compared to cyclohexane. Göbel et al. have reported a CMC value of 2.8×10^{-4} M $\approx 0.018\%$ by weight, and thus the concentration of 0.1% used in our study is expected to be above the CMC. The reported water-cyclohexane interfacial tension and surface concentration of Triton X-100 at CMC are $\gamma_{\text{CMC}} = 7$ mN/m and $\Gamma_{\infty} = 1.45 \times 10^{-6}$ mol/m^2; recall the corresponding values for Span 80 are $\gamma_{\text{CMC}} = 0.8$ mN/m and $\Gamma_{\infty} = 3.69 \times 10^{-6}$ mol/m^2. Looking at the interfacial activity and surface concentration of both the Span 80 and Triton X-100, our conjecture is that combined surfactant layers at the water-cyclopentae interface lead to rapid surfactant crowding at the interface during the lateral crystal growth, expedite the crystal merging back behavior and thus reduce the time before the radial growth sets in, as seen in Figure A.4.

Effect of anti-agglomerants

As discussed in the Chapter 3, the presence of a commercially available anti-agglomerant (quaternary ammonium salt) in water completely inhibits the hairy hydrate growth even at high Span 80 concentrations and leads to a faceted shell type morphology. It is also observed that the presence of anti-agglomerants (AA) restricts the lateral crystal growth leading to smaller hydrate facets as shown Figure

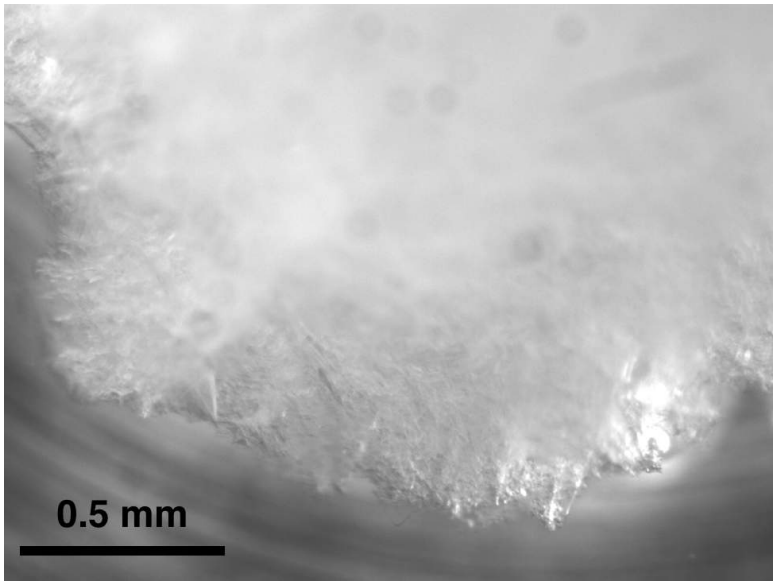

(a)

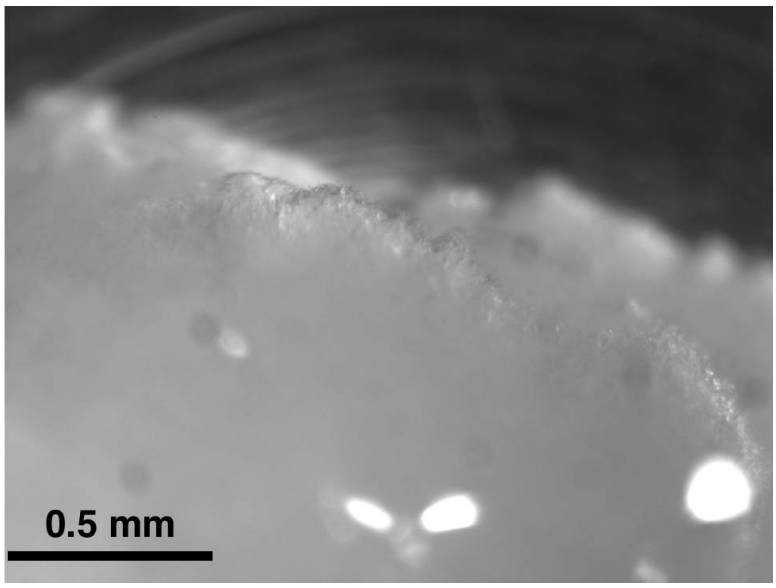

(b)

Figure A.3: Cyclopentane hydrate morphology, $C_{S80} = 0.1\%$ (v/v) in both the cases, $T = 0.2^{o}$C, water drop containing - (a) Hairy, no Triton X-100, (b) Muhsy / cotton-like, Triton X-100 (0.1% by wt)

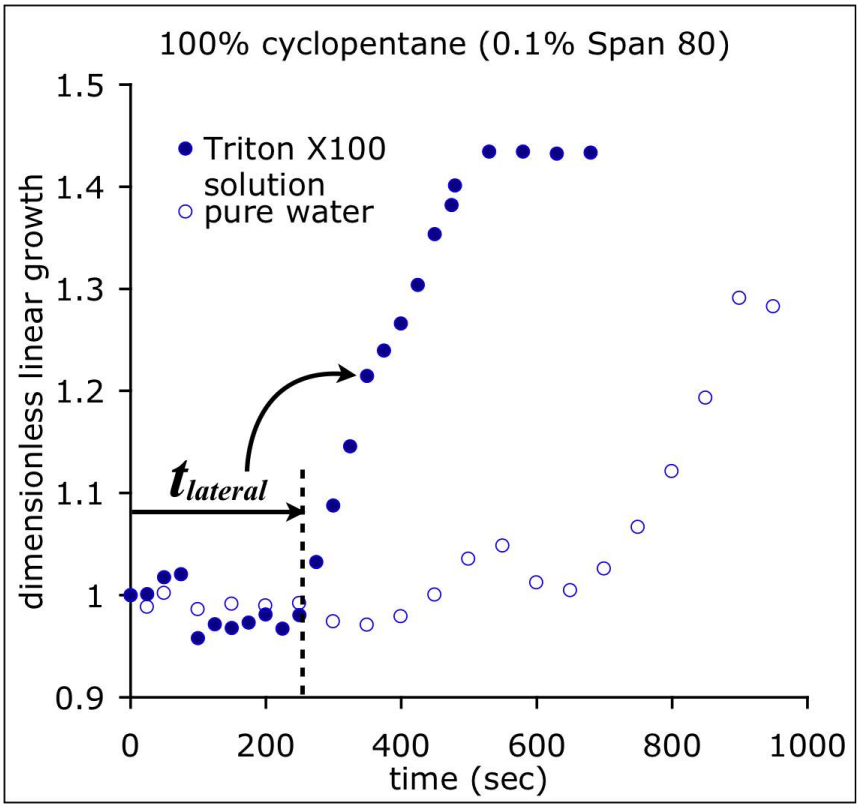

Figure A.4: Effect of Triton X-100 on the linear dimension of hydrate ball during hydrate growth, $C_{S80} = 0.1\%$ (v/v) in both the cases, $T = 0.2^{o}$C. Open circles: pure water drop, solid circles: water drop containing Triton X-100 (0.1% by wt). Linear dimensions of water drop are made dimensionless by the initial ice ball size (only x and y dimensions from the top view are considered).

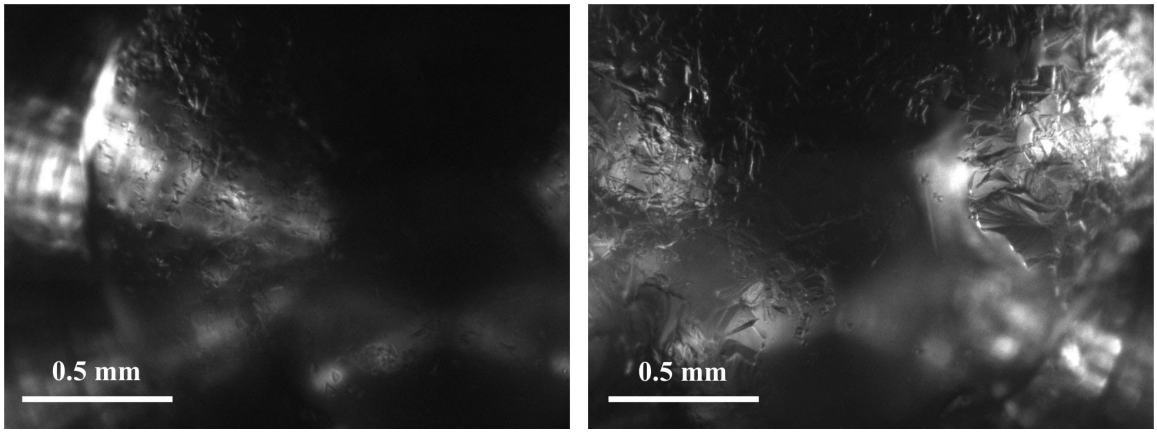

Figure A.5: Effect of anti-agglomerant (AA) on the lateral crystal growth of cyclopentane hydrates, 4 μl water drop (1% AA by wt) in cyclopentane, $C_{S80} = 0.1\%$ (v/v), $T = 0.2^{o}$C.

A.5.

Figure A.6 shows variation of AA effectiveness with its concentration in the water drop. The AA effectiveness is defined as the amount of sub-cooling up to which it is effective in inhibiting the hairy / mushy hydrate growth and keeping the morphology to a faceted shell. For example, for 1% by weight AA in water, the reported effectiveness is 15°C. This suggest that the shell morphology is obtained up to a temperature $T_{\text{hold}} = (T_{\text{eq}}$ - 15) = -8°C; recall that T_{eq} of cyclopentane hydrate = 7°C. At -9°C the radial growth sets in leading to the observed hairy morphology. It can be seen that AA effectiveness depends non-linearly over its concentration. Reported data is preliminary in nature and further repetitions are required to define a distinct line separating the shell and hairy morphology zones.

As reported by McCulfor et al. [87], Arquad 2HT-75 (an oil-soluble quaternary ammonium salt) may be a better anti-agglomerant based on their observation of increased contact angle of a water drop on a glass surface in mineral oil. A similar single-drop experiment with a pure water drop suspended in cyclopentane containing Arquad 2-HT 75 at 0.1% by wt concentration is performed; Figure A.7 shows a

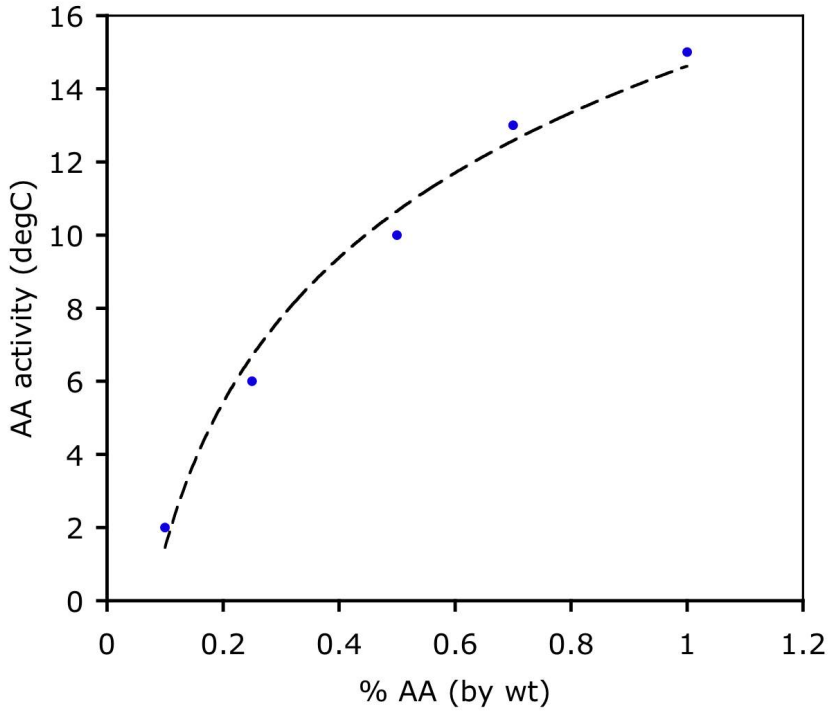

Figure A.6: AA effectiveness as a function of concentration in the water phase, dotted line separating the mushy and shell morphology zones is just a guide to an eye.

sequence images during the hydrate growth. It is observed that hydrate crystals during the lateral surface growth are smaller in size and are faceted as compared to conical crystals observed in the presence of Span 80. The faceted shell formation is observed before the shell breakage and an outward flow of water in a boiling fashion led to the observed smooth and slushy morphology.

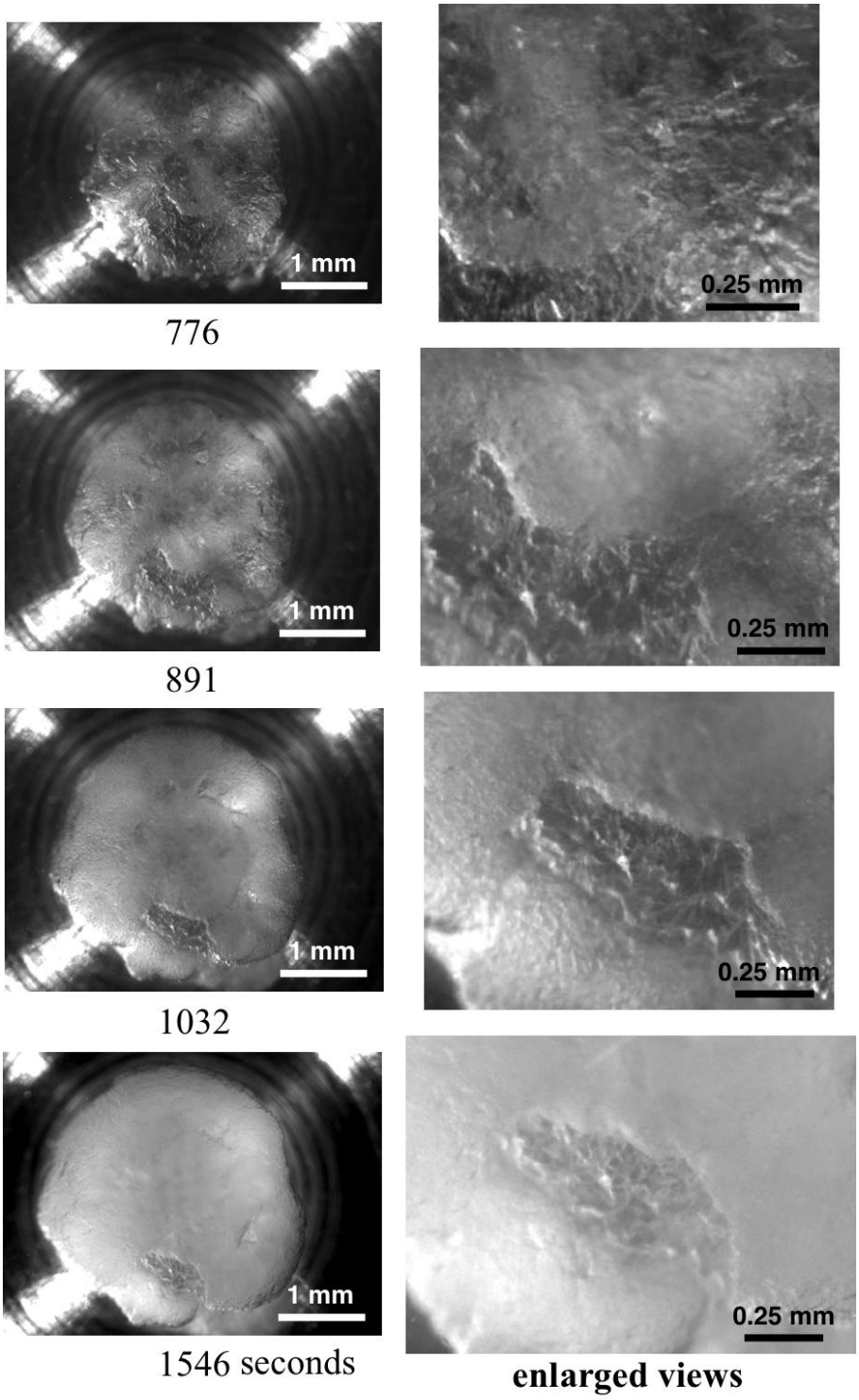

Figure A.7: Effect of Arquad 2-HT on cyclopentane hydrate morphology: water drop in cyclopentane, $C_{\text{Arquad}} = 0.1\%$ by wt, $T = 0.2^{\text{o}}\text{C}$, time is measured from onset of ice melting. Enlarged views are shown on the second column.

Appendix B: Hydrate formation and dissociation effects: Calorimetric analysis

It is of interest to determine how the hydrate formation and dissociation process may affect the stability of an emulsion. It may cause both agglomeration and development of heterogeneity in the emulsion, as well as coalescence of water drops during hydrate dissociation. The technique of calorimetry is applied to study the effect of repetitive hydrate formation and dissociation on the emulsion stability. The same temperature protocol as in the kinetic studies, *i.e.* decreasing the temperature from 20°C to -45°C and then heating to 20°C at 1°C/min in each direction, is applied repeatedly to samples of the hydrate- and ice-forming emulsions. Refer Chapter 2 for a detailed information on the emulsion composition and stability. Each sample is maintained at 20°C for 20 minutes between cycles. Figure B.1 shows the endotherms for the melting of ice and dissociation of hydrates for five consecutive hydrate formation/dissociation cycles. No significant change is observed in the melting behavior for an ice system. However, for the hydrate-forming emulsion, a noticeable broadening of the ice melting endotherm is observed and this endotherm overlaps with the hydrate dissociation endotherm at each cycle.

The melting onset point, T_{onset}, defined as shown in Figure B.1(a) is always below the pure ice melting point (0°C) in ice-forming emulsions. This may be due to

premelting or due to melting point depression caused by the presence of surfactant and oil. T_{onset} decreases with each cycle and one possibility is with each cycle, the water-oil interface gets more contaminated and thus leads to greater depression, as seen in Figure B.2(a). For the hydrate system, T_{onset} appears to be constant and always above the pure ice melting point, but in fact this is due to the fact that along with an endothermic ice melting there is an exothermic hydrate formation taking place. The two opposing heat flows cause the delay in showing the endothermic heat flow. Thus the reported T_{onset} is not a true ice melting point for the hydrate case.

The area under the hydrate dissociation endotherm provides the amount of water converted into hydrates. It can be seen that, from the second cycle onwards hydrate dissociation starts before ice melts completely. We make a simplifying approximation that this hydrate dissociation peak is symmetric and calculate the area under the right half of the curve and double it to get the amount of hydrates. This overlap of ice melting with hydrate dissociation curve (resulting from broadening of the ice melting endotherm) is not clearly understood. Our conjecture is that the agglomeration or interlocking of hydrates in the previous cycle may add an additional barrier to the transfer of heat for ice melting in the following cycle, thereby causing endotherm broadening with each cycle. This is supported by the hairy / dendritic morphology observed in the presence of Span 80, as reported in Chapter 3. Figure B.2(b) shows that conversion of water to hydrates decreases with each cycle. Error bars on the conversion in each cycle suggest that initial conversion is reproducible but the events happening in subsequent cycles are more variable, although the nature of the heat flow curves remains similar.

Broadening of ice melting endotherms and a corresponding drop in the conversion of water to hydrates suggests that the hydrate system flocculates to form agglomerates. This can be explained by the rapid water-wetting of the hairy hydrate surface

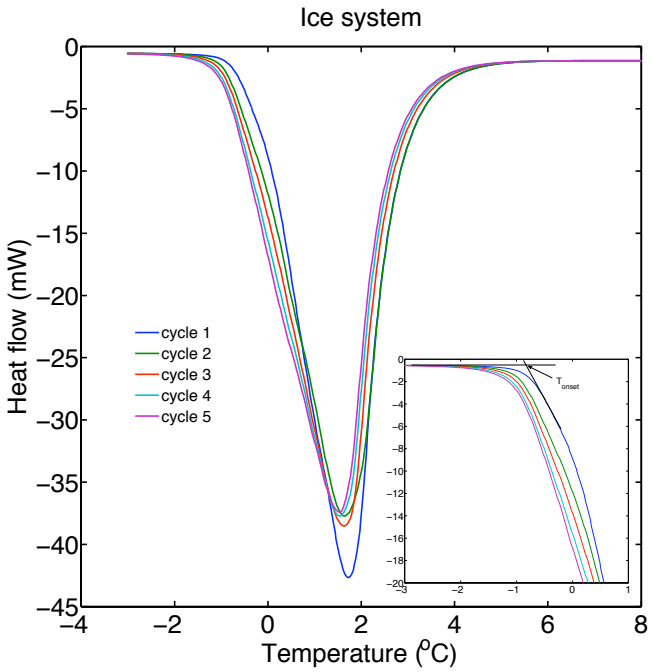

(a) ice forming emulsion

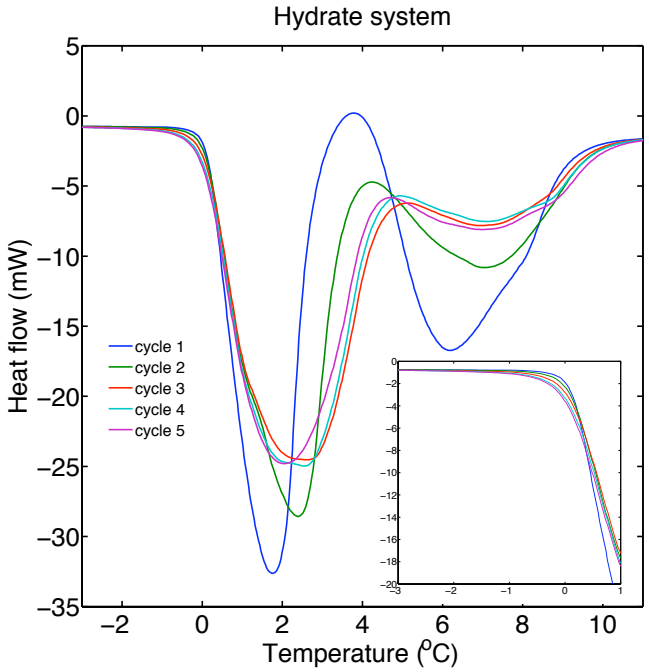

(b) hydrate forming emulsion

Figure B.1: Hydrate formation/dissociation effects on the endotherms, 40% *w/o* emulsion, (inset shows the initial part of an endotherm), heating rate = 1°C/min.

as observed in experiments with millimeter size water drops. We believe that the wetted liquid water films around the hydrate surface lead to interlocking structure and eventually cause the coalescence of water drops during dissociation. Recall that, a destabilized emulsion was observed after the dissociation of mushy or cotton-ball like hydrate plug in a flow rheometer. No such effect is observed in case of an ice-forming emulsion which suggests that droplets remain separated even after the ice formation and melting.

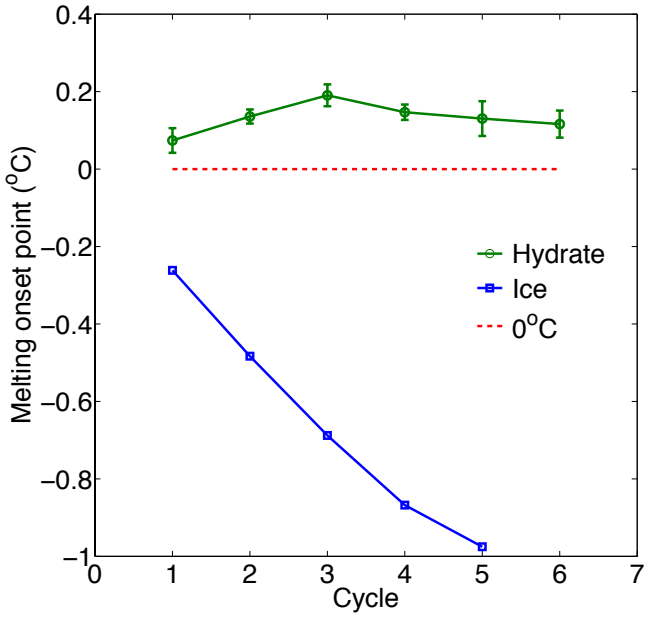

(a) Melting point onset

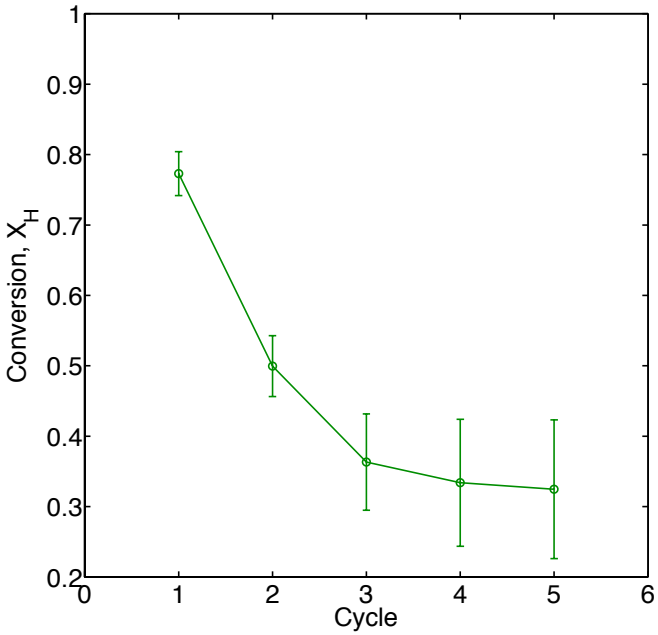

(b) Conversion of water to hydrates

Figure B.2: 40% *w/o* emulsion.

Bibliography

[1] N. Macintosh, Flow assurance still leading concern among producers, Offshore 60 (2000).

[2] E. G. Hammerschmidt, Formation of gas hydrates in natural gas transmission lines, Ind. Eng. Chem. 26 (1934) 851–855.

[3] E. D. Sloan, A changing hydrate paradigm – from apprehension to avoidance to risk management, Fluid Phase Equilibria 228-229 (2005) 67–74.

[4] S. Acevedo, G. Escobar, L. Gutiėrrez, H. Rivas, Isolation and characterization of natural surfactants from extra heavy crude oils, asphaltenes and maltenes. interpretation of their interfacial tensions – ph behaviour in terms of ion pair formation, Fuel 71 (1992) 619–623.

[5] M. A. Kelland, History of the development of low dosage hydrate inhibitors, Energy Fuels 20 (2006) 825–847.

[6] A. Lund, D. Lysne, R. G. Larson, K. W. Hjarbo, Method and system for transporting a flow of fluid hydrocarbons containing water, United States Patent 6774276 (2004).

[7] L. D. Talley, D. J. Turner, D. K. Priedeman, Method of generating a non-plugging hydrate slurry, United States Patent 20090078406 (2009).

[8] D. Turner, L. Talley, Hydrate inhibition via cold flow - no chemicals or insulation, in: Proceedings of the 6^{th} International Conference on Gas Hydrates (ICGH), 2008.

[9] E. D. Sloan, Gas hydrates: Review of physical/chemical properties, Energy Fuels 12 (1998) 191–196.

[10] P. Englezos, Clathrate hydrates, Ind. Eng. Chem. Res. 32 (1993) 1251–1274.

[11] A. V. Milkov, Global estimates of hydrate-bound gas in marine sediments: how much is really out there?, Earth-Science Reviews 66 (2004) 183–197.

[12] P. Englezos, J. D. Lee, Gas hydrates: a cleaner source of energy and opportunity for innovative technologies, Korean J. Chem. Eng. 22 (2005) 671–681.

[13] M. Darbouret, M. Cournil, J. M. Herri, Rheological study of TBAB hydrate slurries as secondary two-phase refrigerants, Int. J. Refrig. 28 (2005) 663–671.

[14] M. Nakajima, R. Ohmura, Y. H. Mori, Clathrate hydrate formation from cyclopentane-in-water emulsions, Ind. Eng. Chem. Res. 47 (2008) 8933–8939.

[15] J. S. Zhang, J. W. Lee, Equilibrium of hydrogen + cyclopentane and carbon dioxide + cyclopentane binary hydrates, J. Chem. Eng. Data 54 (2009) 659–661.

[16] E. D. Sloan, Clathrate hydrates: the other common solid water phase, Ind. Eng. Chem. Res. 39 (2000) 3123–3129.

[17] P. L. Parlouër, C. Dalmazzone, B. Herzhaft, L. Rousseau, Characterization of gas hydrates formation using a new high pressure micro-DSC, J. Therm. Anal. Calorim. 78 (2004) 165–172.

[18] Y. Zhang, P. G. Debenedetti, R. K. Prud'homme, B. A. Pethica, Differential scanning calorimetric studies of clathrate hydrate formation, J. Phys. Chem. B 108 (2004) 16717–16722.

[19] B. Fouconnier, L. Komunjer, M. Ollivon, P. Lesieur, G. Keller, D. Clausse, Study of CCl_3F hydrate formation and dissociation in *W/O* emulsion by differential scanning calorimeter and x-ray diffraction, Fluid Phase Equilibria 250 (2006) 76–82.

[20] D. Dalmazzone, N. Hamed, C. Dalmazzone, L. Rousseau, Application of high pressure DSC to the kinetics of formation of methane hydrate in water-in-oil emulsion, J. Therm. Anal. Calorim. 85 (2006) 361–368.

[21] D. Dalmazzone, N. Hamed, C. Dalmazzone, DSC measurements and modeling of the kinetics of methane hydrate formation in water-in-oil emulsion, Chem. Eng. Sci. 64 (2009) 2020–2026.

[22] J. W. Lachance, E. D. Sloan, C. A. Koh, Effect of hydrate formation/dissociation on emulsion stability using DSC and visual techniques, Chem. Eng. Sci. 63 (2008) 3942–3947.

[23] S. R. Davies, K. C. Hester, J. W. Lachance, C. A. Koh, E. D. Sloan, Studies of hydrate nucleation with high pressure differential scanning calorimetry, Chem. Eng. Sci. 64 (2009) 370–375.

[24] J. Zhang, J. W. Lee, Effect of sodium dodecyl sulfate on the supercooling point of ice and clathrate hydrates, Energy Fuels 23 (2009) 3045–3047.

[25] S. R. Davies, J. W. Lachance, E. D. Sloan, C. A. Koh, High-pressure differential scanning calorimetry measurements of the mass transfer resistance across a

methane hydrate film as a function of time and subcooling, Ind. Eng. Chem. Res. 49 (2010) 12319–12326.

[26] D. Clausse, F. Gomez, I. Pezron, L. Komunjer, C. Dalmazzone, Morphology characterization of emulsions by differential scanning calorimetry, Adv. Colloid Interfac. 117 (2005) 59–74.

[27] D. Clausse, Differential thermal analysis, differential scanning calorimetry, and emulsions., J. Therm. Anal. Calorim. 101 (2010) 1071–1077.

[28] S. Gao, W. G. Chapman, W. House, NMR and viscosity investigation of clathrate hydrate formation and dissociation, Ind. Eng. Chem. 44 (2005) 7373–7379.

[29] C. P. Aichele, W. G. Chapman, L. D. Rhyne, H. J. Subramani, A. Montesi, J. L. Creek, W. House, Nuclear magnetic resonance analysis of methane hydrate formation in water-in-oil emulsions, Energy Fuels 23 (2009) 835–841.

[30] D. K. Staykova, W. F. Kuhs, A. N. Salamatin, T. Hansen, Formation of porous gas hydrates from ice powders: diffraction experiments and multistage model, J. Phys. Chem. B 107 (2003) 10299–10311.

[31] L. A. Stern, S. H. Kirby, S. Circone, W. B. Durham, Scanning electron microscopy investigations of laboratory-grown gas clathrate hydrates formed from melting ice, and comparison to natural hydrates, Am. Mineral. 290 (2004) 1162–1175.

[32] H. Ohno, T. A. Strobel, S. F. Dec, E. D. Sloan, C. A. Koh, Raman studies of methane-ethane hydrate metastability, J. Phys. Chem. A 113 (2009) 1711–1716.

[33] S. R. Davies, E. Sloan, A. K. Sum, C. A. Koh, In situ studies of the mass transfer mechanism across a methane hydrate film using high-resolution confocal Raman spectroscopy, J. Phys. Chem. C 114 (2010) 1173–1180.

[34] T. Jakobsen, J. Sjöblom, P. Ruoff, Kinetics of gas hydrate formation in *w/o* emulsions: The model system trichlorofluoromethane/water/non-ionic surfactant studied by means of dielectric spectroscopy, Colloid Surface A 112 (1996) 73–84.

[35] A. K. Sum, C. A. Koh, E. D. Sloan, Clathrate hydrates: from laboratory science to engineering practice, Ind. Eng. Chem. Res. 48 (2009) 7457–7465.

[36] C. P. Ribeiro, P. L. C. Lage, Modeling of hydrate formation kinetics: State-of-the-art and future directions, Chem. Eng. Sci. 63 (2008) 2007–2034.

[37] P. U. Karanjkar, J. W. Lee, J. F. Morris, Morphological and calorimetric investigation of hydrate-forming water-in-oil emulsions, in: Proceedings of the 7^{th} International Conference on Gas Hydrates (ICGH), 2011.

[38] P. U. Karanjkar, J. W. Lee, J. F. Morris, Calorimetric investigation of cyclopentane hydrate formation in an emulsion, Chem. Eng. Sci. 68 (2012) 481–491.

[39] R. Sakemoto, H. Sakamoto, K. Shiraiwa, R. Ohmura, T. Uchida, Clathrate hydrate crystal growth at the seawater / hydrophobic - guest - liquid interface, Cryst. Growth Des. 10 (2010) 1296–1300.

[40] J. T. Davis, E. K. Rideal, Interfacial Phenomena, Academic Press Inc. (London) Ltd., New York, N.Y., USA, 1963.

[41] A. Drelich, F. Gomez, D. Clausse, I. Pezron, Evolution of water-in-oil emulsions stabilized with solid particles influence of added emulsifier, Colloid Surface A 365 (2010) 171–177.

[42] A. Carte, The freezing of water droplets, Proc. Phys. Soc. London, Sect. B 69 (1956) 1028–1037.

[43] D. Clausse, F. Gomez, C. Dalmazzone, A method for the characterization of emulsions, thermogranulometry: Application to water-in-crude oil emulsion., J. Colloid Interf. Sci. 287 (2005) 694–703.

[44] S. S. Fan, D. Q. Liang, K. H. Guo, Hydrate equilibrium conditions for cyclopentane and a quaternary cyclopentane-rich mixture, J. Chem. Eng. Data 46 (2001) 930–932.

[45] E. D. Sloan, Clathrate hydrates of natural gases, 2nd edition, Marcel Dekker, New York, 1998.

[46] J. S. Wettlaufer, M. G. Worster, Premelting dynamics, Annu. Rev. Fluid Mech. 38 (2006) 427–452.

[47] Y. Rabin, P. S. Steif, Thermal stresses in a freezing sphere and its application to cryobiology, Trans. ASME 65 (1998) 328–333.

[48] Q. T. Pham, Stresses, strains and failure of biomaterials during freezing, Eurotherm Seminar 77 - Heat and Mass Transfer in Food Processing June 20-22 (2005) Parma, Italy.

[49] H. C. Fogler, Elements of chemical reaction engineering, third edition, Printice-Hall Inc, Upper Saddle River, NJ, 2005.

[50] D. J. Turner, K. T. Miller, E. D. Sloan, Methane hydrate formation and an inward growing shell model in water-in-oil dispersions, Chem. Eng. Sci. 64 (2009) 3996–4004.

[51] Y. Zhong, R. E. Rogers, Surfactant effects on gas hydrate formation, Chem. Eng. Sci. 55 (2000) 4175–4187.

[52] R. Ohmura, T. Shigetomi, Y. H. Mori, Formation, growth and dissociation of clathrate hydrate crystals in liquid water in contact with a hydrophobic hydrate-forming liquid, J. Cryst. Growth 196 (1999) 164–173.

[53] R. Ohmura, W. Shimada, T. Uchida, Y. H. Mori, S. Takeya, J. Nagai, H. Minagawa, T. Ebinuma, H. Narita, Clathrate hydrate crystal growth in liquid water saturated with a hydrate-forming substance: variations in crystal morphology, Philos. Mag. 84 (2004) 1–16.

[54] P. Servio, P. Englezos, Morphology of methane and carbon dioxide hydrates formed from water droplets, AIChE J. 48 (2003) 269–276.

[55] R. Tanaka, R. Sakemoto, R. Ohmura, Crystal growth of clathrate hydrates formed at the interface of liquid water and gaseous methane, ethane, or propane: Variations in crystal morphology, Cryst. Growth Des. 9 (2009) 2529–2536.

[56] K. Saito, M. Kishimoto, R. Tanaka, R. Ohmura, Crystal growth of clathrate hydrate at the interface between hydrocarbon gas mixture and liquid water, Cryst. Growth Des. 11 (2011) 295–301.

[57] H. Bruusgaard, L. D. Lessard, P. Servio, Morphology study of structure I methane hydrate formation and decomposition of water droplets in the presence

of biological and polymeric kinetic inhibitors, Cryst. Growth Des. 9 (2009) 3014–3023.

[58] K. Okutani, Y. Kuwabara, Y. H. Mori, Surfactant effects on hydrate formation in an unstirred gas/liquid system: An experimental study using methane and sodium alkyl sufates, Chem. Eng. Sci. 63 (2008) 183–194.

[59] J. Yoslim, P. Linga, P. Englezos, Enhanced growth of methane-propane clathrate hydrate crystals with sodium dodecyl sulfate, sodium tetradecyl sulfate, and sodium hexadecyl sulfate surfactants, J. Cryst. Growth 313 (2010) 68–80.

[60] C. Y. Sun, B. Z. Peng, A. Dandekar, Q. L. Ma, G. J. Chen, Studies on hydrate film growth, Annu. Rep. Prog. Chem. C 106 (2010) 77–100.

[61] S. Hoiland, K. M. Askvik, P. Fotland, E. Alagic, T. Barth, F. Fadnes, Wettability of freon hydrates in crude oil/brine emulsions, J. Colloid Interf. Sci. 287 (2005) 217–225.

[62] P. Fotland, K. M. Askvik, Some aspects of hydrate formation and wetting, J. Colloid Interf. Sci. 321 (2008) 130–141.

[63] J. Sjöblom, B. Øvrevoll, G. Jentoft, C. Lesaint, T. Palermo, A. Sinquin, P. Gateau, L. Barre, S. Subramanian, J. Boxall, S. Davies, L. Dieker, D. Greaves, J. Lachance, P. Rensing, K. Miller, E. D. Sloan, C. A. Koh, Investigation of hydrate plugging and non-plugging properties of oils, J. Disper. Sci. Technol. 31 (2010) 1100–1119.

[64] L. E. Zerpa, J. L. Salager, C. A. Koh, E. D. Sloan, A. K. Sum, Surface chemistry and gas hydrate in flow assurance, Ind. Eng. Chem. Res. 50 (2011) 188–197.

[65] H. Sakaguchi, R. Ohmura, Y. H. Mori, Effects of kinetic inhibitors on the formation and growth of hydrate crystals at a liquid-liquid interface, J. Cryst. Growth 247 (2003) 631–641.

[66] J. D. Lee, M. Song, R. Susilo, P. Englezos, Dynamics of methane-propane clathrate hydrate crystal growth from liquid water with or without the presence of n-heptane, Cryst. Growth Des. 6 (2006) 1428–1439.

[67] R. Kumar, J. D. Lee, M. Song, P. Englezos, Kinetic inhibitor effects on methane/propane clathrate hydrate-crystal growth at the gas/water and water/n-heptane interfaces, Cryst. Growth Des. 310 (2008) 1154–1166.

[68] C. J. Taylor, K. T. Miller, C. A. Koh, E. D. Sloan, Macroscopic investigation of hydrate film growth at the hydrocarbon/water interface, Chem. Eng. Sci. 62 (2007) 6524–6533.

[69] Z. M. Aman, L. E. Dieker, G. Aspenes, A. K. Sum, E. D. Sloan, C. A. Koh, Influence of model oil with surfactants and amphiphilic polymers on cyclopentane hydrate adhesion forces, Energy Fuels 24 (2010) 5441–5445.

[70] J. Peixinho, P. U. Karanjkar, J. W. Lee, J. F. Morris, Rheology of hydrate forming emulsions, Langmuir 26 (2010) 11699–11704.

[71] S. Y. Lin, K. McKeigue, C. Maldarelli, Diffusion-controlled surfactant adsorption studied by pendant drop digitization, AIChE J. 36 (1990) 1785–1795.

[72] R. Pan, J. Green, C. Maldarelli, Theory and experiment on the measurement of kinetic rate constants for surfactant exchange at an air/water interface, J. Colloid Interf. Sci. 205 (1998) 213–230.

[73] L. J. Paltonen, J. Yliruusi, Surface pressure, hysteresis, interfacial tension and cmc of four sorbitan monoesters at water-air, water-hexane, and hexane-air interfaces, J. Colloid Interf. Sci. 227 (2000) 1–6.

[74] E. Santini, L. Liggieri, L. Sacca, D. Clausse, F. Ravera, Interfacial rheology of span 80 adsorbed layers at paraffin oil-water interface and correlation with the corresponding emulsion properties, Colloid Surface A 309 (2007) 270–279.

[75] B. P. Binks, Particles as surfactants – similarities and differences, Curr. Opin. Colloid. In. 7 (2002) 21–41.

[76] R. Camargo, T. Palermo, A. Sinquin, P. Glenat, Rheological characterization of hydrate suspensions in oil dominated systems, Annals of New York Academy of Sciences 912 (2000) 906–916.

[77] R. Camargo, T. Palermo, Rheological properties of hydrate suspensions in an asphaltenic crude oil, in: Proceedings of the 4^{th} International Conference on Gas Hydrates (ICGH), 2002.

[78] V. Andersson, J. S. Gudmundsson, Flow properties of hydrate-in-water slurries, Annals of New York Academy of Sciences 912 (2000) 322–329.

[79] A. Sinquin, T. Palermo, Y. Peysson, Rheological and flow properties of gas hydrate suspensions, Oil Gas Sci. Technol. – Rev. IFP 59 (2004) 41–57.

[80] A. Fidel-Dufour, F. Gruy, J. M. Herri, Rheology of methane hydrate slurries during their crystallization in a water in dodecane emulsion under flow, Chem. Eng. Sci. 61 (2006) 505–515.

[81] E. Colombel, P. Gateau, L. Barre, F. Gruy, T. Palermo, Discussion of agglomeration mechanisms between hydrate particles in water in oil emulsions, Oil Gas Sci. Technol. – Rev. IFP 64 (2009) 629–636.

[82] R. B. Schüller, M. Tande, H. K. Kvandal, Rheological hydrate detection and characterization, Annual Transactions of the Nordic Rheology Society 13 (2005) 83–90.

[83] P. J. Rensing, M. W. Liberatore, C. A. Koh, E. D. Sloan, Rheological investigation of hydrate slurries, in: Proceedings of the 6^{th} International Conference on Gas Hydrates (ICGH), 2008.

[84] P. J. Rensing, M. W. Liberatore, A. K. Sum, C. A. Koh, E. D. Sloan, Viscosity and yield stress of ice slurries formed in water-in-oil emulsions, J. Non-Newton. Fluid. 166 (2011) 859–866.

[85] P. G. Debenedetti, Supercooled and glassy water, J. Phys. Condens. Matter 15 (2003) R1669–R1726.

[86] R. F. Ma, L. Shi, Y. Y. Duan, L. Z. Han, N. X. Liu, Saturated liquid viscosity of cyclopentane and isopentane, J. Chem. Eng. Data 48 (2003) 1418–1421.

[87] J. McCulfor, P. Himes, M. R. Anklam, The effects of capillary forces on the flow properties of glass particle suspensions in mineral oil, AIChE J. 57 (2011) 2334–2340.

[88] J. G. Göbel, G. R. Joppien, Dynamic interfacial tensions of aqueous Triton X-100 solutions in contact with air, cyclohexane, n-heptane and n-hexadecane, J. Colloid Interf. Sci. 191 (1997) 30–37.